Thèse (Dissertation)

"Radiation damage induced by neutrons in CMS silicon sensors"

Forton, Eric

Abstract

Les expériences conduites auprès du futur accélérateur LHC au CERN nécessitent la construction des détecteurs les plus grands et les plus complexes jamais conçus. En particulier, le trajectographe de la collaboration CMS utilisera uniquement des détecteurs micropiste silicium et ce, en très grandes quantités. Ce dernier dépend donc de manière capitale de la qualité de toute la production des senseurs et la collaboration CMS a ainsi décidé de mettre en place un vaste programme de contrôle de cette qualité. Cette thèse présente une partie des travaux réalisés à l'UCL dans ce cadre. La discussion porte en particulier sur résistance aux radiations des senseurs en silicium, testée de manière routinière à Louvain-la-Neuve. Le texte débute par une présentation du détecteur CMS et des dégâts radiatifs subits par les détecteurs micropiste silicium. Les dispositifs expérimentaux mis en place auprès des cyclotrons et dans le laboratoire de l'institut de Physiq...

Référence bibliographique

Forton, Eric. *Radiation damage induced by neutrons in CMS silicon sensors.* Prom. : Grégoire, Ghislain

UCL - Université catholique de Louvain
Faculté des Sciences
Département de Physique

Radiation damage induced by neutrons in CMS silicon sensors

Eric Forton

Promoteur: Prof. Ghislain Grégoire

Dissertation présentée pour obtenir le titre de

Docteur en Sciences

Louvain-la-Neuve, mars 2006

C'est déjà la troisième fois que je commence des remerciements en citant le professeur Ghislain Grégoire. Je tiens vivement à le remercier et à souligner le rôle capital qu'il a joué dans ma formation depuis maintenant presque sept ans.

Je voudrais aussi remercier collectivement les membres constituant mon jury pour les commentaires très complémentaires dont ils m'ont fait part. En particulier, je me réjouis de compter le Professeur Frank Hartmann parmi ces membres : l'équipe de Karlsruhe fut d'une aide certaine lors de la mise en route du dispositif de mesure réalisé autour de la probe station.

Ce travail est avant tout expérimental. La mise au point des dispositifs de mesure n'aurait se faire sans l'aide des ateliers de mécanique et d'électronique dont l'expérience et le feeling est inestimable. Parce que la collaboration fut plus étroite avec eux, je citerai Willy, Bernard, Dominique, Pierre, Luc ou Jean-Marc. Travailler avec eux fut toujours un réel plaisir.

Un dispositif d'irradiation n'est rien sans faisceau ! Les « nôtres » sont en général très stables grâce à toute l'équipe du cyclotron. Je tiens aussi à présenter mes excuses à ceux que j'ai réveillés lors certaines irradiations parce que « ça a sauté ».

Pour avoir travaillé ensembles pendant toute la durée de nos thèses, Samia reçoit évidemment toute ma sympathie. Heureusement que nous pouvions compter l'un sur l'autre pour assurer les gardes lors des longues nuits auprès du cyclotron et réaliser à tour de rôle les mesures avec la probe station!
Nous avons pu profiter à l'occasion du dévouement de Guillaume, Muriel, Christophe et Otilia lors de certains shifts. Je tenais à les en remercier… Et surtout j'espère n'oublier personne tant le temps peut paraître long sur le coup des 4-5 h du matin !

Terminer la rédaction de cette thèse me donne l'occasion de constater que ces dernières années furent riches d'expériences et de rencontres en tous genres. Je tiens à remercier tous ceux qui contribué à cela.
Dans ce contexte, je ne peux pas terminer sans remercier Papa, Maman, Patricia et Gaëlle. Les deux premiers parce qu'il m'est impossible de même dresser la liste de ce qu'ils ont fait pour moi (ils seront soulagés de me voir terminer), les deux dernières… Juste « parce que » !

Table of contents

Table of contents ***4***

Introduction ***7***

Chapter 1 : CMS and the LHC ***9***

1.1. The LHC **9**

1.2. Zoom on CMS **13**
1.2.1. The CMS tracker 17
1.2.2. Radiative environment in the CMS Tracker 24

Chapter 2 : Silicon detectors ***27***

2.1. Properties of the crystal **27**

2.2. Principle of operation, characteristics **29**
2.2.1. Charge collection and position resolution 34
2.2.2. Electrical properties of a strip detector 35

2.3. Radiation-induced changes in detector properties **38**
2.3.1. Basic damage process 39
2.3.2. The NIEL hypothesis 40
2.3.3. Evolution of detector properties 43
2.3.4. Correlations between microscopic defects and macroscopic properties 48
2.3.5. Comments on bias and irradiation rate 50

2.4. CMS sensors designs **51**

2.5. Qualification procedure for the CMS tracker sensors **55**

Chapter 3 : Experimental setups ***59***

3.1. Electrical characterisation setup **59**
3.1.1. Instrumentation, acquisition program 59
3.1.2. Performances, measurement accuracy 63
3.1.3. Encountered Problems 66
3.1.4. Cross calibration with the Karlsruhe system 69

3.2. The T2 beam line and instruments around the irradiation zone **72**
3.2.1. The High flux neutron beam line 73
3.2.2. Sensor environment, cold box 76
3.2.3. Sensor biasing 79
3.2.4. Acquisition and monitoring 83

3.3. Sensor test protocol in Louvain **84**

3.4. Summary **86**

Chapter 4 : Evolution under irradiation ***89***

4.1. Experimental neutron hardness factors **89**
4.1.1. Diodes description, pre-irradiation qualification 90
4.1.2. Monoenergetic neutron beam line (“Q” beam line) 91
4.1.3. Principle of the test 93
4.1.4. Post-irradiation measurements and calculations 96
4.1.5. Summary and comparison with literature 99

4.2. Analysis of CMS test structures **101**
4.2.1. The impact of bulk biasing during irradiation 103
4.2.2. Summary of the irradiation results 112

Conclusions ***127***

Annexes ***129***

A.1. Dosimetry and fluence calculations **129**
A.1.1. Beam monitor 129
A.1.2. Activation 131
A.1.3. Alanine 134

A.2. Thermal treatment of the sensors: annealing oven **141**
A.2.1. Principle 142
A.2.2. Performances 143

A.3. Useful constants **145**
A.3.1. Silicon properties 145
A.3.2. Silicon oxide properties (SiO_2) 146

Terms, abbreviations ***147***

Bibliography ***153***

List of figures ***157***

List of tables ***161***

Introduction

The LHC accelerator, currently under construction at CERN, will be the theatre where Physicists will watch the most powerful collisions ever seen so far, at an unprecedented rate. It will be a state-of-the-art accelerator giving physicists a chance to uncover new secrets and to shed light on processes that have not been observed yet.

Indeed, the standard model of particles and interactions, confirmed so far by many results at previous accelerators, requires the existence of a still unobserved particle, the Higgs boson, in order to be complete. Also, new mechanisms and theories beyond the standard model have been proposed by theoreticians but they still need experimental observations to be either confirmed or ruled out.

At the LHC, the Belgian universities are involved in CMS*, a general-purpose detector among the four experiments that will be installed along the accelerator ring. CMS will be, like other High Energy Physics experiments, an onion-like detector composed of different layers: from the outermost Muon-chambers to the innermost tracker and pixel detectors. Our group is involved in the construction of the tracker, which will be uniquely composed of about 25000 silicon detectors, covering a sensitive area of 206 m^2. The description of CMS, its tracker and the LHC environment are given in chapter 1.

To the contrary of previous accelerators with relatively low radiation levels, the very characteristics of the LHC will generate a radiation environment that will be the harshest High Energy Physics environment so far. Hence, operating silicon detectors for 10 years or more at these radiation levels is one among the many challenges raised [5]. Chapter 2 is dedicated to the description of silicon microstrip detectors, their operating principle and their evolution after a long exposure to high radiation levels.

Previously involved in testing the radiation tolerance of MSGCs, our group had also some experience with silicon detectors but we took the opportunity to enter the world of large scale segmented silicon detectors through an involvement in monitoring the radiation tolerance during the production of sensors dedicated to the CMS tracker. Indeed, the large

* CMS stands for Compact Muon Solenoid.

number of sensors requires a complex strategy for the qualification of the sensors, ensuring these have stable characteristics in order to build a reliable tracker. This qualification procedure is described at the end of chapter 2 and the tools developed in Louvain-la-Neuve to perform these tests are described in chapter 3.

Finally, the results obtained on CMS sensors from 2002 to 2004 will be presented in chapter 4, together with other tests made in parallel. The conclusions present a short summary of the entire document.

Chapter 1 : CMS and the LHC

1.1. The LHC

Starting in 2007 and for the next few years, the High Energy Physics community will look towards events and reactions at CERN's Large Hadron Collider.

Indeed, the LHC will collide protons together at an unprecedented center-of-mass energy of 14 TeV. The bunch spacing will be of 25 ns, leading to a luminosity of 2 10^{33} $cm^{-1}.s^{-1}$ in the beginning and raised afterwards to 10^{34} $cm^{-1}.s^{-1}$ (100 pb^{-1} per year). The centre of mass energy, combined with the high luminosity will give a unique opportunity to investigate and study new Physics, even very rare events.

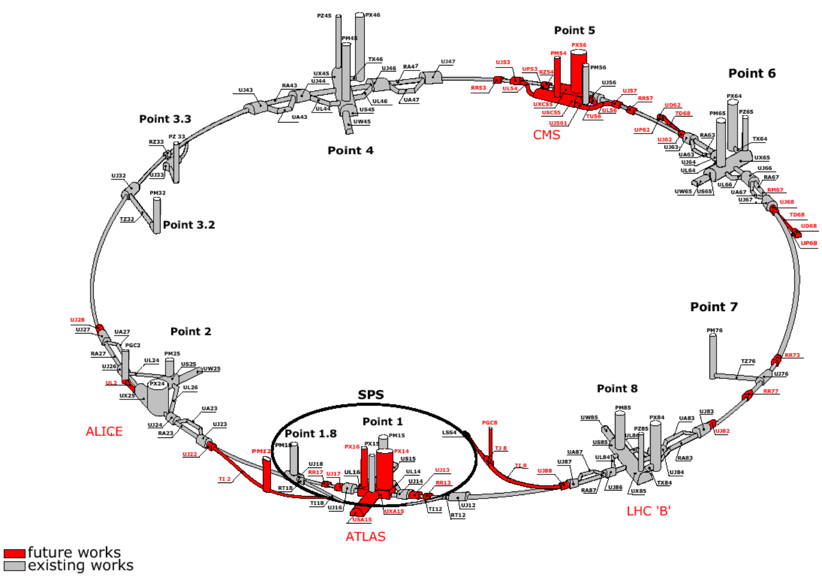

Fig. 1 : The LHC underground installations. The grey structures were already existing at LEP.

The LHC (Fig. 1) will be located in the 27 km-long circular tunnel previously drilled for LEP, but additional caverns and surface structures have been excavated to meet the larger space requirements of the new experiments and to house the necessary services needed to cool down an all-superconducting accelerator.

During operation at high luminosity, there will be no less than ~20 min bias events per bunch crossing, ~1000 charged tracks per event in each experiment. This qualifies the LHC as the most severe radiation environment that any High Energy Physics experiment will have to undergo so far. This latter point is discussed in 1.2.2. while this section focus mainly on the Physics motivations to build the LHC.

For sure the hottest topic at LHC will be the search of the last missing piece of the standard model: the Higgs boson. Its mass is not predicted by theory although there are already constraints coming from previous experiments: we know from LEP that the mass of the Higgs boson should be above 114 GeV. The ignorance of the Higgs boson mass leads to the fact that various scenarios have to be considered and the study of many discovery channels is required, as presented in Fig. 2.

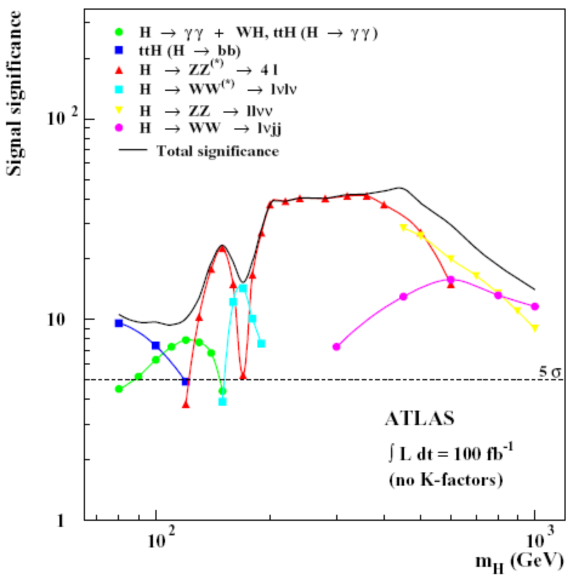

Fig. 2 : Signal significance of the various SM-Higgs discovery channels, after one year or 100 fb^{-1} (from [7]).

The different channels pictured in Fig. 2 can be dispatched into different categories according to the Higgs production mechanism. For instance, a Standard Model (SM) Higgs can be produced through the fusion of two gluons (gluon fusion channels), or via quark interactions in the weak boson fusion channels:

The three gluon fusion channels are:

$gg \rightarrow H \rightarrow \gamma\gamma$ (for $m_H \leq 150$ GeV)

$gg \rightarrow H \rightarrow ZZ^* \rightarrow 4l$ (for $m_H \geq 120$ GeV)

$gg \rightarrow H \rightarrow WW^* \rightarrow l\nu l\nu$ (for $m_H \geq 130$ GeV)

The weak boson fusion channels are:

$qq \rightarrow qqH$, then $H \rightarrow \gamma\gamma$ (for $m_H \leq 150$ GeV)

$qq \rightarrow qqH$, then $H \rightarrow \tau\tau$ (for $m_H \leq 150$ GeV)

$qq \rightarrow qqH$, then $H \rightarrow e^{\pm}\mu^{\pm}\ p_{t,miss}$ (for $m_H \geq 110$ GeV)

$p_{t,miss}$ is missing transverse momentum.

There are even more channels, involving for instance the Higgs decay into a pair of b quarks after a WH or a ttH production:

$q\bar{q} \rightarrow WH$, then $H \rightarrow b\bar{b}$ (for $m_H \leq 120$ GeV)

$q\bar{q} \rightarrow t\bar{t}H$, then $H \rightarrow b\bar{b}$ (for $m_H \leq 130$ GeV)

show that a high resolution tracker is a key subdetector.

These channels, part of the Standard model studies at LHC, already show that LHC detectors must be built according to the present state-of-the-art technology. Every sub-detector plays a crucial role as the exciting perspectives requires the observation of many different decay channels involving photon, quark (jet) and lepton measurements in turn, hence requiring good calorimeters, accurate trackers and an efficient muon system. Many of the decay channels also involve the measurement of missing energy or transverse momentum, hence requiring a detector as “particle-tight” as possible.

The purpose of this section is not to survey the entire Physics program. It is however worth to mention that, besides the SM Higgs discovery, there are numerous extensions to the standard model, among which supersymmetry. This extension assumes that each fermion has a boson counterpart (the squarks and sleptons), and the standard model bosons have fermionic superpartners (gluinos and gauginos). This theory, to be confirmed, implies the discovery, the identification and study of a whole new spectrum of particles, including no less than 5 Higgs particles. The entire parameter space of the minimal supersymmetric model (MSSM) can be studied at LHC and hence if supersymmetric higgses exist, some of these have also to be observed at LHC [8].

Apart from supersymmetry, numerous exotic models are proposed as extensions of the standard model (refer e.g. to [7], [8] or [9]). A possibility would be to consider a fourth generation of leptons and quarks. Predictions on a fourth generation of quarks show a dominant decay mode to Wb. Hence again, the detection of secondary vertices and an accurate tracking are needed.

Other model predicts the existence of new heavy gauge bosons (W' and Z', with a mass of several TeV) or even magnetic monopoles, leptoquarks (particles carring both a leptonic and a baryonic quantum number)… There is also the so-called Technicolor, a new strong interaction at high energy scales that gives a possible alternative to the Higgs mechanism of electroweak symmetry breaking but implies the existence of specific technifermions.

Furthermore, if the presence of extra-dimensions is observed in collider experiments, it may be a major step towards a unified theory of the fundamental interactions. Hence they will be studied at the LHC, both in direct (cf. [10]) observation channels and indirect ones (cf. [11]).

As far as the tracker is concerned, the need for resolution is clearly seen in channels involving lepton identification – for instance, the accurate identification and reconstruction of electrons implies a good separation with photon events in the electromagnetic calorimeter- but even more in the channels involving the secondary vertex measurements, as is the case for detecting the b quarks. The tracker is also used for jet isolation, and even at low Higgs mass, for $H\rightarrow\gamma\gamma$ it is useful to calibrate the electromagnetic calorimeter. The CMS collaboration decided the following design guidelines (cf. [13]):

- The leptons should be measured up to η=2.5, hence the tracker has to cover the pseudorapidity range up to at least this value.

- The transverse momentum P_t resolution should be better than 1 % below 100 GeV for an intermediate mass Higgs discovery.

- A z-resolution of 2 cm for the primary vertex is a minimum requirement. This implies a tracker with small cells coupled to an efficient and robust pattern recognition algorithm due to the pile-up.

- A fast response time is needed due to the high data acquisition frequency.

- The material budget must not be neglected and kept as low as possible as this is a crucial factor in the energy resolution for electrons and gamma measurements.

1.2. Zoom on CMS

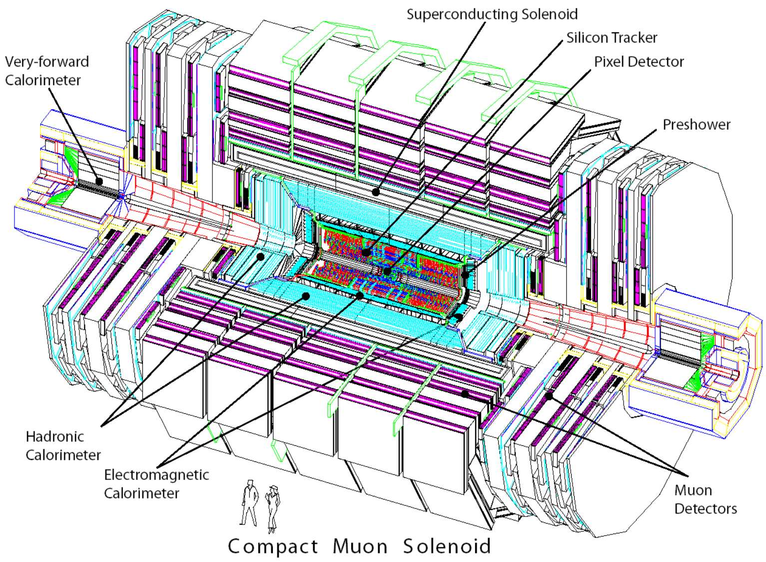

Fig. 3 : Layout of the CMS experiment at LHC.

The Compact Muon Solenoid will be one of the four LHC experiments. It is a multi-purpose particle physics detector based, like any modern High-energy Physics experiment, on an onion-like structure. One of its peculiarities is its innovative design, based on new technologies used at a large scale. A sketch of the experiment is shown on Fig. 3. This paragraph is aimed to describe briefly the different sub detectors making CMS.

Starting from the outer part and successively “removing” in turn all the layers of our “onion”, the first and most external sub detector encountered is the muon system. Indeed, muons are, right after the undetected neutrinos, the most penetrating particles produced at LHC. The outermost detectors, placed in the gaps of the return yoke, are hence dedicated to the tagging of these muons. In the case of CMS, the muon system consists of drift tubes (DT) in the barrel (up to η=1.2) and cathode strip chambers (CSC) in the endcaps, up to η=2.1. Additional resistive plate chambers (RPC) are used for bunch identification.

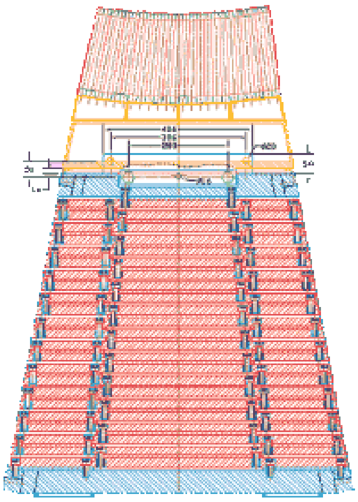

Fig. 4 : A slice view of the HCAL Barrel: copper plates interleaved with plastic scintillators sheets. Copper plates are 50 mm thick whereas scintillator plates are 4 mm thick. The readout uses plastic wavelength shifting fibers.

Right inside the muon system, one finds the outer barrel of the hadronic calorimeter, installed there because HCAL is only about 6.5 radiation lengths thick. Removing this outer barrel uncovers the superconducting magnet. It will be one of the biggest and most powerful magnet ever built, able to deliver a magnetic field of 4 Tesla in a volume about 355 m^3. This magnet contains the calorimeters for energy measurements. It implies that the sensitive elements of the calorimeters will operate in a high magnetic field, hence narrowing the choice of technology for the detectors to be used.

With the magnet yoke "peeled off", we now look at the hadronic calorimeter. It is a sampling calorimeter made of successive layers of copper plates (radiator) and plastic scintillator sheets with a wavelength-shifting fibre readout. HCAL covers all directions up to η=3. At high η, in the very forward calorimeter, copper is replaced with steel to minimize activation problems and the scintillators are replaced by quartz fibers, able to sustain higher radiation doses. Due to the high magnetic field, the fibres are readout using hybrid photodiodes ("HPD"[¤]). The granularity of the calorimeter, corresponding to an array of 5X5 cm^2 crystals, is about 0.087 by 0.087 in η and Φ[*].

Going deeper inside, the next item found is the electromagnetic calorimeter. It has been optimized for the $H\rightarrow\gamma\gamma$ decay channel since a mass resolution of $\Delta m_H/m_H < 1\%$ has to be achieved [8]. This calorimeter is made of more than 80000 $PbWO_4$ crystals. Despite their low light emission level, they are a good choice because of their small radiation length (allowing a compact calorimeter design[*]), their small Molière radius (22 mm), their fast response and the good light collection (most of the light yield is collected within the 25ns bunch spacing).

CMS is monitored by different control systems to ensure a high accuracy of the measurements. For example, in the case of ECAL, the optical transmission of the crystals drifts with time and is therefore continuously monitored by means of light pulses that are injected using clear optical fibres. This interesting feature is pictured on Fig. 5. In the case of the tracker, the alignment and positioning of the different structures relative to each other and to the rest of the detector is continuously monitored by multiple infrared laser beams [14] that are seen by dedicated silicon sensors called "optical sensors".

[¤] HPD's are made of a photocathode and a diode separated by a gap of a few millimetres. A high electric field is applied between cathode and diode, so that photoelectrons are accelerated before being detected by the diode. In contrary to photomultipliers, a high axial magnetic field can be tolerated by these devices.

[*] It is usual to use cylindrical coordinates. In that case, z is the longitudinal distance in the beam direction, r is the radial distance and Φ the corresponding angle.

[*] The measurement of the energy in Ecal requires the crystals to be as long as 26 radiation lengths. In the Case of $PbWO_4$, this gives only 23 cm long crystals.

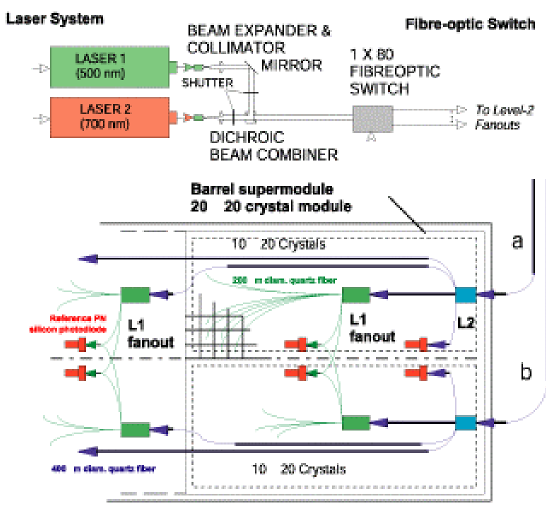

Fig. 5 : Light monitoring system of the CMS electromagnetic calorimeter. LASERs are used as light source and distributed over the entire calorimeter using optical switches and fanouts.

In addition to the ECAL crystals, there is a preshower detector in the endcaps to allow the separation of photon pairs, neutral pions and single photon events. This preshower detector consists of two layers of silicon strip detectors with orthogonal orientations, sandwiched between two lead sheets.

The inner tracking system is located further inside the calorimeters. It consists of the tracker and the pixel detectors. As the silicon strip tracker will be further described in paragraph 1.2.1, we will only say a few words about the pixels here.

The pixel detector (Fig. 6) is located as close as possible to the interaction point. It will be 120 cm-long, with an inner diameter of 8cm. The main purpose of this detector is the accurate determination of the vertex positions that are crucial for e.g. *b*-jet tagging (crucial for instance in the study of $H \rightarrow b\bar{b}$). To fulfil its role, it is designed to deliver 2 hits per track up to a pseudorapidity of η=2.2. With a pixel size of 150X150 µm², the high accuracy of the hit position is reached thanks to a signal interpolation between pixels, improved by the Lorentz-angle effect. This is the reason for choosing a turbine-like geometry for the disks. The induced charge division between adjacent strips, coupled with their analogue readout, enhances the accuracy in the particle crossing position to as low as about 15 µm, giving a resolution of about 50 µm for the transverse position of the vertex.

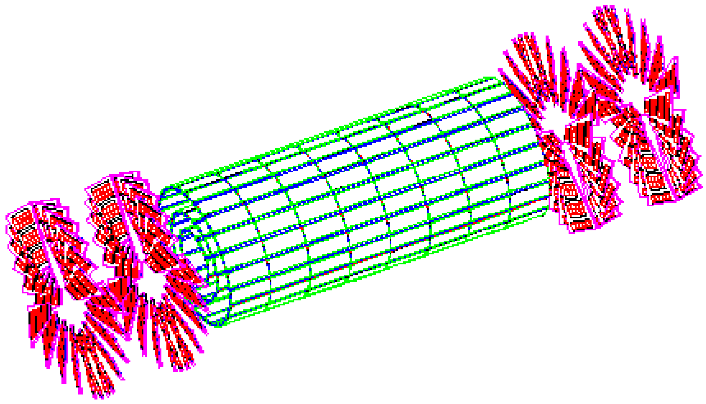

Fig. 6 : The CMS pixel detector layout. One distinguishes the three barrel layers and the two turbine-like endcaps on each side.

1.2.1. The CMS tracker

In 2000, the CMS collaboration decided to build an all-silicon tracker, putting aside the MSGC detectors. In the new design, the CMS tracker is subdivided in several different parts, namely (from the interaction point towards the calorimeter): the inner barrel, closed by 3 small disks on each side; the outer barrel; and the endcaps. This tracker will be the biggest all-silicon tracker ever built with about $11.4\ 10^6$ channels and an active surface of more than 200 m².

The inner part of the tracker consists of a barrel (TIB) with four layers of silicon modules arranged in concentric cylinders, flanked by three disks (TID) of three concentric rings of modules on each side. The sensors used to build the inner tracker modules are all 320 µm thick with low resistivity silicon wafers.

The outer part of the tracker is also made of a barrel (TOB) consisting of six concentric cylinders whereas the endcaps (TEC) are made of nine disks on each side, with seven rings of modules per disk. All modules will be built with 500 µm thick, high resistivity sensors apart the four innermost rings of the endcaps that will be assembled with 320 µm thick sensors because they are closer to the interaction point.

Fig. 7 shows the sketch of a quarter of the tracker together with the pixel detector. Starting from the interaction point in the lower left corner, one distinguishes the pixel detector, and thereafter the inner barrel, closed by the inner disks, and the outer barrel, closed by the endcaps.

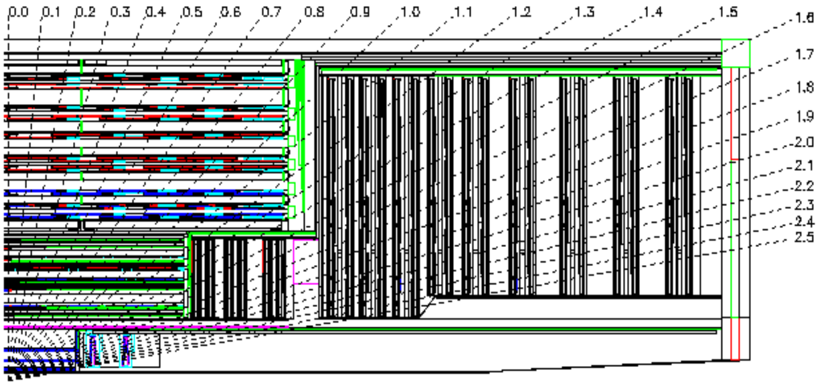

Fig. 7 : Transverse view of the CMS tracker. The radius is about 115 cm and the length about 270 cm on each side of the IP.

Looking further into the details of the tracker construction, we will first describe the support structures, going into more details on the detector modules thereafter.

The support structure of the tracker has to carry all the detectors, data and controls cables but must also respond to additional requirements:

- It houses the pipes of the cooling system to keep the tracker at a temperature of -10 °C in its entire volume of 24.4 m^3. Cooling will be needed to avoid reverse annealing of the depletion voltage of the silicon sensors (cf. 2.3.3.b) and also limit the leakage current (cf. 2.2.2), hence ensuring the detector to be kept fully depleted and limiting the noise in the mean time. The cooling power must be large enough to cope with the increased power consumption over the years* of operation and avoid thermal runaway.

- The temperature requirement implies that the tracker must be operated in a controlled dry atmosphere to avoid condensation on the sensors and electronics.

- The support structure has to be stiff enough to guarantee the accuracy of the position measurement of the tracker. One of the stringent requirements for this is the minimal deformation with

* The foreseen total power consumption of a petal after 10 years of use is about 70W for a “back” petal, 90 W for a front petal.

temperature cycling and a high stability versus time. The positioning precision of a module must be about 100 µm with time variations in the 10 µm range [17].

- The high magnetic field requires also the use of paramagnetic materials to limit stresses on the structure.

All these features have to be achieved with a mass as low as possible to limit its contribution to the material budget.

In the case of the CMS support structure, both the inner and outer barrels are made of a skeleton that supports the carbon fiber "rods" onto which the modules are attached. Inner and endcap disks are made of honeycomb panels with carbon fiber skins to ensure the stiffness. In the case of the TEC disks, the modules are arranged in "petals" fixed to the disks. These support structures are shown on Fig. 8.

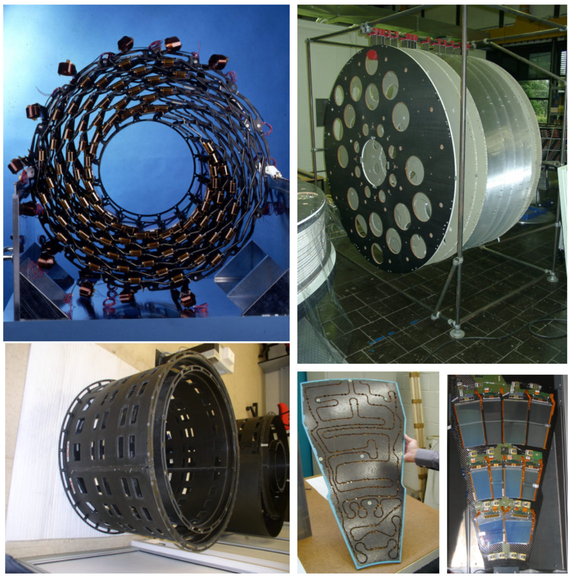

Fig. 8 Clockwise from bottom left: support structure of TIB, support structure of the TOB filled with some rods, TEC honeycomb support disk, TEC petal with modules, details of the cooling pipes grooves of a TEC petal.

As shown on the picture above, the low temperature operation of the tracker is obtained by the circulation of a cooling fluid. Despite the difficulties encountered at welding and soldering the pipes to their connectors, titanium has been chosen as a material for the endcap pipes due to its good radiation resistance, its absence of induced long-term radioactivity, its low mass and easy bending properties.

A module is the most basic yet fully functional detection unit of the tracker. It is made of a high thermal conductivity carbon fiber frame which supports one or two silicon sensors connected to their readout electronics using a pitch adapter.

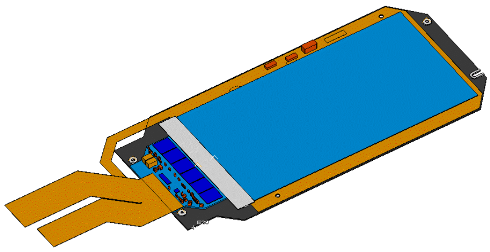

Fig. 9 : Drawing of a CMS barrel module. One can distinguish the carbon-fibre frame with the silicon sensors and their readout electronics.

There are several modules geometries within the tracker: 4 rectangular types are used to build the barrel, and 7 wedge-shaped are mounted on the petals of the endcaps. Among the different layers made of these modules, several are equipped with double sided (stereo) modules. A double sided module has twice the number of silicon sensors as a normal module: the microstrip sensors are mounted back to back and their strips are tilted by a relative angle of 0.1 rad to give a 3-D information about the particle crossing. The pitch of the sensors is higher in the outer parts of the tracker, where the need for high resolution is lower.

It is time now to focus on the tracker readout scheme. Sketched on Fig. 10, the readout electronics in the CMS tracker features several modules: the control (FEC-front end controller) and readout (FED-front end driver) systems are located outside the detector and get or send their information using numerous monomode optical fibres coming in and out of the tracker. Inside the detector itself, the control of the modules is made by the CCUs (clock control unit) that, for instance, distribute the clock and trigger signals. The module electronics performs the strip readout and local storage of the analogue data (analogue pipeline voltage-APV chip), but also integrates the controls and the multiplexers used to send the signals to the optical transmitters that gather signals from the modules and are in charge of sending the data to the counting room. After shaping, the signals of all strips are multiplexed and sent to the underground counting room via single mode optical fibres. This transmission mode has been chosen for its minimal contribution to the material budget and its immunity to electrical interferences.

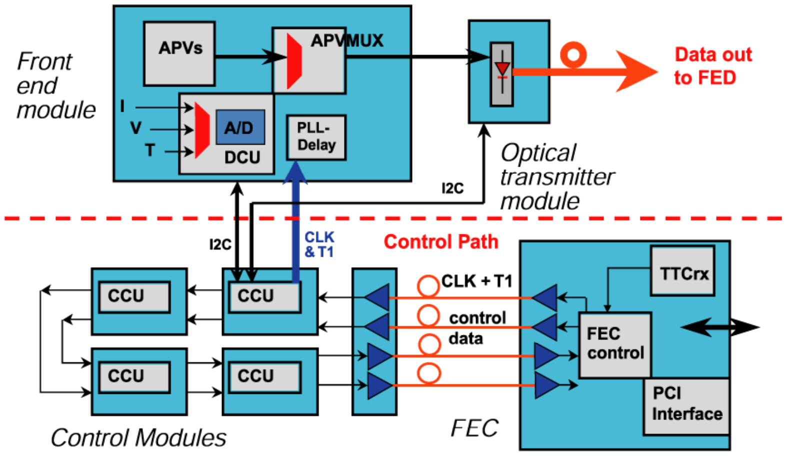

Fig. 10 : CMS tracker electronics overview.

All the different module types have a single readout scheme, using the same APV chip, described for example in [18]. Each strip on the sensors is connected to a charge sensitive amplifier and shaper sampled at 40 MHz and whose output is stored in an analogue pipeline, waiting for he L1 trigger.

Under normal running conditions, the APV shows a very good linearity: better than 5 %. It can be run in 3 different filter modes: peak, deconvolution and multi-mode:

- In peak mode, the signal amplitude of a single bunch crossing is recorded. In the absence of pile up, this gives a better signal to noise ratio and hence a better position resolution than the other modes.

- In deconvolution mode, the signal is shaped using three bunch crossings. The data of the three bunch crossings are stored on 3 capacitors of different values and the chip then outputs a weighted sum of the signal. This gives a better timing accuracy and removes the effects of pile-up but weakens somewhat the position resolution. At high luminosity, the signal to noise performance of tracking is decreased due to pile-up. The deconvolution mode allows to diminish pile up effects, and the S/N ratio is 1.7 times higher in this mode than in the peak mode.

- The multi-mode operation can be used when calibrating the pulse shape. In this mode multiple consecutive pipeline columns (corresponding to multiple bunch crossings) can be read without filtering.

The APV is implemented in 0.25 μm technology, which ensures a good noise performance and a high radiation tolerance by nature and design. By nature because the miniaturization of the chip reduces the oxide layers sizes and thicknesses, hence reducing the amount of charge trapping due to the exposure to radiation: the effects of radiation drop as the square of the oxide thickness and for very thin oxide layers (<10 nm, which is the case of the APV25), most of the charges drift away in a few minutes. Nevertheless, some design rules have to be taken into account to reinforce the radiation hardness, such as p^+ guardrings and enclosed transistors geometries to avoid leakage current paths. Such design rules also prevent the chip to be sensitive to single events effects (SEE*): for instance a test at PSI predicted a worst-case LHC scenario of 84 SEU/hour over all the 2000 CCUs of the tracker.

We already stated the requirements of the tracking system, among which the material budget. With all its features and the electronics described above, Fig. 11 shows the material budget of the CMS tracker for its different components in terms of radiation lengths [16].

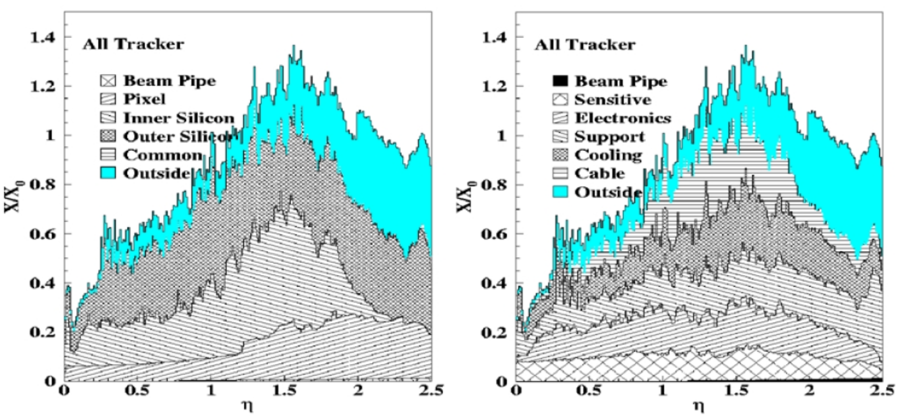

Fig. 11 : the tracker material budget distribution, expressed in terms of radiation lengths [16]. The photon attenuation length due to pair production is approximated by 7/9 the radiation length. At η=1.5, the photon attenuation is hence about 16 %.

* Short definitions of Single Event Effects is given at the end of this document.

As a general rule, the resolution of a tracker is proportional to:

$$\frac{\sigma_{p_t}}{p_t} \propto \frac{\varepsilon p_t}{0.3BL^2} \qquad (1.1)$$

Where p_t is the transverse momentum; σ_{pt} the error on the transverse momentum; ε, the error on the position perpendicularly to the track; B, the magnetic field and L, the track length. In the case of CMS, with a nominal magnetic field of 4 T and a radius of 1.1 m, the resolution of 1 % for tracks with p_t<100 GeV translates into a strip pitch of about 100 µm. (1.1) then becomes [19]:

$$\frac{\sigma_{p_t}}{p_t} \approx 0.12\left(\frac{pitch}{100\mu m}\right)\left(\frac{1.1m}{L}\right)^2\left(\frac{4T}{B}\right)\left(\frac{p_t}{1TeV}\right) \qquad (1.2)$$

As an example of the role of material budget in the performance of the tracker, The p_t resolution given by (1.2), valid in the case of a material-less tracker, is about 1.2 % for 100 GeV muons at low η, whereas a realistic tracker has a resolution of about 1.6 %.

The accuracy of track measurements has been simulated and studied in the case of muons (cf. [16]). It is foreseen to be between 10% at 1 TeV and 0.1 % at 1 GeV and low η. At high η the resolution lies between 30 and 2 %. The azimuthal angle resolution (Φ) is about the same, but is better for high P_t particles (about 0.01 %) compared to low P_t ones (about 0.2 %). The cotan(θ) resolution has been studied as well.: at low pseudorapidity, it is assessed at 0.05 % at high P_t and 0.2 % at low P_t; for higher pseudorapidity it is of the order of resp. 0.3 % and 2 %.

The track reconstruction efficiency for muons lies between 95 and 99 % depending on the muon P_t and η. When considering jets, the track finding efficiency falls to about 85 %.

These performance data are valid only after the alignment of the tracker, which will be performed at first with a laser beam system, and then, in the early operation of the detector, using real tracks of particle crossing the detector [20].

1.2.2. Radiative environment in the CMS Tracker

It has been pointed out at the beginning of this chapter that the high luminosity and the unprecedented beam energy of the LHC will generate the most difficult environment ever encountered by HEP experiments. It was therefore crucial to assess the fluxes inside the detector, and especially in the tracker, where these fluxes are the most intense. The purpose of this section is to outline the properties of the radiation field as described in [15] and updated in [16].

When considering the radiation hardness issues, dedicated simulations are needed since a non-negligible part of the damage comes from low-energy phenomena which are usually neglected when performing Physics studies. As a striking example, the radiation environment of the inner part of the tracker is dominated by direct contributions coming from the interaction point, but already at a radius of 50 cm, the tracker starts to undergo the intense flux of albedo neutrons generated by hadronic interactions with the ECAL crystals located at larger radii. While the radiation originating from the interaction point is irreducible, a polyethylene shielding is foreseen to limit this albedo neutron flux.

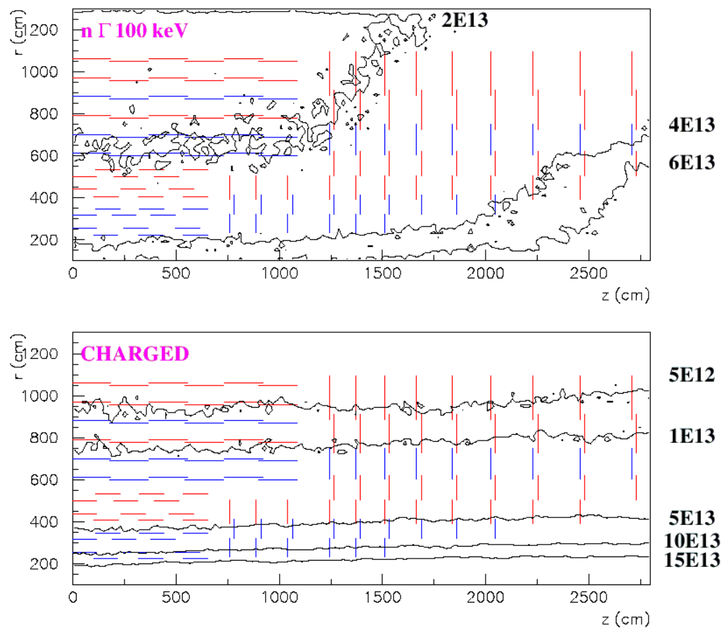

Fig. 12a, b : Neutron and charged particle integrated fluences in the CMS tracker expressed in particles.cm^{-2} after 10 years at the LHC.

Also, the fluxes and fluences obtained during the operation of the accelerator have to take several additional parameters into account: the luminosity variations (high or low luminosity runs and the number of fills per day) and the maintenance periods. All these parameters as well as their uncertainties led to a conservative estimation of the error margins as high as 30 % for the charged particle fluences and a factor 2 may be considered in the case of albedo neutrons.

Starting from these radiation fields, a total dose and fluence are deduced. For given particle types and known energy spectra, one can compute a NIEL normalisation factor (Table 1; more details about the method are given in paragraph 2.3.2).

	$|\eta|$= 0 – 0.9	**$|\eta|$= 0.9 – 1.8**	**$|\eta|$= 1.8 – 2.7**
R= 0 – 20 cm	75	69	62
R= 20 – 40 cm	88	85	82
R= 40 – 65 cm	100	95	92
R= 65 – 120 cm	109	106	104

Table 1 : Average NIEL factors in the tracker (in MeV.mb).

These radiation fields are translated into a 1 MeV-neutron equivalent fluence, which is more convenient regarding the radiation tests (Table 2).

It should already be stressed that the NIEL factors are subject to large uncertainties as the damage functions of all particles over the whole LHC energy range are not well known or experimentally confirmed. Together with the uncertainties on the fluences, a safety factor of 1.5 to 2 should be applied to the 1-MeV equivalent fluence. Hence, as a general rule and for what concerns this thesis, it is usually considered that the inner tracker sensors have to sustain a fluence of 2.4 10^{14} 1-MeVn.cm^{-2} whereas outer tracker sensors one have to sustain 0.5 10^{14} 1-MeVn.cm^{-2} (0.8 10^{14} 1MeV-n.cm^{-2} in the worst outer tracker case). A very conservative approach has hence been considered.

TIB (averaged)

Radius (cm)	22	32	41	49	58
1-MeV Φ (10^{13} n.cm^{-2})	15.7 ±0.1	8.88 ±0.09	6.22 ±0.05	4.67 ±0.04	3.54 ±0.04

TOB (averaged)

Radius (cm)	75	85	95	105	115
1-MeV Φ (10^{13} n.cm^{-2})	2.9 ±0.1	2.58 ±0.05	2.36 ±0.05	2.2 ±0.06	2.09 ±0.06

TEC

Radius (cm)	75	75	75	75	75
Z (cm)	117	141	177	210	255
1-MeV Φ (10^{13} n.cm^{-2})	2.8 ±0.1	3.6 ±0.2	3.7 ±0.4	3.9 ±0.2	4.9 ±0.2

Table 2 : 1-MeV equivalent fluences as quoted in [15] and [16].

The radiation environment also presents another damageable effect on the electronics: highly ionizing particles events (known as “HIPs”). HIP events mainly affect the readout electronics as they can saturate it or cause permanent failures due to large charge depositions (up to 1000 MIPS) in a few channels. In the case of CMS tracker, Monte-Carlo simulations have evaluated the rate of such events, and the effects on the readout electronic were assessed with test-beams at the PSI (see e.g. [23] and [24]). The inefficiency of an APV chip induced by a HIP event is about 20 to 36 % during the 750 ns following the event (the deadtime being raised up to 350 ns). This may be regarded as something catastrophic, but the large number of channels and the presence of several layers of the tracker are such that the actual track reconstruction inefficiencies are at the percent level. The HIP will have therefore a negligible effect on the tracker regarding its Physics performances.

Chapter 2 : Silicon detectors

This chapter briefly describes the silicon particle detectors, being either diodes or microstrip detectors, and their behaviour under exposure to radiations. Some paragraphs of this chapter were already described in previous reports [28] but are further developed here.

We start with a description of the crystal structure of the silicon bulk, putting the emphasis on the lattice orientation, which bears some impact on the detector performances. Thereafter, we continue with the depletion mechanism, crucial to understand the detection principle of a semiconductor radiation detector. We finally add the features of a segmented detector (the surface and strip parameters). The evolution of the macroscopic properties of a detector under irradiation is then outlined in a very general way since results specific to CMS structures will be discussed in chapter 4. This chapter ends with a description of the CMS detectors and the quality assurance scheme applied by the CMS sensor group these last few years.

2.1. Properties of the crystal

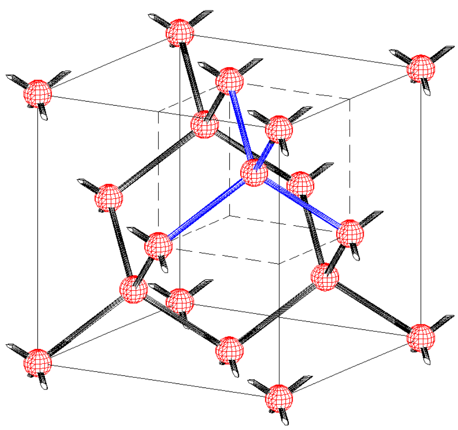

Fig. 13 : Diamond lattice structure.

The silicon crystal has the same lattice geometry as diamond, namely a face-centred cubic lattice, pictured in Fig. 13. In fact, most of the commonly used semiconductors (Silicon, Germanium, Diamond) present the same crystal geometry, but with different lattice sizes and energy gaps.

Although Silicon is very abundant on earth, it is rarely found in its crystalline form. Several crystal growth techniques have been developed to produce monocrystalline ingots, which will be used as the basic material for the production of detectors. These techniques will not be discussed here, but a good summary can be found in [32]. It is however important to mention at this point that, as the crystal is grown as an ingot, already two major characteristics of our future semiconductor detector are determined, namely the lattice orientation and the bulk resistivity.

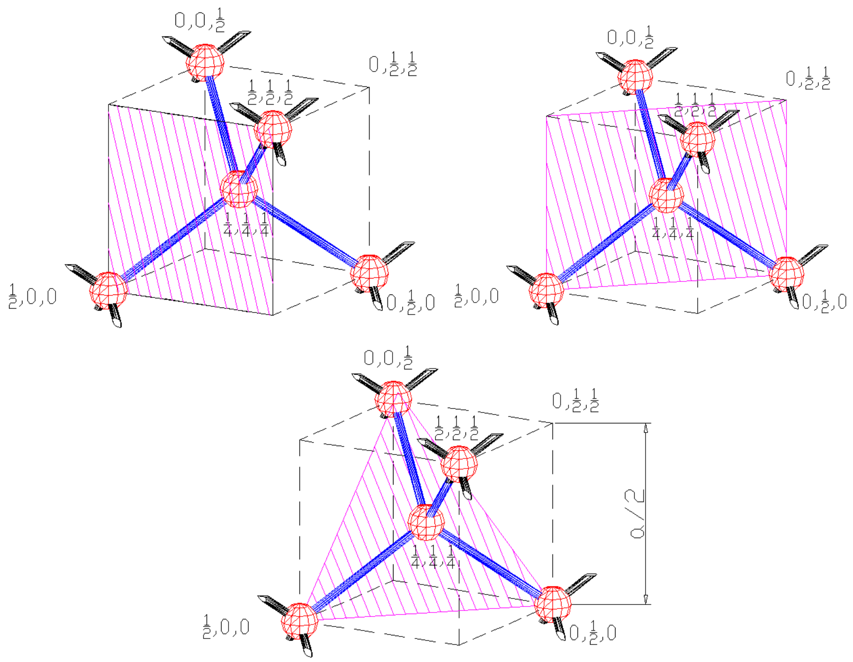

Fig. 14a, b, c: Respectively <100>, <110> an <111> lattice orientation planes (pictured in purple).

The lattice orientation of a wafer is determined by the orientation of the seed used to grow the ingot. The crystal orientation is named after the Miller indices* of the cutting plane (wafer surface). There are three possible

* The Miller indices are determined by first finding the intercepts of a plane with the three basis axes in terms of the lattice constants and then reduce these values to the smallest integers having the same ratios.

orientations for a detector, namely <100>, <110> and <111>, pictured above. One sees that the difference lies in the density of surface atoms near the cutting plane, and hence the density of unpaired electrons (dangling bonds). This will influence the surface parameters of the detector, as will be discussed when considering the CMS silicon sensors below.

The bulk resistivity (the initial concentration of defects/doping of the wafer) depends mainly on the crystal growth and purification technique. For detectors, as it needs to be as high as possible in order to reach a full depletion at a low voltage, the float zone technique seems to be the unique possibility so far as it is difficult to produce high-resistivity crystals with other techniques.

2.2. Principle of operation, characteristics

The basic principle of particle detection with semiconductor detectors is pretty similar to the ionization of a gas: a charged particle passes through the medium, exciting its constituents and creating free charge carriers that diffuse through the detector. When an electric field is applied within the detection volume, the negative charge carriers drift towards the anode (positive electrode), whereas the positive charge carriers move towards the cathode (negative electrode). Depending of the electric field, the device can also be operated in different modes (e.g. the avalanche mode), like the different regimes of a gas detector.

The comparison between gas and semiconductor detectors stops there. Big differences already arise with the nature of the charge carriers. In gas detectors, the freely moving charges are electrons stripped from the gas atoms on one side and their corresponding positive ions on the other. In semiconductor devices, if the negative charge carriers are also electrons that are relatively free to move across the lattice (with a given mobility μ_e), the positive charge carriers are not the created ions, which are locked on their lattice position. Instead, vacant positions left by electrons and created inside the lattice carry positive charges +e and are called "holes"; they can move between neighbouring atoms and behave like positively charged particles with a proper mobility μ_h. Let's then describe the basic principle of operation of a semiconductor detector.

For this purpose, it is usual to start by a short description of doping and a discussion of the simplest yet very important P-N junction structure.

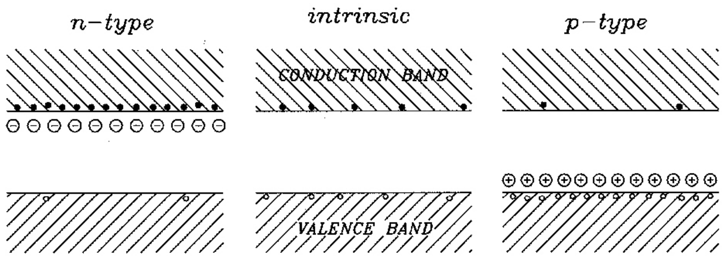

Fig. 15 : The shallow donors and acceptor levels in the band gap of silicon with the corresponding free charge carriers (from [2]).

P- and N-doped crystals are produced introducing tri- or pentavalent defects in the crystal. This raises the density of shallow donor (N-doping) or acceptor (P-doping) states which are almost always in an excited state due to their proximity to the conduction or valence band respectively (cf. Fig. 15). One then speaks of an extrinsic semiconductor. A PN junction is made by stacking a P-doped and a N-doped extrinsic crystals.

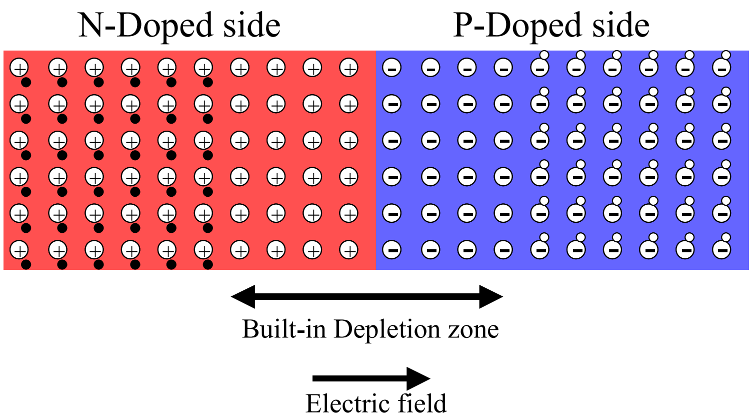

Fig. 16 : The built-in depletion zone of a PN junction and the direction of the resulting electric field.

Without the application of an external bias, such a device has free holes in the P-doped volume, and free electrons in the N-doped one. These recombine around the contact borders of the two volumes, hence creating a small built-in depletion zone (cf. Fig. 16). Initially neutral, this depletion zone becomes locally charged: one side (P-side) has a negative charge concentration, and the other side (N-side) a positive charge concentration. This depletion zone is interesting for its two main features:

1. There are no free holes or electrons, hence preventing further recombination of injected charge carriers within its volume

2. The electric field causes any charge within its volume to drift towards its borders (electrons to the N side, holes to the P side)

These two characteristics of the depletion zone are very interesting for particle detection: they prevent signal losses and help charge collection during the operation of the detector. More than this, due to recombination in undepleted areas, the depletion zone becomes the actual detection volume, it is hence standard practice to enhance the volume of the depletion zone by reverse-biasing the sensor. One generally wants to keep depleted the entire volume of the device to maximise the active thickness and to get the best signal/noise ratio.

The full depletion voltage is usually determined using the capacitance-voltage method. The boundaries of the depletion zone act like the two plates of a planar capacitance: with increasing reverse voltage (V), the distance between the planes increases and hence the bulk capacitance (C_{back}) diminishes. The relations linking the capacitance with the depletion depth is given below. A further discussion can be found in [2], [5] or even [28], we will only stress the fact that as the detector becomes fully depleted, its bulk capacitance becomes independent of the bias and a kink appears in the $1/C^2$ over voltage plot. The full depletion voltage of a planar diode is then given by (2.2).

In the following equations, q is the proton charge, ε and ε_0 define the dielectric constant, S the surface of the detector, V_{bi} is the built-in voltage and N_{eff} the effective doping concentration.

$$C_{back}(V) = \frac{dQ}{dV} = S\sqrt{\frac{q\varepsilon\varepsilon_0 |N_{eff}|}{2(V_{bi}+V)}} \qquad (2.1)$$

$$V_{dep} = \frac{q}{2\varepsilon\varepsilon_0}|N_{eff}|d^2 - V_{bi} \qquad (2.2)$$

The second main characteristics of a reverse-biased PN junction is its dark current, with a current density proportional to the depletion depth according to (2.3). The following symbols are also introduced: n_i is the intrinsic charge carrier density, τ_g the carrier generation lifetime, d_0 is the thickness of the built-in depletion zone and J_{leak} is the total dark current per unit area generated within the detector.

$$
\begin{aligned}
J_{leak}(V) &= -q\frac{n_i}{\tau_g}(d_{dépl} - d_{bi}) \\
&= -q\frac{n_i}{\tau_g}\sqrt{\frac{2\varepsilon\varepsilon_0}{q|N_{eff}|}}(\sqrt{V_{bi}+V} - \sqrt{V_{bi}})
\end{aligned}
\qquad (2.3)
$$

It is important, at this stage, to note that the ratio n_i/τ_g is also called the thermal generation rate; it is strongly dependent on the temperature and so does the leakage current according to equation (2.4) for a given bias voltage. It will be important to remember this relation when comparing the results obtained after irradiation at a temperature of –10 °C with those quoted in the literature and usually obtained at room temperature.

$$
\frac{J_{leak}(T)}{J_{leak}(T_{ref})} = \left(\frac{T}{T_{ref}}\right)^2 e^{-\frac{E_{gap}}{k_B}\left(\frac{1}{T}-\frac{1}{T_{ref}}\right)} \qquad (2.4)
$$

When a particle passes through a PN semiconductor device, it creates charge carriers pairs by ionizing the media. The energy required for the production of an electron-hole pair in silicon is about 3.6 eV. This is another advantage of semiconductor devices when compared to the 36 eV required on average to ionise a gas molecule. The number of generated charge carriers, as well as the Fano factor of the detection material, are crucial when considering the energy resolution of a semiconductor detector compared to any other type (the number of charge carriers being indeed the single parameter determining the statistical limit on energy resolution). We will however not discuss the energy resolution into further details here as we focus on the position sensitivity.

Indeed, the position resolution is a key element for building a tracker. The following paragraphs will hence introduce the features of a segmented silicon microstrip detector.

The two next figures show the layout of a typical CMS-silicon microstrip detector in respectively transverse and longitudinal views. Please note that we picture here only the AC-coupled version of a P^+-n-N^+ silicon detector and that there are many other sensor designs according to the wafer type, the biasing scheme and the charge carrier collection possibilities as the similar electron-hole mobilities (the saturation velocities are about 10^7 and $8.4\ 10^6$ cm.s^{-1} for electrons and holes respectively in intrinsic silicon) even lead to the opportunity to develop double-sided detectors. All these possible designs will not be discussed here since they are not used to build the CMS tracker.

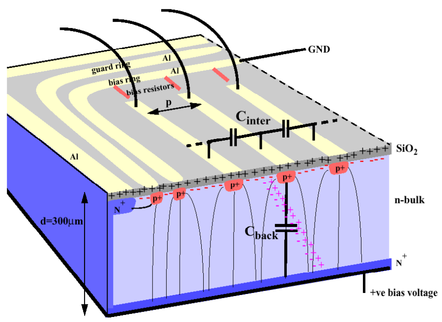

Fig. 17 : General layout of an AC-coupled microstrip detector [21].

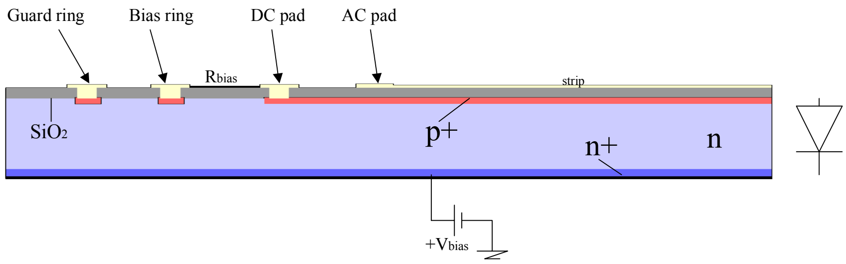

Fig. 18 : Longitudinal cut view of a silicon microstrip detector.

On the above figures, one sees the N^+ implantation, in contact to the backplane where the bias is applied. It prevents the surface current generated at the mechanical borders (cuts) of the sensor. The upper surface has the second bias contact (bias ring). The detectors are usually equipped with one or more guard rings to prevent breakdowns and leakage current between the N^+ implantation and the other surface structures due to the high voltage difference. The bias ring is connected to all strips, in this case via polysilicon resistors, to uniformly distribute a common potential and hence to define the electric field within the bulk of the detector. The resistors are in fact not connected to the surface aluminization of the strips but to the P^+ implants underneath. This is peculiar to AC-coupled detectors, where a P^+ implant forms a capacitance with the aluminization. Together with the bias resistors, these capacitances act as a high-frequency bandpass filter, allowing the acquisition system (DAQ) to react only to signal pulses without being fed by the leakage current of the detectors.

2.2.1. Charge collection and position resolution

The accuracy of the position measurement obviously depends first on the pitch of the strips. Using a digital readout, where the strip number is recorded as the crossing position of the particle, one achieves a precision of the order of $p/\sqrt{12}$, p being the strip pitch. But a higher accuracy can be reached with an analogue readout of the neighbouring strips, in which case the particle position is found by interpolation among the various strip numbers.

To assess the higher precision brought by an analogue readout, one has to have an idea of the pulse shape at the strips. Indeed, as mentioned above, when a particle passes through the detecting media and creates electron-hole pairs, these latter begin to drift within the bulk and are eventually collected either by the strips or on the backplane. The drift[*] of the charge carrier cloud depends on the type of the incident particle, but the pulse shape at the electrodes will not solely depend on the time spent by the charge carriers to reach the electrodes. There is also a current (i) induced on the electrodes as the electrons/holes drift towards or away of the electrodes at a given speed (v). The induced current plays a major role, and its value is given by the Shockley-Ramo theorem (2.5).

$$i = q\vec{v}.\overrightarrow{E_0} \qquad (2.5)$$

where E_0 is a function called the weighting field: it is the solution of the Poisson equation with a unit potential the concerned electrode, and 0 on every other one. A brief discussion about this theorem as well as a useful illustration can be found in [1].

In the presence of a magnetic field, the additional drift angle (called the Lorentz angle) due to the crossed electric and magnetic fields can be used to further improve the spatial resolution, as explained in ref. [15], section 2.3, in the case of the CMS pixel detector.

[*] A useful method to obtain a rough estimation of the width of the charge cloud to be collected by the strips can be found in [2], page 111.

2.2.2. Electrical properties of a strip detector

The leakage current of a segmented detector is correctly described by the above relations (2.3) and (2.4). Even after irradiation, the scaling of the leakage current remains valid, as will be shown in 4.2.2. But although the basic mechanism of depletion also remains the same, the capacitance-voltage behaviour is quite different. Indeed, the presence of strips at the upper surface of the detector implies a geometry of the electric field different from the one in a plane capacitor. This has been explained in a paper by E. Barberis et al. [26]. For a given effective doping concentration, a segmented detector will show a higher depletion voltage compared to a diode according to:

$$V_{dep,seg} = V_{dep,diode}\left[1 + 2\frac{p}{d} f\left(\frac{w}{p}\right)\right] \qquad (2.6)$$

where p is the pitch of the strip, d is the detector thickness and w is the strip width; f(w/p) is a function whose details are given in the above-mentioned article. The diode depletion voltage can be determined using equation (2.2).

It is important to note that the method for determining the full depletion voltage is not affected in any way by the segmentation of the detector: the plot of $1/C^2$ as a function of bias will also show the characteristic kink of the depletion voltage of the device. However, we will have to take this effect into account when using either the depletion voltage to determine the effective doping concentration, or its evolution under irradiation to compute the changes in full depletion voltage.

In addition to the bulk properties, a segmented detector has many surface characteristics that are of major importance when considering the overall performance of the device.

1. Coupling capacitances are a key element in charge collection. Their value should be as high as achievable to ensure a good charge transmission to the readout electronics.

2. Interstrip capacitances are the major contributor to the crosstalk between strips and noise. Interstrip capacitances can be used to improve the position accuracy in the case of a capacitive charge division readout. However high interstrip capacitances may cause deviations from linearity of the charge division between

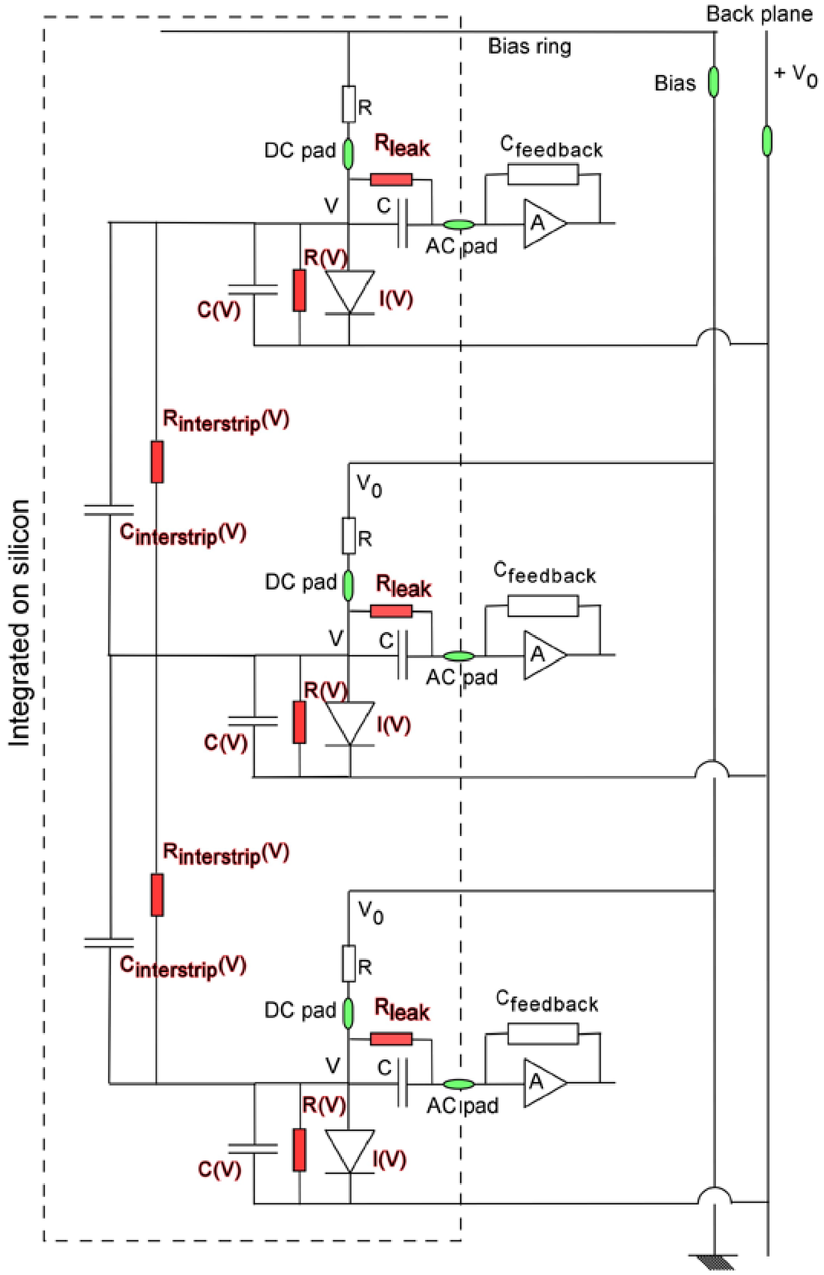

Fig. 19 : Circuit diagram of a silicon microstrip sensor.

two adjacent strips and generate in some cases a position-dependent accuracy. Interstrip resistances mainly contribute to the noise if their values are too low, hence also deteriorating the performance of the sensor.

3. Bias resistors have to be as uniform as possible across the device to ensure a uniform electric field within the bulk. Especially after irradiation, when the leakage current is high..

4. The overall surface quality of the sensor also plays a major role. For instance, a poor surface quality or a breakdown of the superficial oxide layer may lead to "pinholes". These are pictured as R_{leak} through which currents collected at the P^+ implant directly leak into the readout electronics, ruining all the advantages of an integrated AC-coupling.

The S/N ratio of a detector module depends not only on the sensor, but also on the readout electronics. Some general considerations regarding the noise of an AC-coupled detector can be derived from the electrical scheme pictured in Fig. 19:

1. Thermal noise: it is due to the thermal fluctuation of charge carriers present in the bulk, and proportional to $\sqrt{4kT/R_{poly}}$. Hence, the sensor should have high values of the bias resistor, but without compromising the field uniformity across the surface of the sensor.

2. Shot noise: the shot noise is due to the fact that the charge is quantified. In this case, noise is proportional to $\sqrt{2qI_{leak}}$.

3. Serial noise: Serial noise find its source in the readout amplifier and depends on its transfer function. It adds in quadrature to the thermal noise, and its value is proportional to sum of the capacitances seen from the input of the amplifier: the capacitive feedback of the amplifier ($C_{feedback}$) and the total strip capacitance composed of the coupling capacitance (C_{AC}), the interstrip capacitance (C_{int}) and the strip bulk capacitance (C_{bulk}).

4. Low-frequency noise: The origin of low-frequency noise, or Flicker noise, in detectors [30], and silicon devices in particular [31], is still not well-known. Empirical models exists, that show

that above a given frequency, pure white noise (thermal and shot noise) is observed.

More details about noise in detectors can be found in either [2], [29]or [30]. Very important results about the S/N ratio of a detector and its related electronics can be obtained by means of numerical simulations. In the case of CMS sensors, these have been reported in [33] and will be summarised later in the discussion about the design of the sensors.

About the surface parameters, the lattice orientation and number of dangling bonds play another essential role. Even though there are only little differences between <111> and <100> brand new devices, the lattice orientation: as a general rule, a low surface density of dangling bonds is an asset for the radiation hardness.

Despite the fact that the effects of the surface parameters on the detector performances have known tendencies, there are no general rules or recipe to design a detector: these considerations on the surface parameters of a sensor stress the importance of simulations and prototyping of the devices before any mass production. Highly critical in the case of the CMS tracker, this development phase is outlined in 2.4.

In addition to the stringent requirements on these parameters, it should also be stressed that all measurements of these characteristics should be performed in perfectly well-defined conditions. For instance, as a segmented detector is a complex network of resistances and capacitances, the frequency used by the LCR-meter to determine the capacitances plays a major role in the reproducibility of the results. The measurement of the interstrip resistances has also to take into account the depletion state of the sensor because the electric field near the surface plays a major role in the concentration of charge carriers nearby the strips. To cope with this issue in the context of the CMS QA scheme, a very detailed protocol has been fixed by the collaboration

2.3. Radiation-induced changes in detector properties

This section outlines the evolution of a silicon detector properties under irradiation. It is inspired from ref. [2] and [32], which are standard references in the domain.

2.3.1. Basic damage process

The very first damage process in the bulk is the creation of a Frenkel pair in the crystal lattice due to a primary knock on atom*. Being either light or heavy, charged or not, the incident particle kicks a silicon atom out of its position within the lattice, creating a vacancy-interstitial pair. The threshold for this process is 25 eV. Once knocked out of its position, the silicon atom can in turn, if energetic enough, create other defects on its own in a cascade process. The high concentrations of defects caused in this way are often called "clusters"**, as opposed to point defects caused along the track of an incident particle, as depicted in Fig. 20.

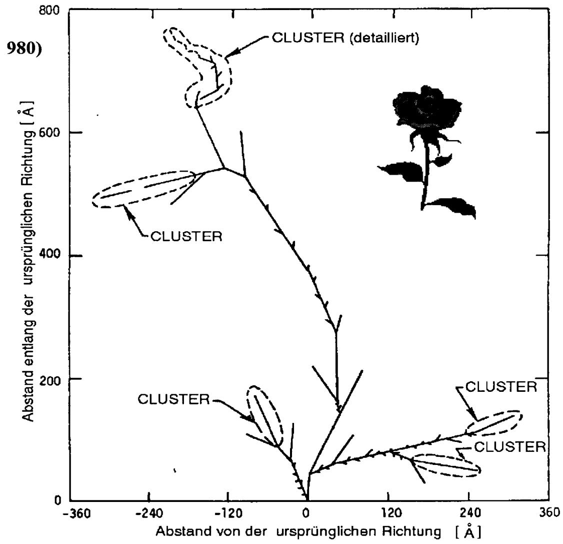

Fig. 20 : Basic damage cascade process caused after a PKA: the initial impact took place at location (0,0). Taken from the ROSE collaboration, [32].

Once created, all these primary defects move within the silicon bulk through a diffusion process and are likely to recombine in many different stable defects, inducing now irreversible damage which influence permanently the macroscopic properties of the detector. The reaction rate at

* Often referred as PKA.

** The defect concentration is computed to be as high as 100 defects in a 5 nm diameter volume.

which this process takes place is highly dependent on the temperature because of the defect mobility within the bulk of the sensor.

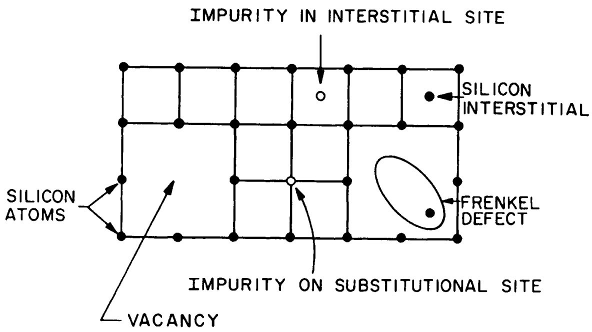

Fig. 21 : Simple defects in a 2-D crystal, from ref. [2].

There is an extensive nomenclature of these defects, based on the combination of simple defects such as vacancies (V), silicon interstitials (I), impurities (for which the symbol taken is often the chemical symbol of the interstitial atom), as described in Fig. 21.

These permanent defects are in fact recombination centres acting as electron or holes traps depending where their energy level lies inside the band gap. From a macroscopic point of view, the defects generate higher leakage current, modify the depletion voltage (changing the effective doping concentration) and diminish the charge collection efficiency by trapping either the electrons or holes created by the ionizing incident particle.

A further interpretation of the link between microscopic defects and macroscopic properties requires first to describe the evolution of these.

2.3.2. The NIEL hypothesis

Despite the complexity of reactions taking place in a semiconductor device when exposed to high radiation levels, first studies have demonstrated that the evolution of some macroscopic characteristics can be described using a relatively simple hypothesis: the NIEL* hypothesis according to which only the non-ionizing component of the total energy deposit within the device contributes to permanent damages. The spatial extension of the reaction cascade, as described above, and the complexity of the lattice perturbations are not taken into account.

* NIEL: Non-Ionizing Energy Loss.

The evaluation of the non-ionizing component is made by computing D, the displacement cross-section, also called the average displacement KERMA. For a given particle flux, this is done according to the following definition of a flux-weighted cross section (2.7):

$$D = \frac{\int_E \frac{d\Phi(E)}{dE} D(E) dE}{\int_E \frac{d\Phi(E)}{dE} dE} = \frac{\int_E \frac{d\Phi(E)}{dE} D(E) dE}{\Phi_{tot}} \qquad (2.7)$$

Where

$$D(E) = \sum_k \sigma_k(E) \int dE_r f_k(E, E_r) P(E_r) \qquad (2.8)$$

The last equation (2.8) is the expression of a macroscopic interaction cross section (or “damage function”) for a given particle interacting through different reactions within the device, $\sigma_k(E)$ being the cross sections of these reactions ; $f_k(E, E_r)$, the probability for an incident particle of energy E to produce a recoil energy E_r in a reaction of type k while the function $P(E_r)$ is the part of the recoil energy E_r deposited in displacements.

Expressed in MeVmb, this quantity D is usually normalized to the displacement cross section for damages produced by a 1 MeV neutron, quoted to be 95 MeVmb[¤]. The subsequent factor is then referred as κ, the hardness factor of the radiation field. It is then used to compare, scale and add fluences of different particle types and energies.

$$\kappa = \frac{D}{95 MeVmb} = \frac{\int_E \frac{d\Phi(E)}{dE} \kappa(E) dE}{\Phi_{tot}} \qquad (2.9)$$

[¤] 95 MeVmb is the value of the displacement function for 1 MeV neutrons, and is the most commonly used reference value although some rather use a value of 76.9 MeVmb which averages a bit around 1 MeV, because the displacement cross sections varies a lot in the vicinity this neutron energy (cf. [40]).

Where

$$\kappa(E) = \frac{D(E)}{95MeVmb} \qquad (2.10)$$

On the basis of this normalisation, a "real" particle fluence is expressed in its "1-MeV neutron" equivalent using (2.11):

$$\Phi_{eq} = \kappa\Phi_{tot} \qquad (2.11)$$

Compilations of the hardness factors can be found in references [22], [41] and [42]. Neutron coefficients taken from these references are illustrated in Fig. 22.

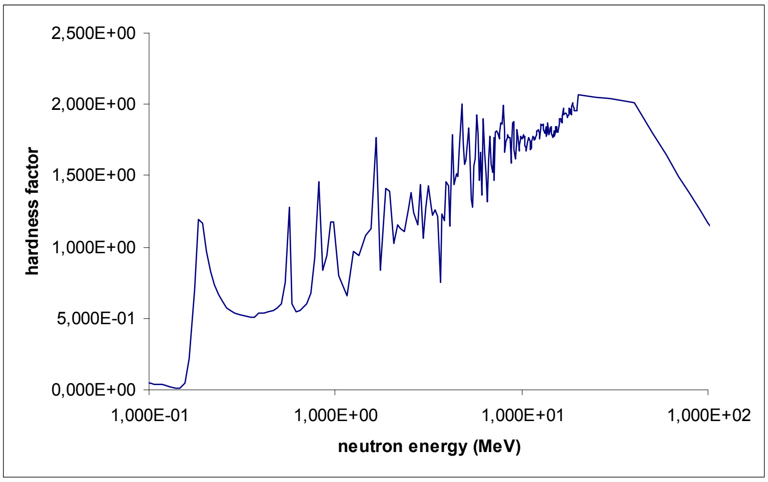

Fig. 22 : NIEL hardness factors in the case of neutrons from 0.1 to 100 MeV.

M. Huhtinen performed this normalization in the case of the radiation field present in the CMS tracker during its operation in [15], and updated it in [16]. This has been outlined in 1.2.2.

The success of this approximation is based on the fact that the strong dependence on particle type and energy of the interaction is smoothed out to a large extent by secondary reactions within the displacement cascade [2]. It therefore provides a good scheme to predict the evolution of the leakage current of a detector but failed however to explain various aspects of the changes in the macroscopic properties of the detector, such as the reverse annealing of the depletion voltage. The latter still requires further investigations on the microscopic defects produced during irradiation. This is illustrated by the fact that oxygenated silicon detectors are less subject to damage when exposed to the same 1-MeV equivalent fluence of protons than when exposed to neutrons.

2.3.3. Evolution of detector properties

Now that the basic processes of damage within a semiconductor sensor have been shortly discussed, it is time to consider how they affect the macroscopic properties and the functionality of the detector. The bulk parameters such as leakage current and depletion voltages are the most affected characteristics of the sensor and will be addressed first. The surface structures will be discussed thereafter.

2.3.3.a. Leakage current

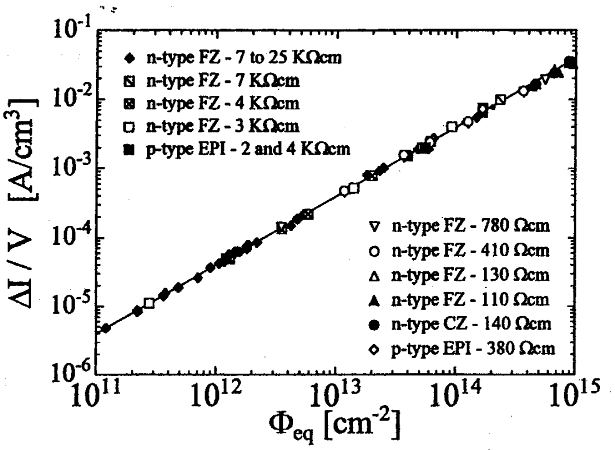

Fig. 23 : Increase of the leakage current density as a function of the fluence, measurements performed after 80 minutes of annealing at 60 °C (taken from [32]).

For a long time now, it has been shown that the leakage current increases linearly with the 1-MeV equivalent fluence (Fig. 23). This effect has been found to be material-independent (manufacturing process, initial doping concentration, p or n-type) and particle-independent (irradiations with neutrons or charged particle).

It has been mentioned above that the frenkel pairs, initially created by PKA, are mobile within the bulk and recombine to create stable defects. It is then no surprise that the electrical properties of a sensor further evolve after irradiation, even if not submitted to any additional fluence. In the case of the leakage current, the same annealing behaviour is observed for all detector materials and all particle types. Although the time constants for this annealing highly depend on the annealing temperature (Fig. 24), the current increase rate is hence found to be the characteristic which best follows the NIEL hypothesis for any incident particle type.

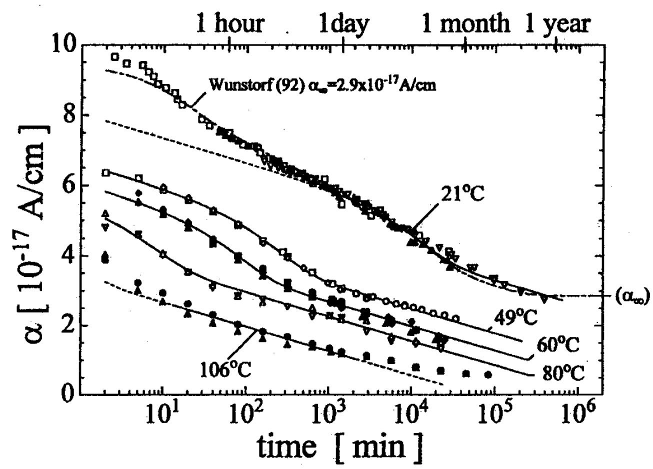

Fig. 24 : Leakage current annealing behaviour after irradiation: α is the leakage current of the detector divided by its volume times the 1-MeV equivalent fluence it has been submitted to (from [32]).

As a consequence of the annealing behaviour, the measurements of the leakage current after irradiation have to be made within careful conditions, to allow further comparisons. This is an additional constraint on the post-irradiation tests in order to ensure the reproducibility of the results. From the leakage current point of view, a 15-day annealing at room temperature (21 °C) is equivalent to 80 minutes at 60 °C. This standard annealing step, widely used in literature, will also be performed for the CMS tests.

2.3.3.b. Depletion voltage

Compared to the leakage current, things get more complicated when considering the depletion voltage. Indeed, the effective doping concentration does not present a simple linear evolution with the fluence combined with a beneficial annealing afterwards. Considering a n-type bulk, the damage behaviour presents rather a combination of exponential decrease of the initial donor concentration, combined with a fluence-proportional damage that anneals both beneficially and adversely.

The current parameterization of this evolution is known as the Hamburg model, developed by the RD48 collaboration. It uses the NIEL hypothesis as a starting point, but classifies bulk damages in four categories, as mentioned above:

1. The first effect of radiation is an apparent donor removal, the donor removal rate being proportional to the donor concentration, this contribution has an inverse exponential form;

2. The introduction of stable damage is proportional to the fluence, and quantified by an introduction rate g_c;

3. g_a quantifies the introduction of damage that will beneficially anneal out. This annealing also presents an exponential time dependence whose time constant depends on the temperature at which the device is stored. For instance, the time constant vary from about a year at –10 °C, down to 2 minutes at 80 °C.

4. The last term is the reverse annealing contribution to damage. The introduction rate is noted g_Y and the time dependence also depends on the temperature: from several hundreds of years at –10 °C to around 92 minutes at 80 °C.

Equation (2.12) gives the whole picture of the Hamburg model, with all effects and including annealing. One can distinguish the various terms in the same order as mentioned above, with the first term representing the initial doping concentration minus the donor removal and the second term representing the fluence-proportional contributions of stable damage, beneficial annealing and finally reverse annealing.

$$N_{eff}(\Phi_{eq},t_a,T_a) = N_{eff,0}\left(1-r(1-e^{-c\Phi_{eq}})\right) - \Phi_{eq}\left(g_c + g_a e^{-\frac{t_a}{\tau_{T_a}}} + g_y(1-e^{-k_{T_a}t_a})\right) \quad (2.12)$$

The dose evolution of this relation is pictured in Fig. 25 whereas Fig. 26 illustrates the temperature annealing.

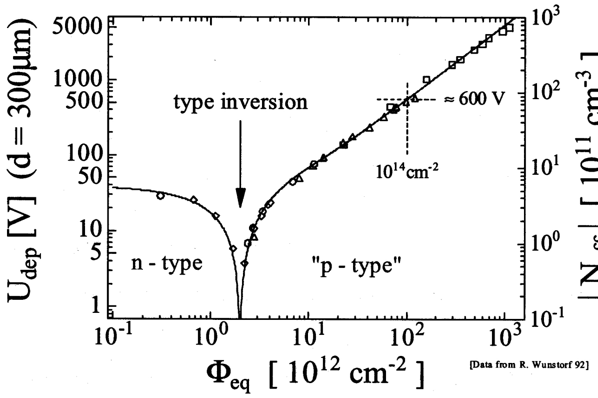

Fig. 25 : Typical evolution of the effective doping concentration of a n-type initial bulk, as a function of the fluence, for a given annealing state. From ref [32].

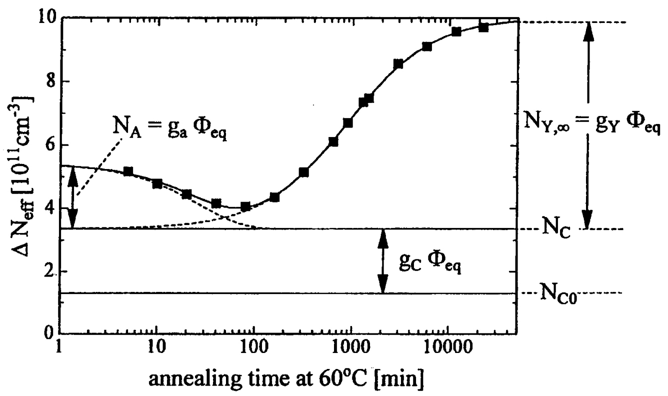

Fig. 26 : General scheme of the post-irradiation effective doping concentration evolution under annealing. From ref [32].

A compilation of all the experimental time constants can be found in [32].

The behaviour of the depletion voltage of a detector under irradiation puts an emphasis on the limitations of the NIEL hypothesis. Indeed, here the effective doping concentration does not present the same evolution for all materials and particle types. One of the most striking effect is the proton-neutron puzzle: for the same initial resistivity, an oxygenated detector will show a higher resistance to neutron fluences, compared to a non-oxygenated one. This effect isn't observed if both detectors are irradiated with protons.

Hence, the NIEL hypothesis is still useful if one knows how a given material reacts to radiations, but a more fundamental approach based on the study of the microscopic defects induced within the bulk has to be used if one wants to know what happens. Such studies, requiring instruments such as deep level transient spectroscopy (DLTS) or thermally stimulated current (TSC) are being carried out by e.g. the RD50 collaboration.

2.3.3.c. Surface structures

All the properties studied so far are bulk properties of the detector. Surface properties, also affected by radiation are critical regarding the detector operation. The trapped charges at the crystal boundaries play indeed an important role as far as resistances and capacitances are concerned. But the surface of the detector is, in most cases, covered by an insulator (SiO_2) and it can hence no longer be considered as a semiconductor crystal.

The damage mechanism is a bit different within an oxide: displacement damage is not the only permanent effect anymore and ionization comes in front of the scene. First, it is important to notice that the band gap is higher for an insulator (for SiO_2 for instance it is 8.8 eV): the emission of captured charge to the conduction band is therefore almost impossible. Then, the crystal/oxide region is a high defect density zone, and charge trapping by this defects plays an important role. Also, the mobility of electrons and holes are very different for insulators. All these effects combined have, as a consequence, that radiations can change the charge state of the insulator.

A consequence of this is that highly-penetrating particles (e.g. neutrons) produce less ionization and hence cause less surface damage than short range ones (X-rays, charged particles). Protons for instance affect more the surface of a detector than neutrons, and this has been seen during the CMS tests when comparing the radiation damage caused by protons in Karlsruhe with the neutron damage caused in Louvain-la-Neuve. This is a further argument for the above-stated complementarity of neutron and proton irradiations

But, besides this qualitative interpretation of damage at the detector surface, there are only few studies about the evolution of the surface structures of microstrip detectors under heavy irradiation. And it is difficult to foresee how these structures will evolve in a quantitative way. One of the reasons for this is that segmented detectors show a wide variety of designs, and hence it is difficult to disentangle general trends for modelling the evolutions under irradiation. Also, in many cases, these structures are, in fact, only slightly affected by irradiation. A study of the evolution of the surface parameters of the CMS sensors under neutron irradiation is carried out in chapter 4. The bad news are that in general the variations go in the way of a deterioration of the performances of the detector (bias resistors, interstrip resistances and coupling capacitances decrease whereas interstrip capacitances increase); the good news being that these variations leave the sensors within the specifications for a good tracking performance.

2.3.4. Correlations between microscopic defects and macroscopic properties

This work focuses on the evolution of the macroscopic properties of a silicon microstrip sensor under irradiation. But, as the annealing picture for both the leakage current and the effective doping concentration have been described, it is now interesting to give a short summary of what is the microscopic picture, and what could be the links between both.

At the microscopic level, impurities are named upon the atoms and type of defects they involve. From the electrical properties point of view, neutral defects have no influence on the semiconductor. This is the case for some combinations involving carbon atoms, whether on a lattice node or not.

Electrically charged defects are energy states located within the band gap. Like for the initial doping, these states can be close to the conduction or valence band (shallow defects). At the contrary, deep levels are close to the midgap.

The concentrations of defects as a function of the detector's annealing state have been studied in careful studies. They have pointed towards the fact that some of these affect the leakage current, whereas others affect the depletion voltage.

For instance, a very good candidate to be responsible for the leakage current increase is the divacancy (VV) and some of divacancy-related defects. This could explain:

- Why the alpha parameter does not depend on the bulk material type: divacancies are the dominant primary defects, depending on the lattice deterioration and not on a subsequent recombination.

- Why the leakage current shows only beneficial annealing: divacancies are very likely to recombine with other impurities or interstitial atoms: the concentration of divacancies can only drop, and hence the leakage current. The annealing curve could then adequately be described by means a sum of decreasing exponentials, each describing the different recombination possibilities for divacancies.

As far as the effective doping concentration is concerned, new microscopic candidates appear. For instance, the V_2O defect. As a complex defect made of a divacancy and an oxygen impurity in the bulk, it can be formed after irradiation. Such recombination mechanisms are thought to be the source for the following effects:

- Reverse annealing of the effective doping concentration: during beneficial annealing, primary defects concentration drop, whereas the reverse annealing, due to less probable recombinations, takes longer.

But a detailed knowledge of the microscopic evolution can also put some light on effects that cannot be explained by the simple NIEL picture:

- the so-called "proton-neutron" puzzle in oxygenated detectors. Oxygenated detectors have shown lower post-irradiation depletion voltages than standard silicon ones when irradiated by a proton flux. This could be explained by the different distribution of primary defects within the bulk for proton/neutron irradiations. Neutron irradiation produces mainly concentrated clusters, as opposed to proton irradiation where primary defects are spread along the entire particle track. This difference in initial defect concentrations can lead to different microscopic kinetics: the production of the electrically inactive V_2O_2 could be enhanced to the detriment of V_2O in the case of proton irradiation.

In the case of the CMS Irradiation Quality tests programme, the experimental result have demonstrated that standard silicon shows the same behaviour under proton and neutron irradiations. But still, this short summary stresses one more time that it is essential that both types of irradiations are performed for monitoring the radiation hardness of the CMS silicon sensors.

Furthermore, if there was the need for an additional argument in that sense: another major difference arises when considering the surface damage. Surface structures are less affected by radiations than the bulk of the sensor, but the damage mechanism is believed to be of a completely different origin as surface damage is mainly due to trapped charge and hence ionization, as opposed to non-ionization for the bulk. A proton irradiation will for sure induce a lot of ionization on the surface, whereas neutrons not.

2.3.5. Comments on bias and irradiation rate

A frequent question about radiation hardness tests to study the survival of detectors in a harsh environment is the influence of the dose rate. Is a fast irradiation performed inside a nuclear reactor or near an accelerator really equivalent to a 10-year operation at the LHC?

Whereas there is no detailed study yet about the flux dependence of strip parameter damage, irradiations have been carried out by a Slovenian group to study the impact of flux on bulk damage [34]. Their conclusions mainly deal with the full depletion voltage: it is found to be flux-independent over a wide range of fluxes from $2\ 10^{8}$ to $5\ 10^{15}$ $n/cm^{2}s$ for the same integrated fluence.

The bias-dependence of the damage is another important question related to the irradiation tests. Indeed, the high fluxes used during radiation hardness tests usually prevent the biasing of the devices during the irradiation themselves, whereas they will obviously be biased during operation at LHC. One can intuitively imagine that any electric field within the bulk of a detector may have an impact on the electrically charged defects and their kinematics.

Very few studies of the impact of biasing during irradiation have been carried out so far, among these the study performed at Lubljana (Cindro et al [35] and [36]), Mikuz et al [37]). Their main conclusions show an effective dependence of the damage on the bias. Although the leakage current seems unaffected, the full depletion voltage tends to increase when structures are biased:

- Right after irradiation, the biased diodes (those that were kept biased) exhibit a much higher depletion voltage than the other ones.

- This difference tends to vanish on diodes on which bias is switched off (after ~100h).

- Also, samples that were kept unbiased during irradiation show an increasing V_{dep} when kept biased for a long time. Hence, both the diode samples that have been biased and unbiased during irradiation exhibit this effect.

This increase of the depletion voltage is thought to come from a bistable defect, which is introduced in the structure whether biased or not during irradiation. The study estimates its impact to be as high as 80 V at the end of the detector lifetime.

The influence of bias in the case of our tests within CMS will be discussed and compared to these results in 4.2.1.

2.4. CMS sensors designs

The construction of the CMS tracker requires many different detector designs to fulfil the resolution requirements and ensure a uniform evolution of the electrical properties of the detectors under the radiation field. To design all these geometries, a series of multi-geometry detectors have been fabricated [38].

As a starting point, the well-known and generally used P^{+}-n-N^{+} scheme has been kept, with an integrated AC-coupling and a polysilicon resistor-biasing scheme (cf. Fig. 17, above).

The other parameters like capacitance, crystal orientation or initial wafer resistivity had to be studied further to ensure the reliability and lifetime of the detectors in the LHC environment. The specific R&D will not be fully described here as it is not part of our work, but the main results will be briefly discussed since they have implications on the design of the tracker and the results of irradiation tests.

A CMS R&D study [38] has been carried out on specific structures that have different pitch values, covering the range foreseen for the tracker, and which have various implantation width over pitch ratio. Each of these structures has been produced with different crystal orientations and initial resistivity. Some of these test sensors have been exposed in the CERN PS irradiation facility with 24 GeV protons for radiation hardness testing.

The pitch (p) and strip implantation width (w) interplay and have an impact on the backplane and interstrip capacitances. With irradiation, the backplane capacitance is found to decrease whereas the interstrip capacitance increases. This increase is a function of w/p only. The ratio w/p has been subsequently tuned to minimize the variation of the total strip capacitance (backplane+interstrip) variation. This is a major result as numerical simulations of the sensors have shown that this strip capacitance is the key feature for the noise of the detector : it dominates the serial noise discussed above. As a further consequence, for modules composed of 2 daisy-chained sensors, it implies that the resulting noise will also increase, requiring the thickness of these sensors to be increased. This is the reason why you have thicker sensors in the outer part of the tracker.

The performances of <111> and <100> oriented substrates have also been compared. Although they were similar before the radiation tests, the interstrip capacitances of <111> ones raises more with fluence than the other, as reported in [33]. This result is highly dependent on the bias voltage and operation frequency of the LCR meter, but is one of the main reasons to choose the <100> orientation. As mentioned above, it is thought to be due to the amount of dangling bonds (atoms at the surface of the silicon wafer), which is smaller in this particular orientation.

The depletion voltage is initially determined by the resistivity[¤] and the thickness of the wafer: the higher the resistivity, the lower the depletion voltage; the higher the thickness, the higher the depletion voltage. One might therefore consider the use of the highest achievable resistivity, but this will make the biasing easy only at the beginning of detector's lifetime, as the bulk type inversion process will occur soon in the radiative environment encountered at the LHC. Indeed, with a detector built on a very high resistivity wafer, we would end up with higher biasing needs due to the subsequent rise of the depletion voltage. The problem of the bulk type inversion is even more important as the junction moves from the front to the backplane; hence the detector needs to be always fully depleted to avoid the recombination of charge carriers and signal losses. Therefore, the initial resistivity of the wafers has to be carefully chosen in order to get final depletion voltages similar to the initial ones. This is done using simulations of the radiation field at the LHC, normalizing it with the NIEL approximation and applying the Hamburg model to take into account the variations in effective doping concentration and thermal annealing effects during the maintenance periods[*]. A typical example of such simulation is pictured on Fig. 27. To cope with this issue when building the CMS tracker, it has been divided into 2 volumes, inner and outer ones, with different resistivities and thicknesses (1.5-3 kΩ.cm and 320 μm for the inner part, >4

[¤] The resistivity is linked to the effective doping concentration according to the relation $\rho = \frac{1}{eN_{eff}\mu}$

[*] It is often assumed that the CMS tracker will be kept cold at –10 °C all year long, excepted for an annual period of 30 days at higher temperature for maintenance.

kΩ.cm and 500 μm in the outer zone) to keep the uniformity of biasing as constant as possible across the whole sub detector.

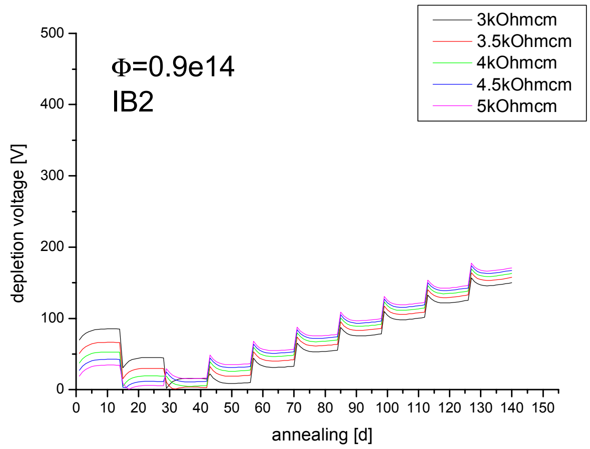

Fig. 27 : Simulation of the evolution of the depletion voltage as function of the initial resistivity, irradiation fluence and annealing time at LHC, for inner barrel CMS tracker sensor of different initial resistivities (taken from [44]).

In parallel to the issue of the depletion voltage, the sensor must have a good stability of the high voltage and must avoid breakdown. As the acceptance criterion for the depletion voltage at the end of the detector's lifetime is 300 V, the minimal voltage for stability against bulk breakdown has been set to 500V and is guaranteed by a guard ring. Small shorts between strips can occur as the field increases with overdepletion. To avoid them the metallization of the strips is designed wider than the implantation width. Since the oxide breakdown field is higher than the crystal breakdown field[¤], the metal overhang ensures a higher breakdown stability of the sensor. This will keep the S/N ratio of the modules as good as possible after irradiation.

[¤] The breakdown voltages for the silicon crystal and Silicon oxide, quoted in Table 26 and Table 27, are respectively of about 3 10^5 V/cm and between 5 and 8 10^6 V/cm.

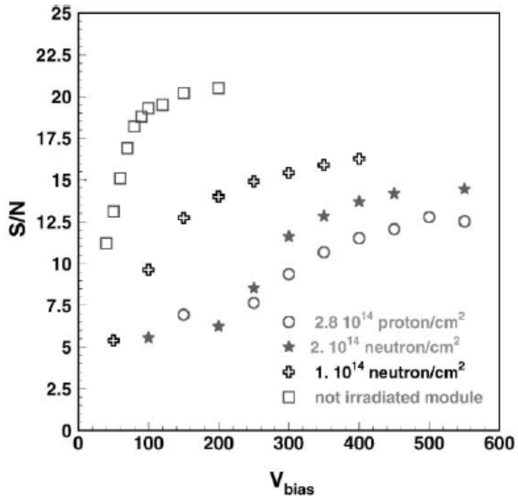

Fig. 28 : Signal to noise ration of irradiated CMS R&D structures (from [39]). The Breakdown resistance of the detector is clearly shown here as a crucial characteristic of the detector as the best ratio is obtained at high bias.

The enhancement has also proven to be better on <100> than <111>-oriented detectors, making it an additional argument for the choice of the first orientation.

In the case of CMS sensors, a rough estimation of the width of the charge cloud generated, without any magnetic field applied, is given by e.g. [2], p111.

	L1 (mm)	L2 (mm)	height (mm)	thickness (mm)
IB1	63,3	63,3	119,0	0,32
IB2	63,3	63,3	119,0	0,32
W1tec	64,6	87,9	87,2	0,32
W1tid	63,6	93,8	112,9	0,32
W2	88,2	112,2	90,2	0,32
W3	64,9	83,0	112,7	0,32
W4	59,7	73,2	117,2	0,32
OB1	96,4	96,4	94,4	0,50
OB2	96,4	96,4	94,4	0,50
W5a	98,9	112,3	84,0	0,50
W5b	112,5	122,8	66,0	0,50
W6a	86,1	97,4	99,0	0,50
W6b	97,5	107,5	87,8	0,50
W7a	74,0	82,9	109,8	0,50
W7b	82,9	90,8	90,8	0,50

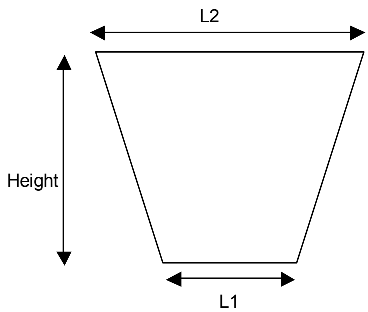

Table 3 : The different CMS sensor designs.

2.5. Qualification procedure for the CMS tracker sensors

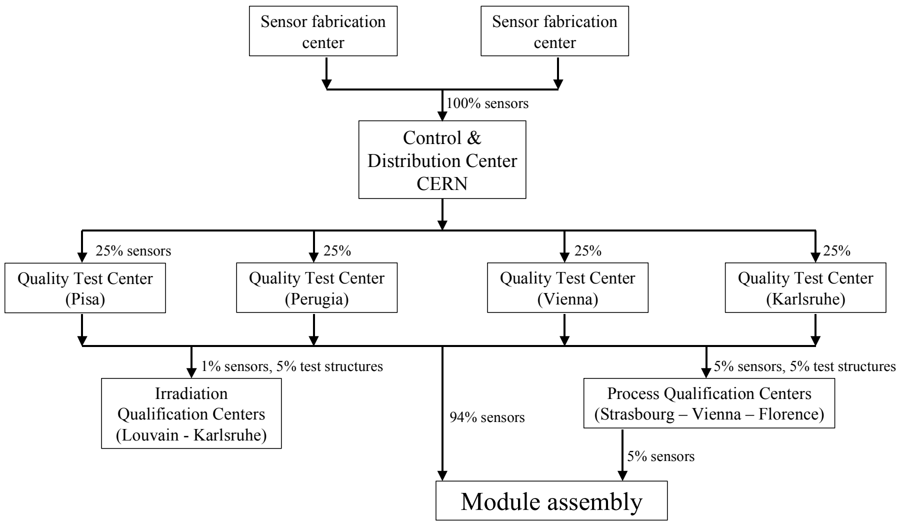

Fig. 29 : The CMS silicon sensor qualification scheme. This work is part of the tasks belonging to the Irradiation qualification centers.

The radiation hardness tests performed by the CMS silicon sensor group (cf. 3.3) are to be placed in the context of a broader quality assurance scheme to which many institutes collaborate [45]. Shown on Fig. 29, this rather complex procedure is required as the tracker will be made of several thousands of sensors and because the collaboration is expecting uniform properties of the silicon modules across the whole sub detector.

Each phase of the qualification procedure is well identified from the other ones and each institute, whether quality test center (QTC), process qualification center (PQC) or irradiation qualification center (IQC), has its own well-defined role and acceptance criteria for the different tests. Besides the sensor qualification scheme, there are also bonding tests which check that the sensors can easily be connected to the associated electronics via the pitch adapter.

	Test	Acceptance criteria
Global	IV	I_{leak} < 100 nA/cm^2 at V_{bias} = 500 V, V_{break} > 500 V
	CV	100 V < V_{dep} < 250 V
Strip by strip	Pinhole measurement	Current through dielectric less than 1 nA
	R_{poly}	Average value between 1 and 2 MΩ, with stdev < 0.3 MΩ
	Strip leakage current	I_{leak} < 500 nA
	C_{ac}	1.2 – 1.3 pF/cm/µm (normalized to the length of the strip and width of implantation)
	Total defect strips	< 1%
	(Strip parameters tested on a fraction of the strips only)	

Table 4 : Tests performed on sensors by quality test centres, and the corresponding qualification criteria (cf. [46]).

The quality test centres check the overall manufacturing quality by making full tests on a sample basis. There is in principle no need to test all sensors, but a sampling is justified as the characteristics may vary from batch to batch. In this context, the QTCs test all batches and, if these pass the tests, distribute samples of structures and sensors to the other test centres. The checks made at this level are an optical inspection of the sensors and an electrical check covering CV, IV, a strip scan to detect any pinhole and measurements of the strip leakage current, its bias resistor and coupling capacitance. The collaboration fixed acceptance criteria (cf. Table 4) on all the measured values and can reject the sensor on a basis of the CV-IV values as well as the number of defect strips.

The process qualification centres use the mini sensor and various structures built on the silicon wafer to monitor the stability of a number of parameters related to the processing of the wafer (e.g. oxide quality and breakdown characteristics, aluminium or implant resistivity, cf. Table 5). They also perform long-term stability tests.

Measurements	Acceptance criteria
CV	100 V < V_{dep} < 250 V (also depends on resistivity)
IV	I_{leak} < 100 nA/cm^2 at V_{bias} = 500 V, V_{break} > 500 V (test performed at room temp.)
C_{int}	C_{int} within 10 % of the parameterization
R_{int}	> 1 GΩ
R_{poly}	Between 1 and 2 MΩ, stdev < 0.3 MΩ
R_{p+}	< 200 kΩ/cm
R_{Al}	≤ 18 mΩ/cm^2
C_{ac}	> 1.2 pF/cm/µm
V_{break} of C_{ac}	> 120 V
I_{diel}	< 1 nA (at 120 V)

Table 5 : Summary of the measurements and acceptance criteria for the process qualification center (PQC) tests (cf. [46]).

In parallel to the PQC tests, radiation tests are performed by the two IQCs. The latter are in fact ageing tests and hence destructive tests. For this reason, mainly test structures have been tested (5 % of the production), along with a small percentage of sensors (1 %). Dispatched over two IQC, it nevertheless corresponds to more than 120 sensors and 600 test structures for each centre. After all the improvements we made to the irradiation setup, we were able to put simultaneously 16 test structures and 4 sensors maximum in the beam per irradiation. At a rhythm of about one irradiation per month during the beam time periods of the cyclotron we tested more than 180 structures during 2004. This is however too small regarding the total amount of devices to be tested. As there was no possibility to get more beam time, it has been decided to irradiate structures from as many different batches as possible. The results and their compliance to the acceptance criteria (Table 6) have to be assessed regarding the fluence that the devices have undergone.

Therefore, the depletion voltage and leakage current are studied and compared to literature using the NIEL approximation. In this way, one can estimate the radiation hardness of the sensors by simulating the LHC environment.

Test	**Acceptance criteria**
CV	V_{dep} < 250 V (+ Hamburg model)
IV	$\alpha \sim 3.5\text{-}4.5\ 10^{-17}$ A/cm V_{break} > 500 V
I_{strip}	Detect leaky strips on a sample basis
C_{int}	< 1.2 pF/cm
C_{ac}	> 1.2 pF/cm/µm
R_{poly}	between 1 and 2 MΩ, stdev < 0.3 MΩ
R_{int}	> 20 MΩ

Table 6 : Criteria for the irradiation qualification (IQC) tests.

Chapter 3 : Experimental setups

This chapter is aimed to describe the two major experimental setups used for silicon detectors radiation hardness testing in Louvain-la-Neuve. First, the electrical test bench will be addressed and second, the irradiation setup around the intense fast neutron beam line. A third section will develop some peculiar aspects in the case of the CMS tracker sensors studies, such as the irradiation and test protocol. Additional equipment is presented in the annexes.

3.1. Electrical characterisation setup

The large amount of sensors and structures to be tested for irradiation qualification of the CMS tracker silicon microstrip detectors requires the use of an automatic test bench. This latter must be designed in order to perform a complete electrical characterization of a device with as less user interventions as possible. It also has to be flexible enough to cope with the several sensors designs and versatile enough to allow quick implementations of special measurements.

Among the measurements possible on a segmented semiconductor detector, CMS focuses on the macroscopic characteristics and functionalities: CV, IV, strip parameters like bias resistors, strip leakage current, coupling and interstrip capacitances, interstrip resistances. Besides these properties, common to all microstrip sensor designs and test structures, additional measurements like CV and IV on diodes, inspection of the oxide layer quality through a MOS capacitance measurement have been added to the program.

The following sections will first describe the setup and then give more details on some specific hardware-related problems before entering the details of the performances and the obtained measurement accuracy.

3.1.1. Instrumentation, acquisition program

In Louvain, the electrical test bench is built around a Karl SüSS PA-200 semi-automatic probe station (shown below on Fig. 30). An especially engineered chrome plated steel plate is placed on top of the chuck. It has thin vacuum grooves to maintain the device during the whole tests and movements and provides a good electrical contact to the backplane of the device.

The chuck is temperature-regulated by a cooling loop and additional peltier elements. Methanol, used as cooling fluid, is kept at low temperature (-5°C) by a Huber cooling plant located outside the probe station clean room. It is kept at a constant temperature whereas the peltier elements ensure the accurate temperature setting and stability. This system is able to cool the chuck down to at least –40 °C and heat it up to 100 °C.

The light-tight enclosure around the chuck is continuously flushed with dry air to avoid any condensation on the device under test during low temperature measurements.

The monitoring of the test environment is made via he use of an active relative humidity sensor and a passive Pt100 resistor housed in the chuck to read its temperature. Special care has been taken to the reading of this latter resistor as the cables used to connect it have an influence on the measurement itself due to their specific resistivity. A correction based upon the length of the cable has been introduced in the acquisition program.

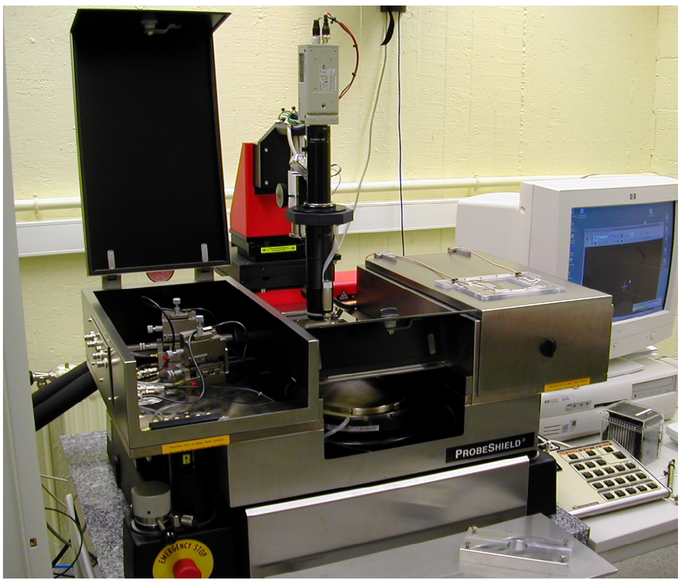

Fig. 30 : The semi-automatic Probe station.

Besides the biasing connection on the chuck (backplane contact, mentioned above), three needles and one additional (directly attached on the plate and pictured on Fig. 31) surround the device to ensure all the electrical connections required. The use of a probe card has been envisaged, but ruled out due to the many different designs to be handled by the same setup.

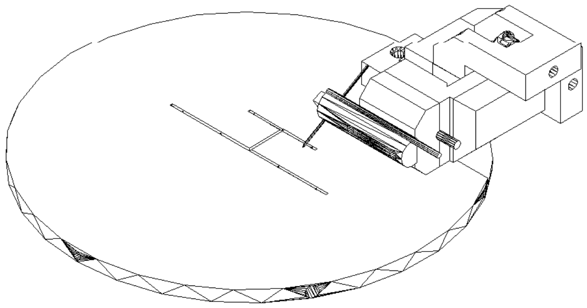

Fig. 31 : The lab-made chrome plated chuck and its fixed needle.

To permit an automated test sequence (composed of many different type of measurement), a switching matrix (cf. Fig. 32) is used to connect the needles to all instruments. Among these, the setup comprise a Keithley 2410 sourcemeter to bias the devices; a Keithley 6514 electrometer to accurately measure currents trough sensors, detect shorts and calculate the resistor's impedances; an Agilent 6614C low voltage source and a 4284 LCR to measure capacitors. This latter can be connected either directly to the needles using the switching matrix or trough a lab-made decoupling box to perform capacitance-voltage ramps, requiring the mixing of both the HV source and LCR measurement signal on the same needles.

The acquisition instruments, the probe station movements as well as the temperature of the chuck are all controlled by GPIB using a unique acquisition program, written under LabVIEW®. After a procedure meant to load the structure to be tested in the probe station (including pitch parameter calculation to allow the program to make accurate movements from strip to strip), the user interface allows choosing the measurement parameters (e.g. the ramping scheme) and the tests to be performed. The results are plotted at the end of each test and a separate file can be written on demand. Environment parameters such as temperatures or current position on the device are also shown.

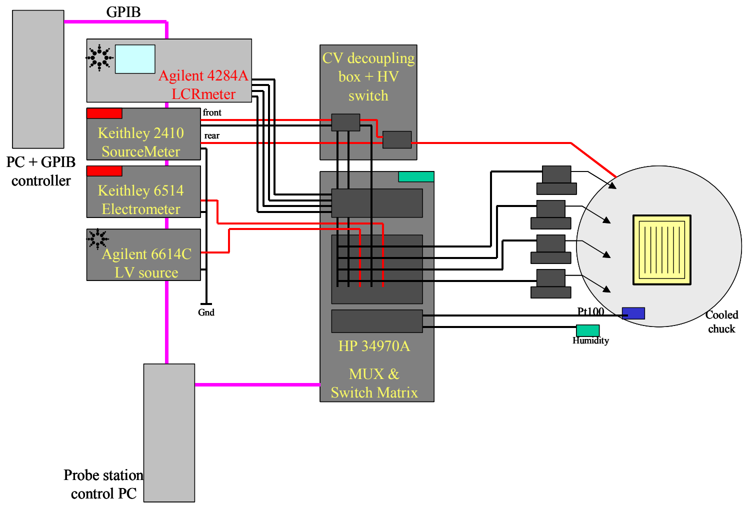

Fig. 32 : Schematic view of the instruments and electrical connections around the probe station.

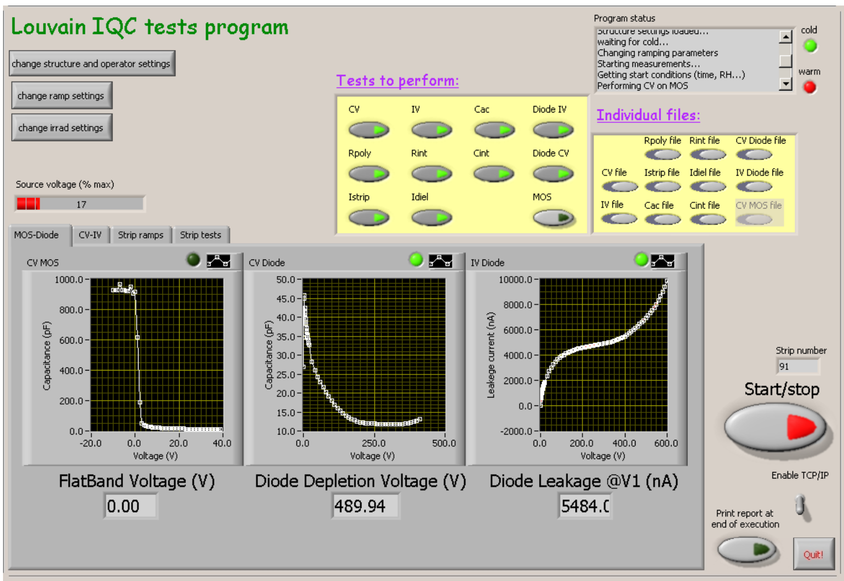

Fig. 33 : Screenshot of the probe station acquisition program.

Behind its main control panel (Fig. 33), this program is arranged in many different layers according to the level of the actions performed. The most basic commands are directly related to the instruments, and these commands are arranged in measurement routines, which are in turn used to perform the whole measurement of a parameter, including a curve fit in certain cases and the writing of the results in a dedicated file. These measurements are in turn arranged altogether to perform an entire test of all the common bulk and strip parameters.

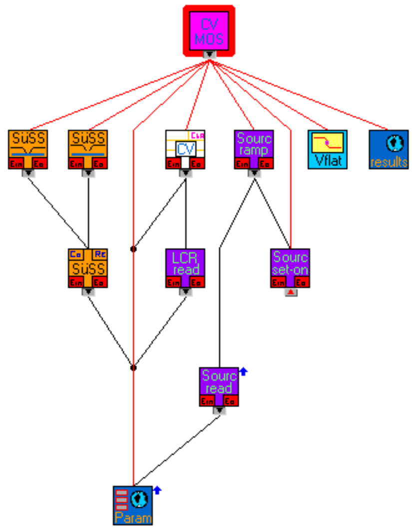

Fig. 34 : LabVIEW® program hierarchy in the case of a CV on MOS device.

Fig. 34 illustrates this organisation in the case of a CV measurement on MOS device in order to determine the flat band voltage. One can distinguish the probe station commands on the left, the measurement itself with the bulk capacitance measurement routine and the sourcemeter control, the calculus of the flat band voltage on the right, and finally the global variable used to store the results.

In the framework of the CMS IQC testing, the program is also used to load the measurements made before irradiation as well as the irradiation parameters (fluence, date, etc.) and format the results in a XML file whose format is suitable to be put in the CMS construction database.

3.1.2. Performances, measurement accuracy

The electrical characterisation setup is supposed to accurately measure very low currents. Indeed, the leakage current of a baby detector on a CMS test structure at –10 °C is of the order of a nanoampere and we also have to determine the value of resistances higher than 20 GΩ. Dealing with such low currents requires a good wire shielding and the avoidance of any ground loop in the circuitry.

As there is in fact no magical recipe to ensure a perfect insulation without any ground loop, we used some well-known ingredients such as shielded coaxial cables (to cope with the high voltage applied on the structures, these are able to sustain voltages up to 1000 V) and metallic boxes when lab-made circuits were to be built. The apparatus connections are as few as possible, to avoid loop generation, although ensuring each instrument is connected to the shielding lines in this way. Some of the sources and measurement devices have separate "common" and "chassis" connections to be used either to define the zero level between the instruments or to shield the setup, in the case of our electrometer, it has been found that one should disconnect the coupling of these connections to avoid perturbation of the current measurements.

On the switch matrix level, we realized also that the connection of all cable shields together is not a good method. Avoiding current parasites requires additional individual connections of the shields of the two cables connected through the matrix. We do not know exactly the reason of this as all of these were already connected together in the first scheme. This has however easily been achieved as each switch of the matrix is in fact doubled for this purpose.

Once these connections made, the accuracy and reliability of the current measurements were improved. The current measured on non-shorted silicon sensor dielectrics at 10 V are less than 1 pA. This could lead to interstrip resistance measurements up to 100 GΩ that would suffice for CMS testing (the acceptance criteria being 20 GΩ), but to ensure a higher precision and avoid perturbation due to higher post-irradiation leakage currents, the measurement is performed doing a small current-voltage ramp whose slope will give the resistance.

Beside the current measurements, the parasitic capacitance was also reduced to about 10 pF (12 pF in the case of the CV measurement because of the decoupling box). The LCR has a specific calibration routine to deal with additional stray capacitance, requiring the measurement of these capacitances in open and shorted contact configurations. Unfortunately, this very practical feature is useless in our case, as the switching matrix changes the stray capacitances for each type of measurement. However, we found that the stray capacitances values for our setup values are acceptable and can directly be subtracted from the measurement in order to obtain the relevant sensor value. This latter subtraction needs frequent calibrations of the system because the parasitics changes a bit during the maintenance of the system (e.g. needle changes).

Another effect of the setup on the measurements is due to the vacuum-induced strain on the structure. Indeed, this constraint can affect the leakage current* of a detector due to lattice deformations. This effect has been observed with many test setups and has been proven to be sensitive to the vacuum strength. This has been an issue for some centres among the sensor group as the problem could even lead to the rejection of sensor batches. These showed a high leakage current about 20 µA, but only when stressed by the vacuum applied on the sensor to maintain it on the chuck (Fig. 35).

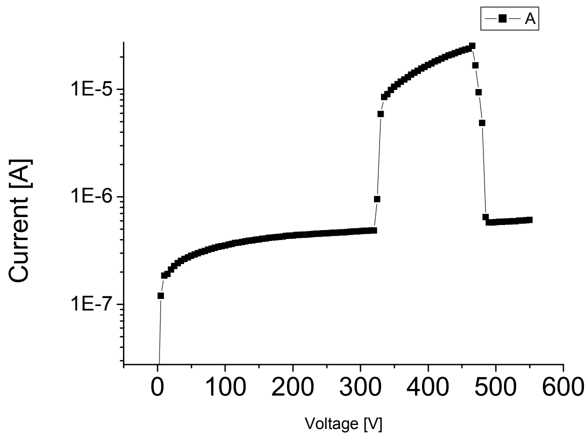

Fig. 35 : influence of chuck-vacuum in the Karlsruhe setup (the step in current appears when vacuum is applied on the sensor). This effect is observed despite the high planarity of the chuck plate. Taken from [47].

In our case, as already mentioned above, we use a dedicated chrome-plated plate on the chuck. It has been rectified to be as flat as possible and its vacuum grooves are only a millimetre wide. Fig. 36 shows clearly that vacuum has no effect on the measurement of the total leakage current of a sensor. The difference of vacuum behaviour is probably due to the vacuum strength and grooves design.

* The electrical resistivity of a semiconductor changes with strain, this is the principle of strain gauges, and hence on a reverse-biased sensor, a higher leakage current can be observed under strain. This is due to changes in electron and hole mobility with changes in crystal structure as strain is applied.

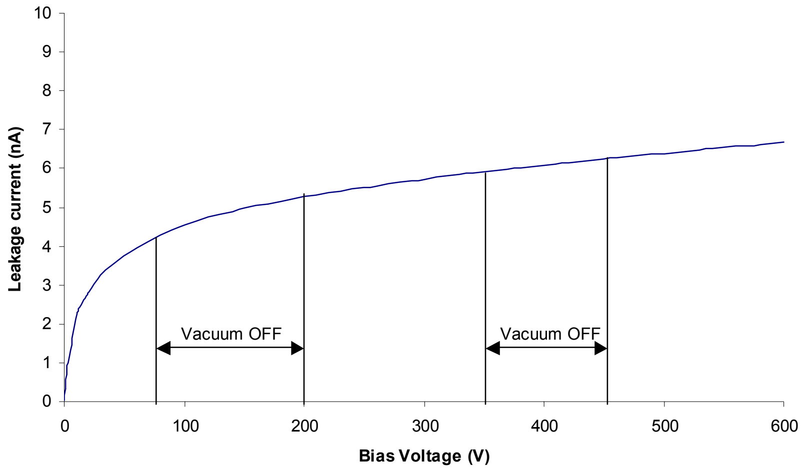

Fig. 36 : Effect of vacuum on Leakage current (measurement performed at 20 °C on non-irradiated 500 µm thick sensor). There is clearly no vacuum-induced effect.

3.1.3. Encountered Problems

Once the corrections for parasitic capacitances were implemented in the program, the most problematic issue encountered was the pinhole generation after irradiation.

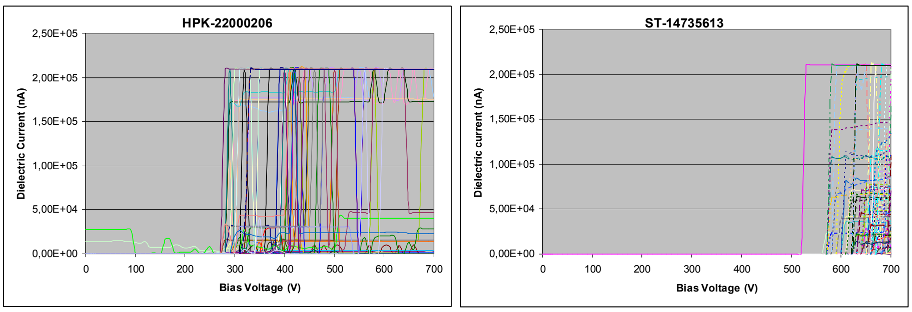

Fig. 37a, b : Dielectric breakdown observed on thin (HPK) and thick (ST) structures after irradiation. Both type of structures where submitted to the same test conditions, but Hamamatsu (HPK) devices are more affected due to lower dielectric breakdown voltage.

Most tested strips showed a breakdown in the dielectric current as a function of the bias voltage (cf. figures above). The Hamamatsu structures were most affected, as their oxide resistance to breakdown was lower than ST-manufactured ones. The switching scheme and test ordering was quickly suspected as the problem arose after the full integration of the tests within a single program sequence.

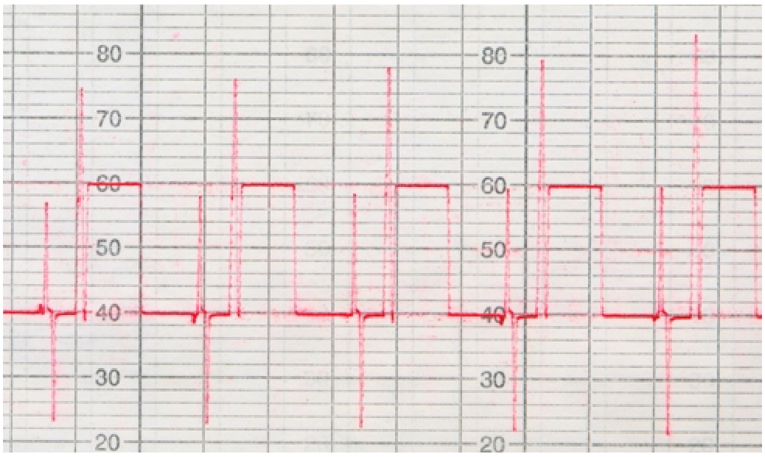

Fig. 38 : Voltage applied on the strip dielectric during 5 strip test sequences (before switching revision). The transient variations at each step were the cause of pinhole creation.

A direct measurement of the voltage applied to the strip dielectric during a strip test sequence rapidly pointed out the existence of parasitic high amplitude voltage peaks applied between DC and AC pads. These peaks (even bigger than shown on Fig. 38 due to the pen-tracer speed) have increasing amplitude with the bias voltage and were the cause of the observed breakdowns.

The solution was first to change the order of the strip parameter tests, minimising the number of switching needed and second, either to ramp the sensor down to 0 V between the strip to strip movements or to keep its bias ring connected at all times during the tests. It is evident that the latter option has been implemented to speed up tests.

Fig. 39 shows the impact of these changes on the voltage applied on the dielectric: the peaks have been removed and the pinholes have indeed stopped to appear in the post-irradiation measurements.

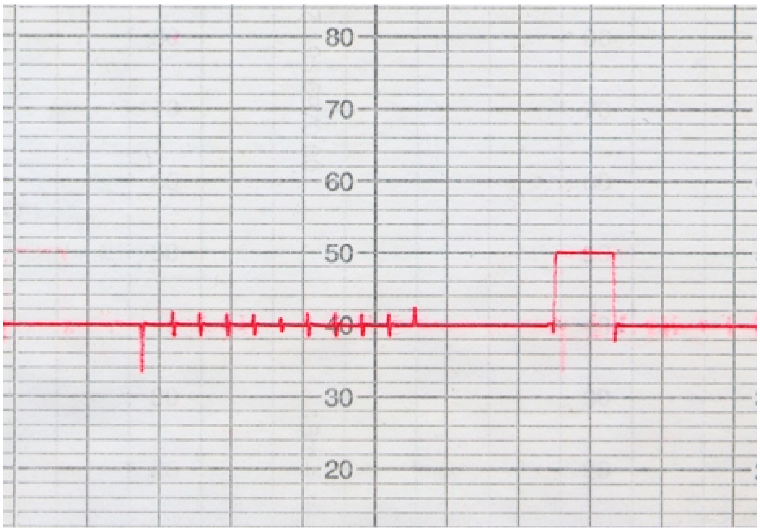

Fig. 39 : Voltage applied on one strip test sequence (after switching revision). Transient peaks have been removed, and setup-induced pinhole creation stopped.

The second problem, still arising sometimes, is bound to our CV-decoupling box. The circuitry of this filter is pictured, without the additional relays, on Fig. 40. The resistors (R_1 and R_2) going from the HV source to the backplane contact of the sensor have to undergo the whole sensor current. Under severe current breakdowns, these resistors may burn as their maximum power lies around 0.6 W. Since these resistors have values of 38 kΩ and 62 kΩ, this sets a limit on the sensor current at 3 mA, which is large enough for all devices irradiated (typical currents for test structures being 60 μA). We could have added diodes or changed the resistors for more power-tolerant ones but we did not as the burning of the resistor indicates that we are approaching the capabilities of our Keithley sourcemeter, limited to 10 mA. This was good as it prevents us from applying lower-than-expected biasing voltages to the detector under test.

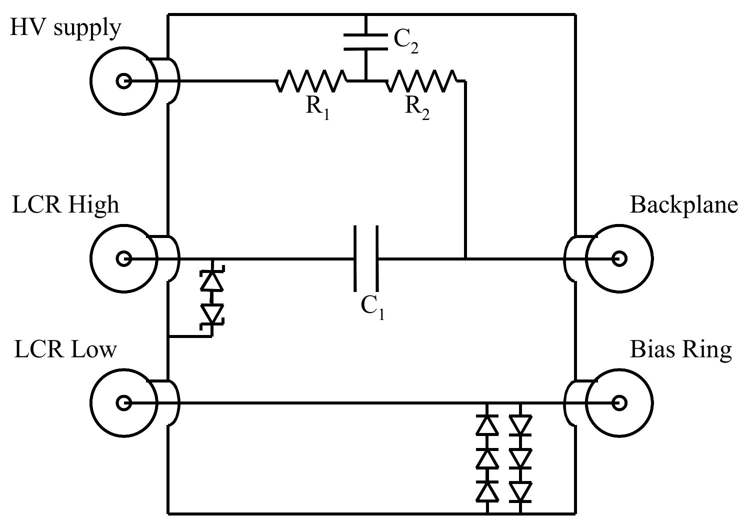

Fig. 40 : CV decoupling filter principle.

3.1.4. Cross calibration with the Karlsruhe system

Whereas the depletion voltage determination as well as the leakage current measurements did always show a good agreement between measurements made in Louvain and by our colleagues in Karlsruhe or even in institutes involved in the CMS sensor group, the strip parameters measurements did require further checks and setup modifications.

First, if the coupling capacitance measurement calibration has been performed easily because of their relatively high values (around 60 pF for a baby detector, more than 500 pF for most full size detectors) compared to the capacitance parasitic, the story was a bit different considering the interstrip capacitances. For a baby detector, these capacitances are of the order of 1 pF before irradiation. The comparison of our results (Fig. 41, below) showed a fairly similar behaviour of the interstrip capacitance-bias voltage curve with respect to the observed decrease and bumps, but with different values. One between the two setups could therefore be improved.

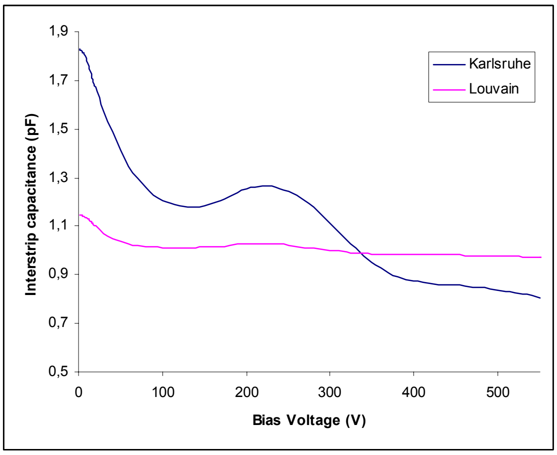

Fig. 41 : Interstrip capacitance measurements performed at Karlsruhe & Louvain, after irradiation on the same p-irradiated structures.

On the Louvain setup, we realised that the interstrip capacitance measurement was perturbed by the needle in contact on the AC pad. Indeed, measuring the small interstrip capacitance requires the LCR to work at high frequency (1 MHz in this case). At that frequency, the coupling capacitance is shorted (in red on Fig. 42, it is 2 orders of magnitude higher than the interstrip one, and has hence a very low impedance at 1 MHz) and the AC pad needle is hence connected to the measuring needles, perturbing the measurement.

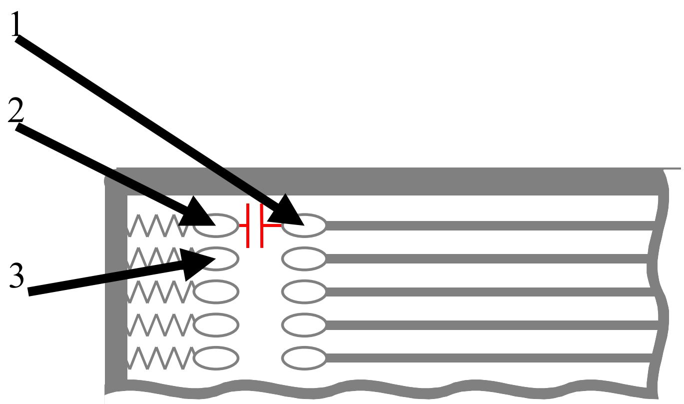

Fig. 42 : Interstrip capacitance measurement perturbation.

The problem has been solved by also connecting Fig. 42's needle 1 together with needle 2 at the level of the switch matrix, hence not only using needles 2 and 3 during the measurement, but also the last other needle in contact with the pads.

The new measurement scheme gave values between 0.66 and 0.68 pF for baby detectors, 2.33-2.35 for OB2 sensors (all measurements performed at full bias, before irradiation). The ratio between these measurements is 3.5. Using the usual capacitance approximation formula (3.3), the interstrip capacitances should be proportional to the strip lengths and inversely proportional to the strip pitches. This leads to a ratio R of 3.9, slightly different from the observed one, but this approximation does not take the capacitance border effect into account and these have an impact on the strip capacitances.

$$C = \frac{2\varepsilon_0 S}{d} \tag{3.1}$$

$$R = \frac{L_{strip,full}\, pitch_{baby}}{pitch_{full}\, L_{strip,baby}} \tag{3.2}$$

On the other hand, the Louvain setup gives now the same interstrip capacitance values than the Karlsruhe setup.

Another measurement that appeared to be tricky in the beginning was the determination of interstrip resistances. Indeed, the measurement of resistors as high as several GΩ implies the accurate measurement of very low currents. As mentioned above, the currents measured with our setup on non-shorted silicon sensor dielectrics at 10 V are less than 1 pA, but due to the high sensitivity of the measurement to any perturbation, the connections evolved a bit to cope with the high leakage current of the detector after irradiation. Fig. 43 shows interstrip resistance measurements as a function of the bias voltage. These measurements are both made in Louvain and Karlsruhe on a standard test structure. The continuous red lines show the min. and max. measurements made in Karlsruhe (on the same structure but at a different annealing stage). This figure clearly shows that both setups give similar results.

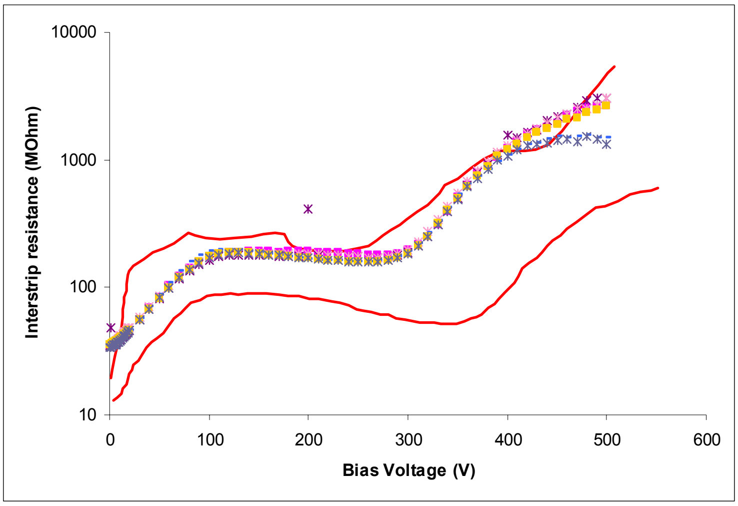

Fig. 43 : Post-irradiation interstrip resistance measurements made in Louvain and Karlsruhe (on the same structure but at a different annealing stage).

At this stage, both CMS-IQC setups within the sensor group were giving consistent results.

3.2. The T2 beam line and instruments around the irradiation zone

This section consists of a detailed overview of the neutron beam line and the experimental setups around the irradiation zone. The first part of this section is largely inspired from ref. [48]. This latter being largely devoted to the neutron beam, it will only briefly be introduced here. Some of the details of its monitoring are also further developed in the annexes.

According to the irradiation protocol, the environment in the irradiation zone has to be as close as possible to the CMS tracker environment, described in sections 1.2.2.

In that sense, and first of all, one cannot neglect the low temperature requirement, mandatory not only to match the Tracker atmosphere, but also to avoid uncontrolled annealing effects during irradiation. This temperature requirement comes with a stringent condition on the relative humidity inside the irradiation cold box to ensure there will be no condensation on the sensors.

Second, sensors should better be biased during irradiation. This is a very demanding requirement because of the high irradiation rate and charged particle levels in beam or reactor radiation fields. It also explains why there is no extensive study of the influence of biasing during irradiation on the radiation damage parameters of silicon sensors. On this aspect, a great asset of our neutron beam, compared to proton beams or other radiation sources, is that its low gamma and charged particle contamination permits the biasing up to voltages as high as 650 V and even more in the case of CMS structures, keeping the device fully depleted during the entire test*. The influence of biasing during irradiation is discussed in section 2.3.5 and further developed in 4.2.1.

Finally, the PC-based control of the power supplies is also used as an input to an acquisition program logging all the irradiation parameters during and also after the irradiation period.

3.2.1. The High flux neutron beam line

The high flux neutron beam, especially designed for LHC radiation hardness tests, uses a primary 50 MeV deuteron beam to produce neutrons from the $^{9}Be(d,n)^{10}B$ reaction. It has been shown that this reaction has the highest neutron production cross section at 50 MeV compared to other reactions like $^{7}Li(p,n)^{7}Be$. As the deuteron beam optics may slightly vary along the different tests, a Titanium collimator (pictured in Fig. 44) is used to define the beam spot on the ^{9}Be target and hence keep the neutron beam geometry constant. The production target is made of a Beryllium cylinder with a thickness of 2 cm and a radius of 4 cm. It is encased in a water-cooled copper ring that is electrically insulated from the rest of the beam line. In this way, the deuteron current can directly be read on the target for monitoring purposes.

To keep the charged particles and gamma contaminations as low as possible, a special filter is placed right after the production target. It is made of a 1cm thick polyethylene slab stacked together with 1mm of Cadmium and 1mm lead. The aim of this filter is not only to remove most of the charged particle contamination, but also to absorb part of the gamma produced and to harden the neutron spectrum by removing its low energy part.

* Without any annealing, the depletion voltages of typical CMS structures can rise up to 600 V when reaching the nominal LHC fluence.

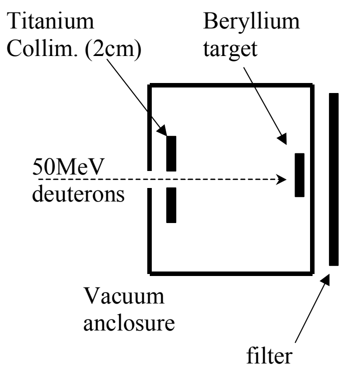

Fig. 44 : Neutron production in the T2 beam line.

An extensive study of the beam properties has been carried out in the past (cf. [48] and [49]), using several dosimetry techniques to determine the beam spatial extension as well as its energy spectrum and other particle contaminations. The most important features are outlined below.

First, the neutron energy spectrum, determined using several different activation foils (cf. A.1.2 for a description of the method) is shown in Fig. 45. In the context of the CMS sensors tests, we compute a hardness factor to convert the real fluence into 1-MeV equivalent fluence according to equations (2.9) to (2.11) and using factors taken from references [41] and [42]. In this case, the obtained hardness factor is 1.95.

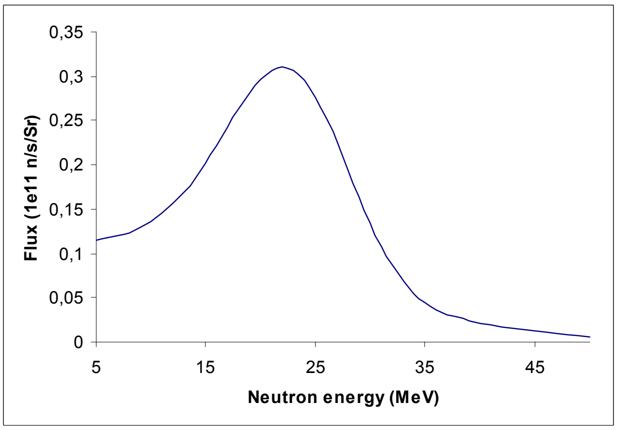

Fig. 45 : The fast neutron beam line energy spectrum. Taken from [49].

Then, the neutron yield and dose rate have been measured using three methods: a calibrated ionization chamber mounted together with a polystyrene phantom, RPL dosimeters and alanine dosimeters. The integrated neutron yield is 6.6 10^{11} neutrons/µC/Sr. For 10 µA of deuteron current on the target and at a distance of 9 cm from this latter, this yield corresponds to a neutron flux about 7.3 10^{10} n/cm^{2}s at the centre of the beam. Fig. 46 gives the radial extension of the beam as a function of the distance from the target, a useful function to determine the position of the samples to be irradiated.

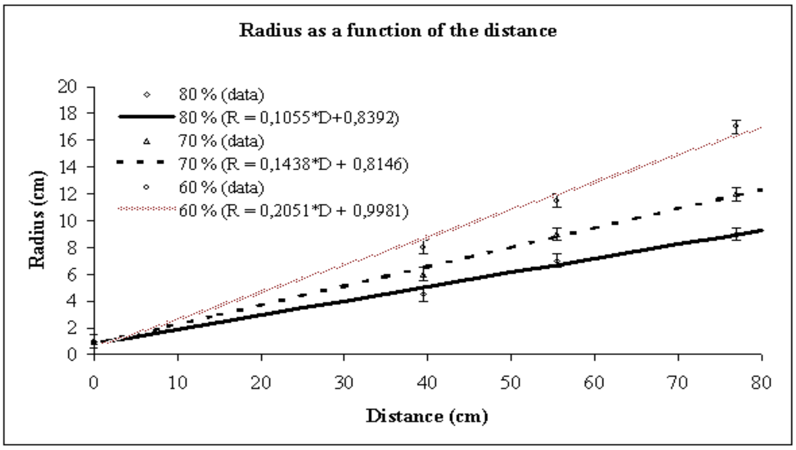

Fig. 46 : Radial extension at 80, 70 and 60 % maximum of the T2 neutron beam line, taken from [49].

Finally, the beam contaminations have been assessed using Monte-Carlo simulations because these are rather difficult to measure. The results of these simulations are shown in Table 7.

Particle type	Fraction (% of neutron yield)	Average energy (MeV)	Maximum energy (MeV)
Proton	0.015	12.61	25
Electron	0.016	1.57	6
Gamma	2.4	1.93	10

Table 7 : The high flux neutron beam contaminations.

3.2.2. Sensor environment, cold box

As mentioned at the beginning of this section, irradiations of silicon sensors have to be performed in a dry and cold environment. To fulfil this requirement, we equipped the neutron beam line with a temperature regulation system that also ensures a low relative humidity within the cold box.

Depicted in Fig. 47, the cooling principle is pretty simple: a proportional gauge, controlled by a PID regulator*, is used to regulate airflow. This latter is further dried using silica gel bottles and thereafter cooled by liquid nitrogen. The mixing of dry air and evaporated nitrogen ensures a very low relative humidity. Once cooled, the air flows to the irradiation box through insulated pipes. The temperature inside the cold box is measured using a Pt100 sensor that is directly read by the PID regulator. The regulation can be switched off or bypassed using the manual gauge mounted in parallel to the proportional one.

Several different cold boxes have been used as the irradiation setup was improved. All of these were made of 6 cm thick insulating walls, with opaque-Mylar windows on the beam entrance.

A calibration and performance test has been performed with the first cold box (inner volume of 18 l). Temperature has been monitored using an additional Pt100. Fig. 48 shows the temperature evolution, starting with the automatic calibration setup procedure. From this measurement, it can be seen that the calibration of the cold box takes about 30 minutes, but this result is highly dependant on the volume of the cold box and on the initial temperature of the cooling system. A more interesting result is the temperature stability, assessed by the maximum deviation in a stable temperature plateau, which is less than 0.5 °C and hence well suited for our purposes. Fans placed inside ensure the temperature uniformity within the box.

* PID stands for Proportional-Integral-Derivative: the command signal of the regulating unit depends not only on the gap between the parameter setup and the measured value, but also to its time dependence. An introduction to PID regulation and the automatic setup procedure of the yokogawa unit can be found in [28] and [50].

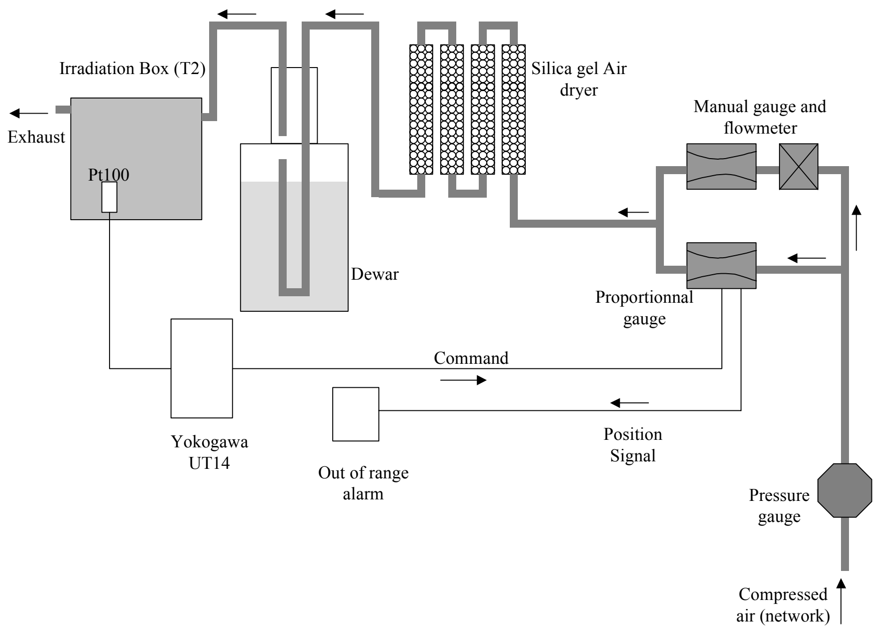

Fig. 47 : Principle of operation of the irradiation cooling system.

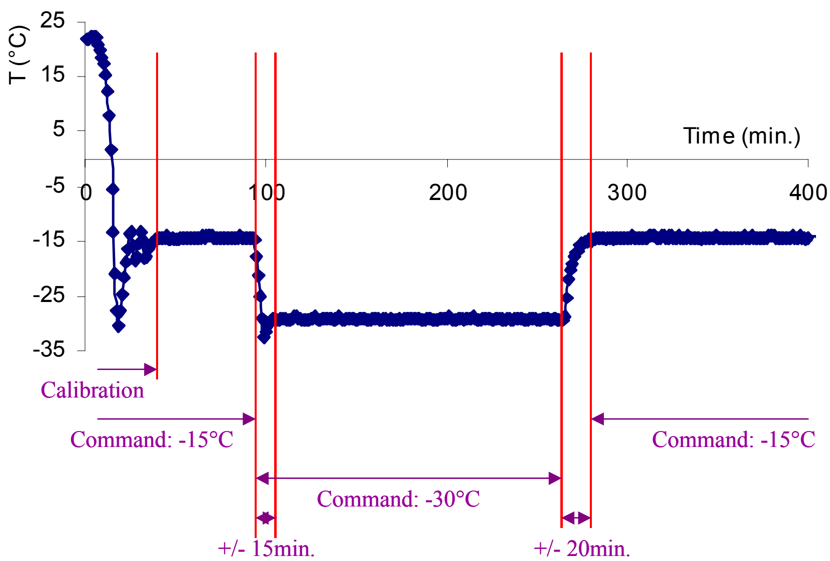

Fig. 48 : Time evolution of the temperature inside the irradiation cold box during calibration setup and afterwards.

Beside the temperature criteria, the relative humidity inside the irradiation box is another important feature of the system. Indeed, the box is unusable if the dew point is so high that condensation occurs on the sensors. First measurements of the relative humidity were a bit disappointing: the remaining relative humidity was about 30 % at -10 °C, with a corresponding dew point of –16 °C that is way too close to the irradiation temperature of –10 °C. A new cold box solved the problem: a better air tightness reduced exchanges with the ambient air and lowered the relative humidity down to 4 % at –10 °C (dew point = -40 °C).

A major drawback of this system is the maintenance of the silica gel air dryer, to be performed once or twice a year depending on the use.

Fig. 49 shows a picture of the irradiation setup equipped with the latest cold box on its sliding rail. This latter allows the irradiation of 3 different stacks of sensors (cf. next paragraph) without opening the irradiation zone. This saves time and optimises the use of the allowed beam time as the radiation level inside the irradiation zone quickly increases after the beginning of the irradiation and as several hours of cool down are necessary to penetrate it again. The movement of the box is made using cables running out of the irradiation zone. Also shown on the picture, the high voltage electrical connections used to bias the sensors.

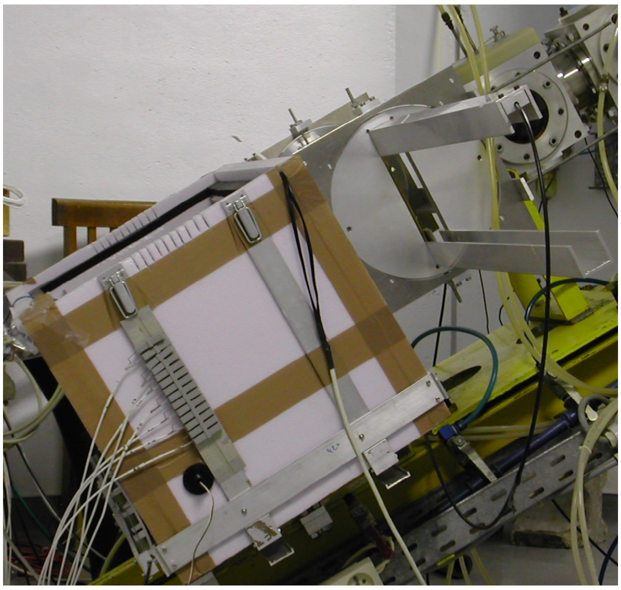

Fig. 49 : Fast neutron beam line irradiation box on it’s sliding rail. One can distinguish the HV connections for sensor biasing on the side.

3.2.3. Sensor biasing

Having addressed the issues about the irradiation environment, we are coming now to the sensors themselves. There's no need to say that these will be biased during their operation in the CMS tracker and hence, the opportunity to bias the sensors during irradiation is an asset when considering radiation hardness tests, even if there is no study yet on the impact of High voltage on the sensor's radiation hardness. This opportunity has already been discussed from the neutron beam radiation environment point of view and the considerations on power supplies and connectivity of the sensors are addressed in this paragraph.

First, an estimation of the current drawn by the silicon sensors during irradiation can be obtained with the alpha parameter before annealing, known from literature (e.g. [32]), the volume of the device under test (if fully biased) and the 1-MeV equivalent fluence attained during irradiation. As discussed in section 2.3.3, this estimation is calculated using equation (3.3).

$$I_{leakage} = V_{device}\alpha_0\Phi_{1-MeVequivalent} \qquad (3.3)$$

For CMS test structures and sensors, the leakage currents computed in this way are listed in Table 8 and Table 9 for fluences of 10 and 15 years of LHC operation, and at room temperature.

The average leakage current to be expected on full size sensors is 42 mA (69 mA maximum) at 15 years LHC fluence. For test structures, the average value is 0.19 mA (0.25 mA maximum). As mentioned above, the values are quoted for sensors at room temperature and as irradiations are performed at –10 °C, the currents drawn by the devices will be about 16 times lower (5 mA max.).

Sensor type	Leakage current at 1.6 10^{14} n/cm^2 (mA)	Leakage current at 2.4 10^{14} n/cm^2 (mA)
IB	34,7	52
W 1 tec	30,6	45.9
W 1 tid	40,9	61.4
W 2	46.6	69.9
W 3	38.4	57.6
W 4	35.8	53.8
Test structure	0.16	0.24

Table 8 : Leakage currents foreseen for 320 µm CMS structures and sensors.

Sensor type	Leakage current at 0.5 10^{14} n/cm^2 (mA)	Leakage current at 0.8 10^{14} n/cm^2 (mA)
OB	20.4	32.7
W 5a	19.9	31.9
W 5b	17.4	27.9
W 6a	20.4	32.7
W 6b	20.2	32.3
W 7a	19.3	31
W 7b	17.7	28.3
Test structure	0.08	0.13

Table 9 : Leakage currents foreseen for 500 µm CMS structures and sensors.

Now that the foreseen leakage current is known, the depletion voltage at end of the irradiation has to be computed. It can be done using the Hamburg model discussed in 2.3.3. This latter has to be given the initial effective doping concentration, extracted from CV measurement (using (3.4) that takes the effect of the segmented geometry into account, cf. [26]), and the 1-MeV equivalent fluence reached. The other parameters of the model such as donor removal constants will be taken from literature. In this case, we do not have to discuss about any reverse annealing as the irradiation is performed at low temperature. This leads to a simplified formula shown in (3.5), where only the donor removal, stable damage and beneficial annealing (at t=0) terms are taken into account.

$$\left|N_{eff}\right| = \frac{2\varepsilon\varepsilon_0}{qd^2}\left(\frac{V_{dep}}{F_{geom}} + V_{bi}\right) \qquad (3.4)$$

$$\left|N_{eff,after}\right| = \left|N_{eff,before} - r_c N_{eff,before}\left(1 - e^{-c\Phi_{1-MeV}}\right) - \Phi_{eq}\left(g_c + g_a\right)\right| \qquad (3.5)$$

The results shown below in Table 10 and Table 11 were obtained for an initial depletion voltage of 160 V and using a donor removal constant r_c of 0.8, which has proven to be a bit over-estimated in the case of our neutron beam (cf. 4.2).

Sensor type	Depletion voltage at 1.6 10^{14} n/cm^2 (V)	Depletion voltage at 2.4 10^{14} n/cm^2 (V)
IB 1	474	716
IB 2	521	781
W 1 tec	492	740
W 1 tid	492	740
W 2	527	789
W 3	545	814
W 4	526	788
Test structure	521	781

Table 10 : Depletion voltages foreseen for CMS test structures and sensors from the inner tracker (320 µm thick sensors).

Sensor type	Depletion voltage at 0.5 10^{14} n/cm^2 (V)	Depletion voltage at 0.8 10^{14} n/cm^2 (V)
OB 1	126	223
OB 2	145	249
W 5a	130	229
W 5b	134	235
W 6a	142	245
W 6b	132	231
W 7b	134	234
W 7a	139	241
Test structure	125	223

Table 11 : Depletion voltages foreseen for CMS test structures and sensors from the outer tracker (500 µm thick sensors).

According to these estimations, the average depletion voltage to be expected on full size sensors is 484 V (814 V maximum) at 15 years LHC fluence. For test structures, the average value is 502 V (781 V maximum).

Once combined with the leakage current results, the requirements on the power supply for the full size sensors are 1000 V with a current of 5 mA at least (80 mA if we want to be able to bias the sensors at room temperature and keep the system versatile). The biasing of baby detectors puts less stringent requirements (800 V at less than 1 mA), but on more channels as most of the radiation hardness study will be done using these test structures.

To match these requirements, we equipped the irradiation area with two Iseg High current power supplies (one channel each with 60 mA at 1 kV) and two CAEN N470 modules providing eight lower current channels (up to 3 kV at 1 mA). The Iseg power supplies are powerful enough to keep all sensors but W1tid and W2 (the most demanding sensors) biased at room temperature.

Many different options were considered to apply the biasing voltage to the sensors and test structures. Among these, only the use of bonding has proven to be satisfactory, as the other techniques (e.g. the use of needles) did not provide reliable electrical connection of the device to the high voltage cable. A sketch of the irradiation support plate dedicated to test structures is shown in Fig. 50. The electrical connection of the baby sensor is made on its side using two aluminium plates that are in turn connected to the high voltage cables. The design of the sensor plates is fairly similar. Another advantage of bonding compared to other solutions is the smaller spacing between the different plates of the irradiation stack. This leads us to considerations about the irradiation uniformity across a stack of supports. The sensors spacing is about 1.1 cm. This is less than the spacing obtained with any of the other solutions envisaged (e.g. conductive rubber). Using the beam specifications described above and at the usual distance from the target for CMS sensor irradiations, the spread around the mean fluence of a stack comprising 6 detector layers is ± 6 % (the biggest and lowest fluences at extreme positions of the stack are different to the middle one by 6 %).

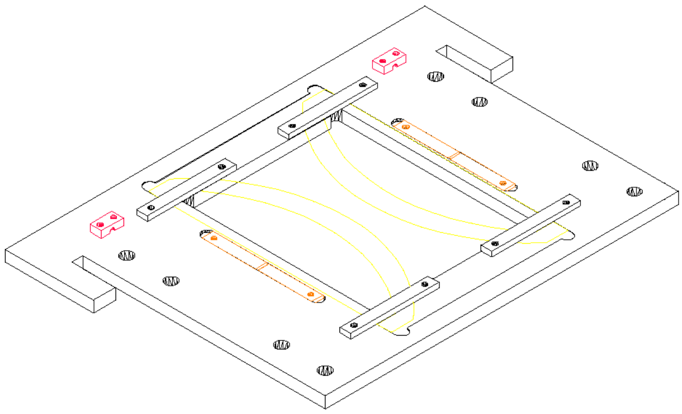

Fig. 50 : Irradiation support for the test structures. One can distinguish the aluminium strips on the side for bonding and electrical connection of the bias line and backplane of the sensor.

3.2.4. Acquisition and monitoring

The monitoring during irradiation is twofold: monitor the sensor bias but also the environment and the beam current. These tasks are ensured by a TestPoint® program reading a multichannel acquisition card and a Caenet interface card, also used to control the N470 HV power supplies.

On one hand, the CaeNET® controller reads the voltages and currents applied on the test structures and, on the other hand the acquisition card reads the analogue outputs of the Iseg power supplies (voltage and current) as well as those of a controller (used to read the temperature with a Pt100 sensor) and a current digitizer used to monitor the deuteron beam current (cf. A.1.1).

This program gives an online estimation of the integrated beam current, plots the irradiation parameters and stores these latter in a log file for further access. A screenshot of its user interface is shown below.

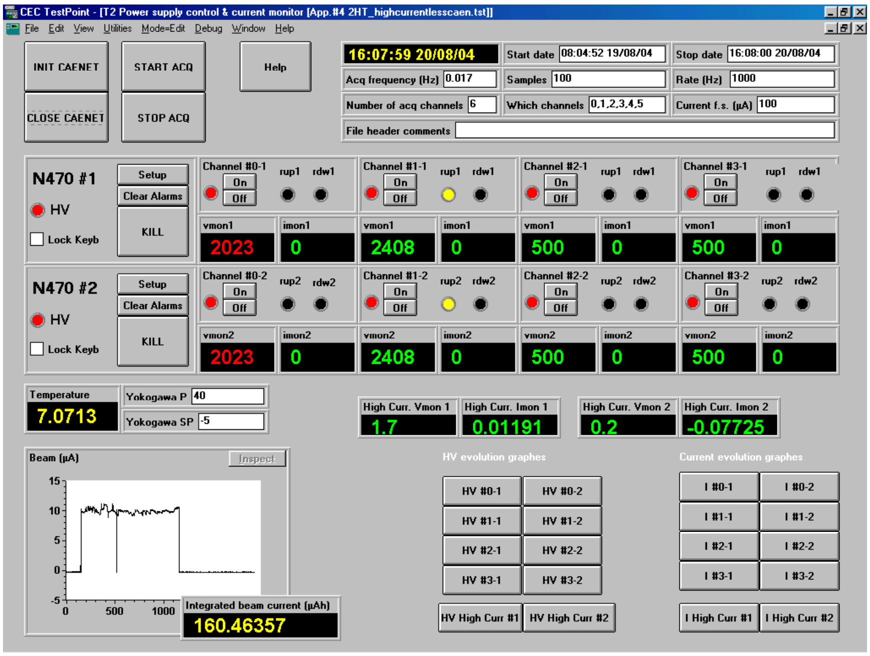

Fig. 51 : Screenshot of the irradiation monitoring program.

3.3. Sensor test protocol in Louvain

The tests performed during the last four years in Louvain are part of the overall CMS tracker sensor QA scheme, discussed in paragraph 2.5 and published in Ref. [45]. As an Irradiation Qualification Centre (IQC), Louvain regularly receives sensors and test structures from the QTC (qualification test center). At the production level, these sensors are labelled according to their type, manufacturer and production date but are also dispatched in "sets" by the QTC. Here is what happens to these sets when these arrive in Louvain (cf. Fig. 52).

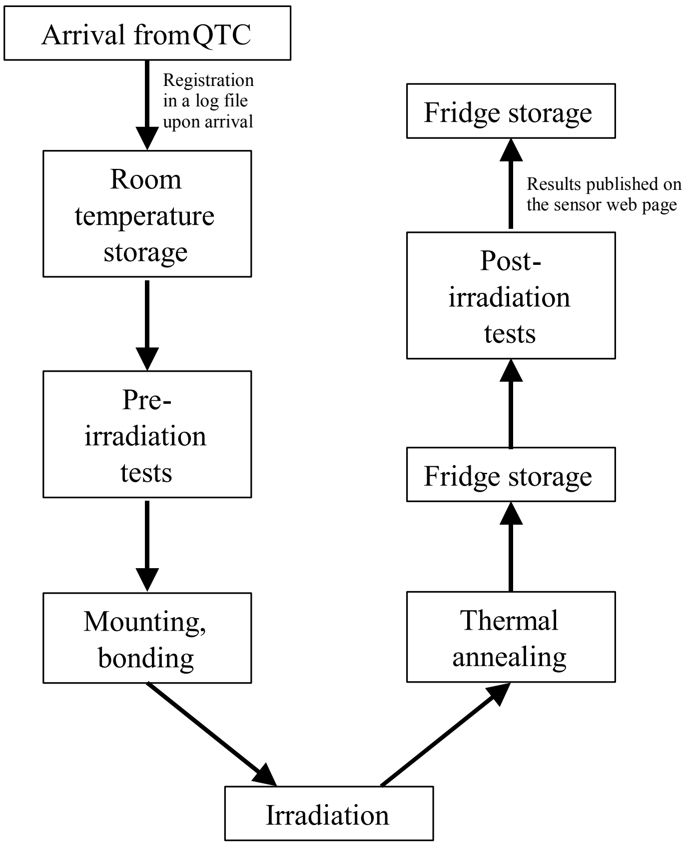

Fig. 52 : The sensor test protocol in Louvain-la-Neuve.

The pre-irradiation tests involve the usual CV, IV and strip parameter measurements, the latter being measured on one strip as a function of the biasing voltage and on several strips at a reference voltage of 400 V. A CV test on MOS device (in the case of test structures only, as sensor do not have MOS devices) has been added to the measurements on the baby detector. This has been decided because of high flat band voltages observed on ST structures in 2002*. The poor quality of the oxide (trapped charges) has some

* There were, in that time, several batches of ST sensors presenting a poor quality of the surface oxide, reflected by a high flatband voltage measured on MOS devices.

impact on the proton radiation tolerance of the devices, although no effect has been observed about the neutron radiation hardness. Before the irradiation, as well as after, all the tests are done at –10 °C.

After irradiation, the devices should be kept cold to avoid any uncontrolled thermal annealing. On the other side, avoiding condensation on the detectors requires them to be at room temperature during the manipulations. These operations should therefore be performed as quickly as possible.

The thermal annealing is performed with our lab-made oven (cf. A.2) for 80 minutes at 60 °C. According to previous studies on the evolution of the leakage current, this is equivalent to 14 days at room temperature. As this annealing procedure is a standard practice in the silicon community, we are able to compare the results obtained with CMS devices to other ones. A little stay of at least 8 h in the fridge after annealing is required to avoid the perturbation of the measurement by temperature-activated bistable defects [43].

When the detectors are ready to be tested again with the probe station, the same tests than before irradiation are performed (excepted the MOS test which does not give any good result because of the high density of trapped charges in the oxide). The program itself then makes a comparison of the strip parameters before/after irradiation and we check the evolution of the bulk parameters against the predictions of the Hamburg model (depletion voltage) and empirical results on the leakage current. For the ease of use in the community, a summary is published on the group webpage for each PQC set.

Afterwards, the sensors are kept in the fridge in case we need to perform further tests.

3.4. Summary

Before the start of this work, it was barely possible to perform the irradiation of silicon sensors in Louvain-la-Neuve. Indeed, the neutron beam was the only element available. We therefore started to equip the irradiation zone with cooling, biasing and monitoring device. The laboratory is now in possession of every adequate device useful to perform an irradiation in a controlled environment with respect to sensor bias, temperature and relative humidity. In the annexes, the required associated dosimetry methods are described as well as their calibration in this specific context.

The most complex system developed was the electrical characterization setup. The measurement of very low currents and determination of high resistances, the accurate assessment of small capacitances and the handling of high voltage requires the use of selected materials and components. The setup has been build step by step, integrating the different measurements together in a program able to perform a complete characterization in an automated way, including the temperature control of the chuck and the automation of the movements enabling to scan the sensor over its surface.

This setup required some iterations and debugging in order to gain confidence in the obtained results. Measurements on test devices and cross-comparison with other laboratories gave us that confidence.

Finally, a standard procedure for structure and sensor handling in Louvain-la-Neuve has been developed, so that all irradiations are performed in the same conditions.

Chapter 4 : Evolution under irradiation

This chapter is dedicated to the presentation of the results obtained in Louvain-la-Neuve.

The first section deals with irradiations with the quasi-monoenergetic neutron beam in the Q-beam line. This test was aimed to validate the NIEL scaling for neutron energies above 20 MeV.

The second section then presents a summary of the results obtained on CMS test structures: the impact of bias during irradiation is discussed before going into more details about the evolution of the different electrical properties of the sensors.

In this chapter, it is difficult to make assumptions on the shape of the result distributions (is it gaussian or is there another law behind the processes). Every number quoted as standard deviations are to be understood as RMS values of the sample distribution. When required, the propagation of these numbers has been done using the usual variance error propagation formula. The impact of systematic errors is believed to be small compared to these RMS values, according to the results of the inter-calibrations depicted in Chapter 3.

4.1. Experimental neutron hardness factors

As pointed out in 2.3.2, the NIEL hypothesis and the hardness factors, used to scale the fluences of many different particles to a global 1-MeV neutron equivalent fluence, has proven to be useful to describe the depletion voltage and leakage current evolution of silicon devices in a radiative environment. However, these factors have only little experimental confirmation. Regarding neutrons, for instance, there are only 3 experimental measurements at energies below 20 MeV [52].

As the CMS environment will involve neutron energies exceeding 20 MeV, and because the intense fast neutron beam line in Louvain-la-Neuve reaches neutron energies above 20 MeV, it makes sense at this point to perform an experimental determination of the hardness factors above 20 MeV.

For this purpose, a monoenergetic source is obviously always better since the unfolding of the data is easier. By chance, the cyclotron facility in Louvain-la-Neuve has such a neutron beam (refer e.g. to [53]).

This paragraph depicts the experimental determination of NIEL hardness factors at 3 energies above 20 MeV, beginning with a description of the irradiated devices and the beam line.

4.1.1. Diodes description, pre-irradiation qualification

We irradiated several diodes, either oxygenated or not. These were samples received either from CERN (M. Moll) or from the university of Hamburg (G. Lindström).

The devices are all 5X5 mm^2 square pad diodes made on approx. either 280 µm or 300 µm thick silicon wafers (pictured in Fig. 53). Their design is very similar excepted that the Hamburg ones have several guard ring structures, instead of one only for the CERN devices, ensuring a stable high voltage operation and a nice shape of the electric field within the bulk.

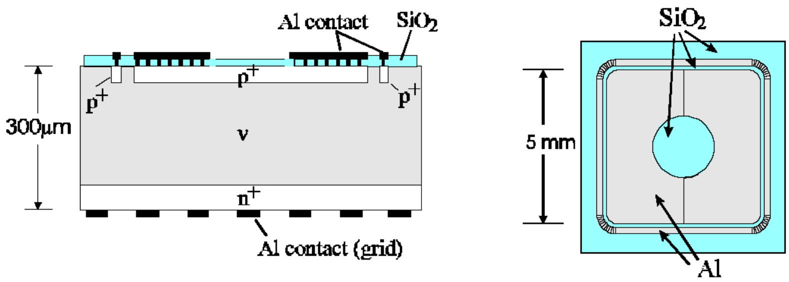

Fig. 53 : Typical silicon pad-diode design, as irradiated in this test (taken from [51]).

The following figures show pre-irradiation CV-IV characterization of those diodes. The results are in agreement with those we received from Hamburg, quoting depletion voltages around 65 V and leakage currents of 0.4 nA for oxygenated silicon or 0.8-0.94 nA for standard silicon.

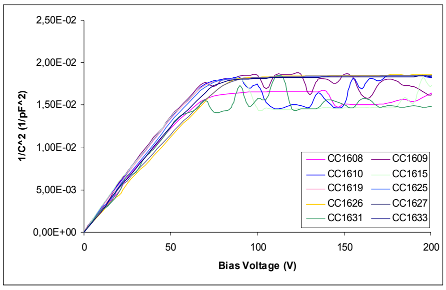

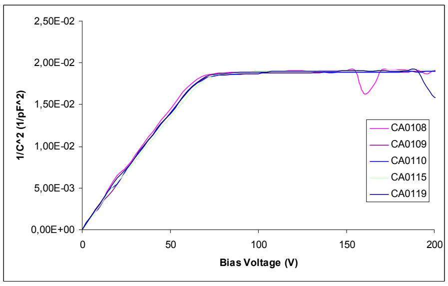

Fig. 54a, b : Oxygenated (left) and standard (right) silicon diodes CV curves before irradiation.

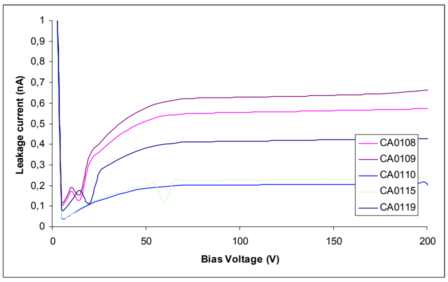

Fig. 55: Oxygenated & standard silicon diodes IV curves before irradiation.

Previous data and literature mention that all these diodes are known to show an "alpha parameter" of 4 10^{-17} A.cm, obtained after proper normalizations of the leakage current shown after irradiation to the volume of the device and to a 1-MeV neutron equivalent fluence (cf. 4.1.3).

4.1.2. Monoenergetic neutron beam line ("Q" beam line)

The details of the quasi-monoenergetic neutron beam are described in [54]. We recall the interesting features for our test, as well as the limitations and drawbacks.

In the so-called Q beam line, neutrons are generated from a primary proton beam hitting an isotopic ^{7}Li target via the ^{7}Li(p,n)^{7}Be reaction (Fig. 56). The remaining charged particles are wiped out of the beam using a magnet and a graphite beam dump.

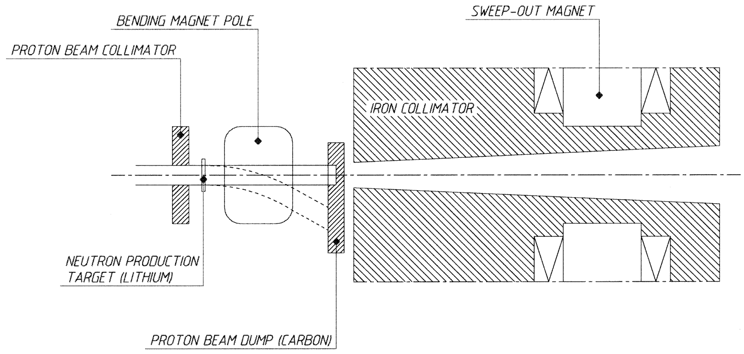

Fig. 56 : Quasi-monoenergetic beam neutron production in Louvain-la-Neuve.

The beam has been characterized for two different target thicknesses [54]. Despite lower neutron fluxes, we preferred the thin (3mm) lithium target to ensure a beam as monoenergetic as possible. The corresponding neutron energy spectra for 3 different proton energies used here are shown in Fig. 57.

We spent 3 days to carry this test, one day for each proton energy. This gives the opportunity to determine NIEL factors well above 20 MeV, where simulations predict a smooth and monotonic behaviour of the hardness factor curve.

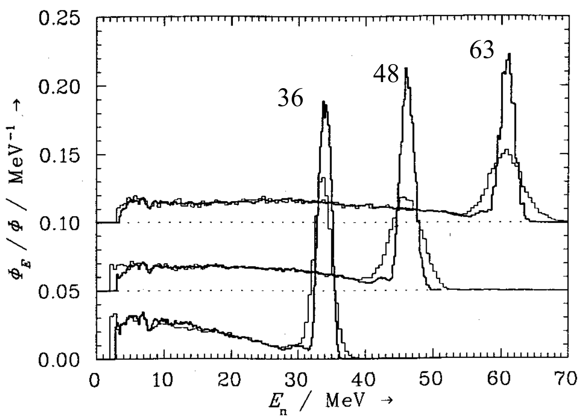

Fig. 57 : Monoenergetic simulated and measured neutron spectra for incident proton energies of 36, 48 and 63 MeV.

Typical fluxes obtained with this facility are around 10^6 n/s with an homogeneity of 10 % within a 30 mm beam spot diameter (at 3 m from the Lithium target). Compared to the intense fast neutron beam line, this flux is smaller by several orders of magnitude.

The fluences reached in the monoenergetic neutron test are therefore very low and causing much less radiation damage. To determine these fluences, we only monitored the intensity of the primary proton beam. We had no other dosimetry system ready for this test since our alanine dosimeters are not sensitive enough and as TLD's would have needed a calibration which we had no time to perform. We obtained integrated proton beam intensities of 228.3 µAh, 237.6 µAh and 187.2 µAh for respective neutron peak energies of respectively 33, 46 and 60 MeV.

The total fluence calculations gave the following values: 6.8 10^{10} n/cm^2, 7.1 10^{10} n/cm^2 and 7.9 10^{10} n/cm^2 for the neutron peak energies of respectively 33, 46 and 60 MeV. Integrated beam measurements and fluence calculations are summarized in Table 12.

Neutron peak energy (MeV)	Integrated proton beam current (µAh)	Fluence at sample position (n/cm^2)
33 ± 2.38	228.3	6.8 10^{10}
46 ± 2.5	237.6	7.1 10^{10}
60 ± 2.61	187.2	7.9 10^{10}

Table 12 : Integrated beam time and fluence summary for the monoenergetic neutron beam.

As a consequence of the low fluences reached, the damage measurements on the diodes have to rely only on the evolution of the leakage current, the depletion voltages being barely affected.

4.1.3. Principle of the test

The radiation-induced variation of the leakage current, discussed in 2.3.3, scales with the normalized fluence and volume of the device. Given the leakage current normalized to the actual neutron fluence, we obtain the total hardness factor of the beam by dividing it by the known alpha parameter found in the literature (e.g. in [32]), which is 3.99 ± 0.33 10^{-17} A/cm (4.3).

$$\Delta I_{leak} = \alpha_{lit.} \Phi_{1-MeV} V \tag{4.1}$$

$$\Phi_{1-MeV} = \kappa_{beam} \Phi_{real} \tag{4.2}$$

$$\kappa_{beam} = \frac{\Delta I_{leak}}{\alpha_{lit.} \Phi_{real} V} \tag{4.3}$$

As mentioned above in this section, we use here the fact that the neutron beam is quasi-monoenergetic. The energy spectrum can be split in 2 parts, and this will help us to compute hardness factors for neutrons above 20 MeV in a way depicted in equations (4.4) trough (4.7).

In the NIEL approximation, the 1-MeV neutron-equivalent hardness factor of a beam is usually computed by folding the energy spectrum with a damage function $\kappa(E)$, which is the total displacement damage normalized to the damage of 1-MeV neutrons (cf. 2.3.2).

$$\kappa_{beam} = \frac{\int_E \frac{d\Phi(E)}{dE} \kappa(E) dE}{\int_E \frac{d\Phi(E)}{dE} dE} = \frac{\int_E \frac{d\Phi(E)}{dE} \kappa(E) dE}{\Phi_{tot}} \tag{4.4}$$

As we want to obtain the hardness factor of the peak neutrons, we should compute the following hardness factor:

$$\kappa_{peak} = \frac{\int_{E_{treshold}}^{E_{end}} \frac{d\Phi(E)}{dE} \kappa(E) dE}{\int_{E_{treshold}}^{E_{end}} \frac{d\Phi(E)}{dE} dE} = \frac{\int_{E_{treshold}}^{E_{end}} \frac{d\Phi(E)}{dE} \kappa(E) dE}{\Phi_{peak}} \tag{4.5}$$

$E_{treshold}$ and E_{end} being the two energy limits of the peak region.

As the energy spectrum of the neutron beam is known (Fig. 57), this can be done assuming the hardness factors for energies below the peak are valid.

Naming ‘background” the lower-energy part of the spectrum, we compute the “background” hardness factor using (4.6).

$$\kappa_{bkg} = \frac{\int_0^{E_{treshold}} \frac{d\Phi(E)}{dE}\kappa(E)dE}{\int_0^{E_{treshold}} \frac{d\Phi(E)}{dE}dE} = \frac{\int_0^{E_{treshold}} \frac{d\Phi(E)}{dE}\kappa(E)dE}{\Phi_{bkg}} \qquad (4.6)$$

From these 3 last equations we obtain the expression for κ_{peak} in (4.7).

$$\kappa_{beam} = \frac{\int_0^{E_{treshold}} \frac{d\Phi(E)}{dE}\kappa(E)dE + \int_{E_{treshold}}^{E_{end}} \frac{d\Phi(E)}{dE}\kappa(E)dE}{\Phi_{tot}}$$

$$\frac{\int_{E_{treshold}}^{E_{end}} \frac{d\Phi(E)}{dE}\kappa(E)dE}{\Phi_{tot}} = \kappa_{beam} - \frac{\int_0^{E_{treshold}} \frac{d\Phi(E)}{dE}\kappa(E)dE}{\Phi_{tot}}$$

$$\frac{\int_{E_{treshold}}^{E_{end}} \frac{d\Phi(E)}{dE}\kappa(E)dE}{\Phi_{tot}} \frac{\Phi_{tot}}{\Phi_{peak}} = \left(\kappa_{beam} - \frac{\int_0^{E_{treshold}} \frac{d\Phi(E)}{dE}\kappa(E)dE}{\Phi_{tot}} \frac{\Phi_{bkg}}{\Phi_{bkg}} \right) \frac{\Phi_{tot}}{\Phi_{peak}}$$

$$\kappa_{peak} = \left(\kappa_{beam} - \kappa_{bkg} \frac{\Phi_{bkg}}{\Phi_{tot}} \right) \frac{\Phi_{tot}}{\Phi_{peak}} \qquad (4.7)$$

The analysis at the three different neutron peak energies is done assuming the published hardness factors are valid over the whole energy range and this, independently of the results obtained for lower energies during the higher energy irradiations.

Starting the interpretation of data with the 33 MeV data and going further on with increasing energy up to 46 and 60 MeV, the results will either confirm the values in the literature or, in case of discrepancies, will give an idea of the point where the experimental NIEL hardness factors start to diverge from the simulated ones.

4.1.4. Post-irradiation measurements and calculations

Before going through the analysis of the leakage current, a few CV measurements performed on the irradiated diodes are useful to illustrate the above mentioned fact that depletion voltages are barely affected by the irradiations. This is pictured in Fig. 58, where one clearly sees that the kink locating the depletion voltage is located at very similar positions, not only at the different annealing stages after irradiation, but also before and after irradiation. The differences in the evaluated depletion voltages between all measurements is less than 5 V.

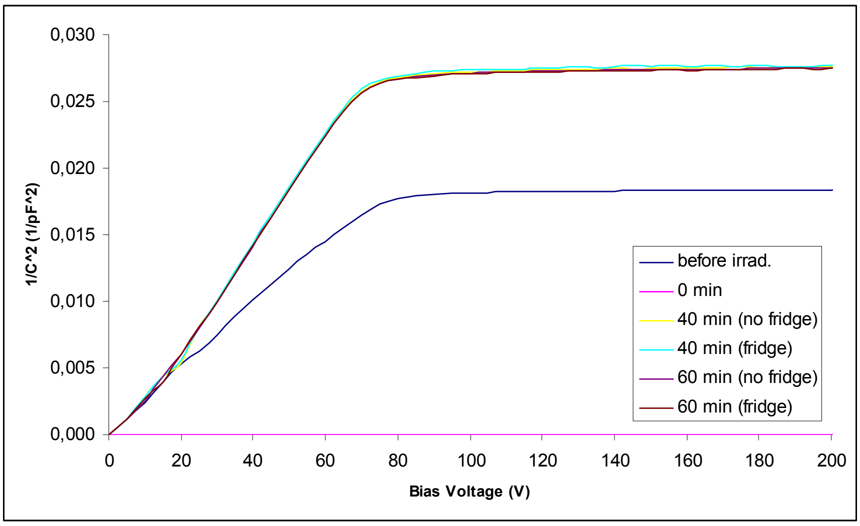

Fig. 58 : Comparison of the CV curves before and after irradiation for each annealing step on diode cc16-09, irradiated with 33 MeV neutrons at a fluence of 6.8 10^{10} n/cm^2.

The IV measurements were performed with the guard ring of the diodes connected in order to keep control of the volume concerned with the leakage current. This leads to a better estimation of the alpha parameter used to determine the hardness factor of the beam and hence to obtain more reliable hardness factors. Another key point when performing measurements after heat treatments is the impact of a radiation-induced and heat-activated bistable defect [43], which can artificially increase the leakage current right after the annealing treatment. The comparison of the curves labelled “fridge or “no fridge” for a given annealing time on Fig. 59 illustrates the fact that this bistable defect has no or only small impact in the case of the irradiations performed here. Indeed, difference of leakage current between measurements performed right after the heat treatment and then after some time in a fridge is of the order of two percent (0.5 nA over about 35). This is probably due to the low fluence reached and the relatively short annealing steps between measurements. However, care has been taken to leave the structures in a fridge for one night between each annealing step and the measurement. Measurements were done around 20 °C and corrected for the small temperature offset of the chuck.

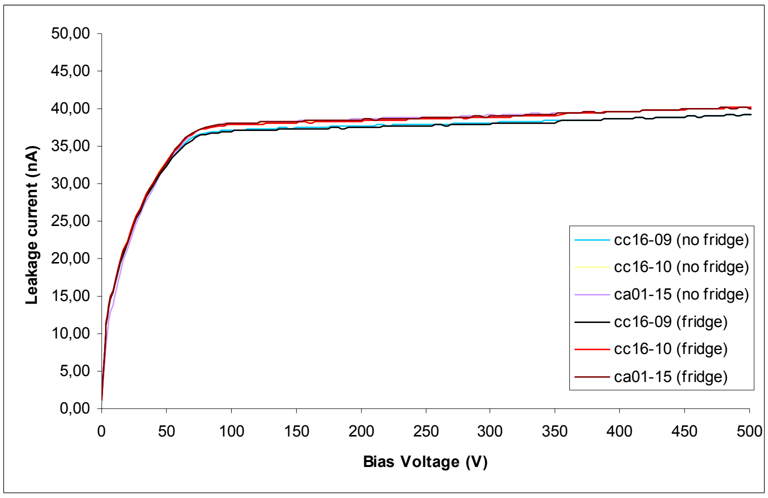

Fig. 59 : Comparison of the leakage current on diodes pre- and post-storage in a fridge after an annealing step of 20 minutes at 60 °C. The diodes were irradiated with 33 MeV neutrons for a real fluence of 6.8 10^{10} n/cm^2.

The tests were also performed after different annealing steps to check whether the annealing curves match those published in the literature. On Fig. 60 (where the data are already normalized using the total beam hardness factors computed below), the alpha parameter annealing points are shown for all diodes measured in this test. These are found to be close to published curves and thus the following sections will only report on the leakage current values after 80 minutes at 60 °C, the most widely used annealing condition for silicon devices*, for which the alpha parameter has widely been studied.

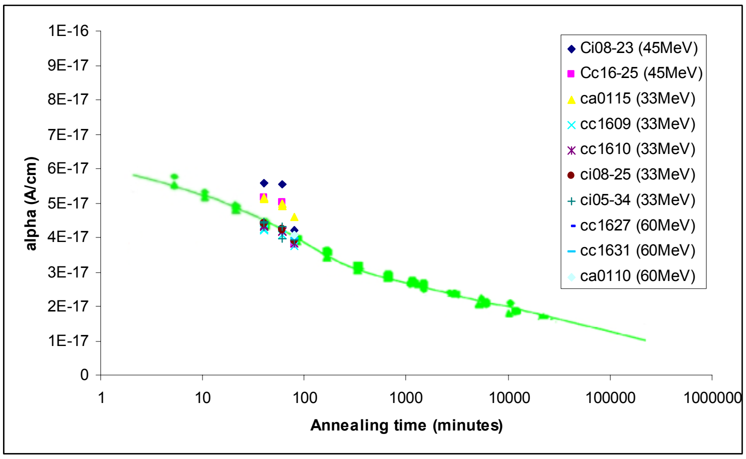

Fig. 60 : Evolution of the alpha parameter measured on the diodes for different neutron energies, compared to literature [32].

4.1.4.a. Measurements at 33 MeV

The variation of the average leakage current obtained with 5 diodes (whether oxygenated or not, these show the same leakage current) is 51.7 ±13 nA. Using equations (4.1) to (4.3), this corresponds to a 1-MeV equivalent fluence of $1.29\ 10^{11} \pm 4.85\ 10^{10}$ n/cm^2.

The actual neutron fluence, obtained from the integrated proton beam current and the neutron beam calibration, is $6.8\ 10^{10}$ n/cm^2 (cf. Table 12) and hence the global hardness factor for the 33 MeV neutron beam is 1.90 ± 0.16. Applying equation (4.7) with a computed background hardness of 1.77, one obtains a 33 MeV hardness factor of 2.05 ± 0.56.

4.1.4.b. Measurements at 46 MeV

The same method has been applied to the readings of the leakage current obtained with diodes irradiated with 46 MeV neutrons. The average increase of the leakage current observed is of 43.6 ± 3.4 nA corresponding to a 1-

* Corresponding to approximately 14 days at room temperature, it offers a good control of the annealing and is less sensitive to oven temperature variations than it's 4 minutes at 80 °C alternative.

MeV neutron equivalent fluence of $1.56\ 10^{11} \pm 1.12\ 10^{10}$ n.cm^2 whereas the total actual fluence is $7.07\ 10^{10}$ n/cm^2.

The beam hardness parameter obtained is hence 2.20 ± 0.17, for a background hardness factor found of 1.90. The computed hardness factor for peak neutrons at 46 MeV is 2.58 ± 0.66, not exactly matching 1.9 as quoted in [42], but this value is almost within our errors.

4.1.4.c. Measurements at 60 MeV

The increase of the average leakage current is 38.1 ± 0.6 nA. Divided by the diode volume and the usual $3.99\ 10^{-17}$ A/cm alpha parameter, a 1-Mev equivalent fluence of $1.36\ 10^{11} \pm 2\ 10^{9}$ n/cm^2 is obtained. Dividing again this result with the tabulated actual fluence of $7.87\ 10^{11}$ n/cm^2, the corresponding beam hardness factor is 1.72 ± 0.02.

In spite of the results obtained at 46 MeV, the tabulated hardness factors found in [42] have been used to compute a background hardness factor of 1.98 in the case of the 60 MeV neutron beam.

These considerations lead to a 60 MeV neutron experimental hardness factor of 1.26 ± 0.61, much lower than the 46 MeV one, but compatible with the value quoted in the literature (1.64).

4.1.5. Summary and comparison with literature

As foreseen from the neutron fluxes and fluences reached, a few measurements on the irradiated diodes proved that the depletion voltage of the diodes were barely affected by the irradiation; we are thus left with the single possibility to determine hardness factors using the increase of the leakage current. This increase, if considerably lower in this test than with the CMS tests concerned in the next sections, has been found to be large enough to be accurately measured with the probe station and its associated equipment, taking care to keep it light tight to avoid any perturbation of the measurement.

The results are summarized in Table 13 and compared to previous data in Fig. 61.

Neutron peak energy (MeV)	Hardness factor
33 ± 2.38	2.05 ± 0.56
46 ± 2.5	2.58 ± 0.66
60 ± 2.61	1.26 ± 0.61

Table 13 : Summary of the experimental hardness factor determination results.

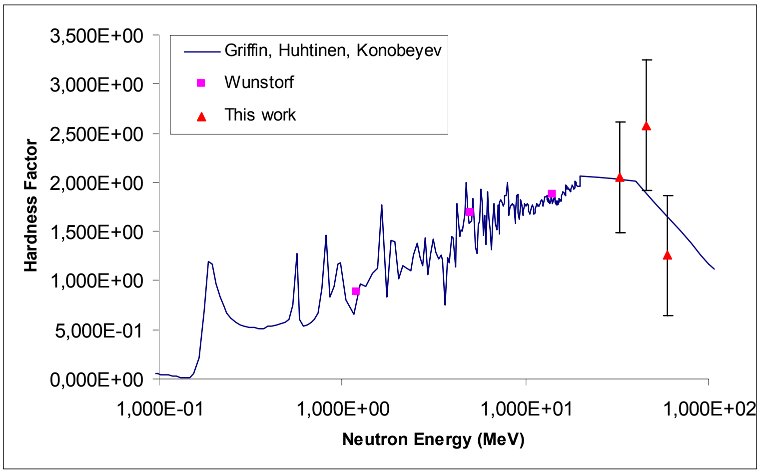

Fig. 61 : Neutron hardness factors as compiled from literature ([42] and [52]) compared to results obtained at Louvain-la-Neuve with the monoenergetic neutron beam line.

Our data point at 33 MeV neutron peak energy matches with 2.04, quoted for neutrons of 30 MeV in [41] or [42]. The results obtained at 46 and 60 MeV are not on the curve quoted in the literature. However, the error bars do not allow to draw any conclusion pointing towards the fact that previous simulations are wrong. Furthermore, the fact that the results are either higher or lower than the latter do not even indicate any tendency of the hardness factors to be actually lower than those quoted here, as expected by some [55].

4.2. Analysis of CMS test structures

This section is dedicated to the results obtained during the irradiation of the CMS tracker sensors. During the years 2001 to 2004, we performed in this context the irradiation of more than 460 test structures and 25 full-sized sensors, sampling the major part of the production from both vendors (ST microelectronics and Hamamatsu photonics). This gave us a unique opportunity to study the evolution of all relevant electrical properties on a statistical basis.

In this scope, we obtained some fluence-related evolutions of the parameters and investigated on the influence of bias during irradiation. Before entering into the details of the statistical analysis, two sections will be dedicated to MOS devices and interstrip capacitances which have a completely different behaviour before and after irradiation. Other parameters, linked to the bulk or surface-related damage are investigated afterwards.

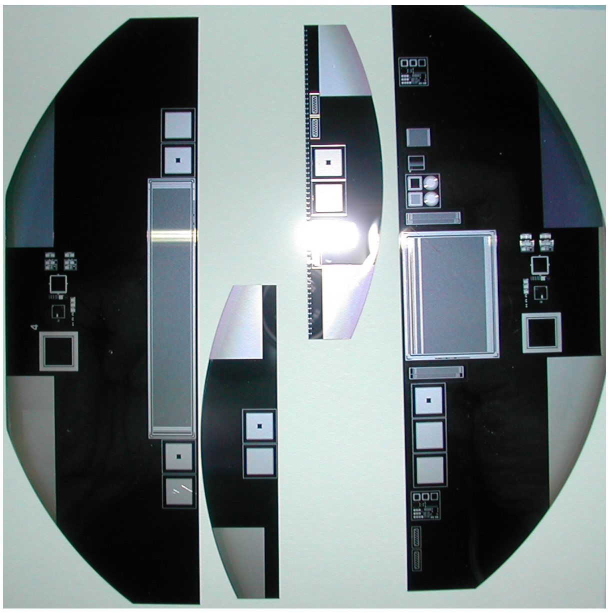

Fig. 62 : The 4 half moons cut around a Hamamatsu sensor (the standard structure is the right one).

Let us introduce here the CMS test-structures. They are produced with the cut-off pieces left around the full-sized sensors after dicing of the silicon wafer. Their production does not lead to major additional costs and it offers a great opportunity to make specific structures useful to check the quality of the sensors and to perform a wide range of tests without damaging the useful active part of the wafer. Due to their rounded shape, they are called "halfmoons" (Fig. 62). Among the four halfmoons produced on every wafer, one of these remains the same for all detector designs.

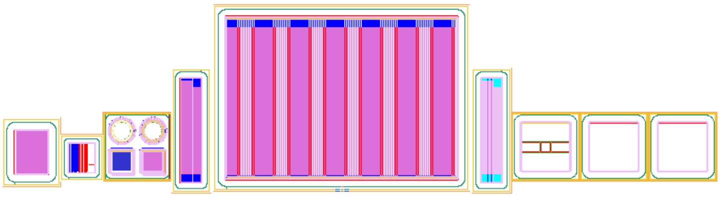

Fig. 63 : The standard CMS test-structure devices.

Pictured on Fig. 63, this test structure has (from left to right):

- An array of 26 AC-coupled strips like those present on the sensors, without the bias resistors;
- A set of nine structures dedicated to the measurement of resistances: three implant strips, three bias resistors, three aluminium strips;
- A set of four gate controlled diodes among which two square and two round ones;
- A second array of AC-coupled strips, but now the aluminization of these are connected together to facilitate grounding;
- A small-sized silicon strip detector (baby detector) with all features of the full-sized one;
- A third array of AC-coupled strips, but this time these strips are not connected in any way to a bias ring;
- A photodiode, quite similar to planar test diodes used e.g. by the RD48 collaboration when elaborating the HH model;
- Two MOS devices.

This set of nine test structures allow an accurate characterisation of all parameters of the silicon sensor and the small-sized strip detector serves as a reference structure for our irradiation tests.

The baby detector has 192 strips, placed 120 µm apart from each other. As a replica of the full-sized model, it has 1.5 MΩ bias resistors, a bias ring and a guard ring. Until the end of this chapter, all measurements are performed on this device unless otherwise stated.

4.2.1. The impact of bulk biasing during irradiation

The first study presented here will be the impact of the bias voltage during irradiation on the electrical properties of the so-called "baby detectors", built on the CMS standard test structures. As mentioned in 2.3.5, previous studies have been published in the literature, and we would like to compare their results in the context of our own work.

The sample studied here is made of 60 structures of both thicknesses, irradiated during the last tests of 2004. These have been chosen because they were made by a single vendor (Hamamatsu) and they have all been submitted to the same manufacturing process (not modified during their production). All of them passed the whole CMS irradiation qualification process and all have very similar initial properties (e.g. resistivity). The irradiation has been performed as usual with neutrons, at a temperature of –10 °C and under 600 V bias for the biased structures. The post-irradiation annealing is also standard (80 minutes at 60 °C) and the structures have been left afterwards for at least one night in the fridge before any measurement. The reference bias voltage for all strip parameters is 400 V, as defined in the CMS-IQC protocol.

This section deals only with the impact of bias on the evolution of the electrical properties. Hence we do not go into much detail: it is not necessary to perform a study in terms of e.g. the Hamburg model. However, as fluences vary from structure to structure, it is relevant to look at some variables using a normalization based on fluences. We will see here that the tests did not show any impact of the bias in our case.

Bulk parameters

Before entering into the details of measurements on the strips, let us take a look at the bulk properties, focusing on the macroscopic measurements of leakage current and depletion voltage.

Fig. 64 plots the fluence as a function of the total leakage current for baby detectors after irradiation. For every graph in this section, diamonds show the results of irradiation-biased structures and squares show the results of unbiased ones.

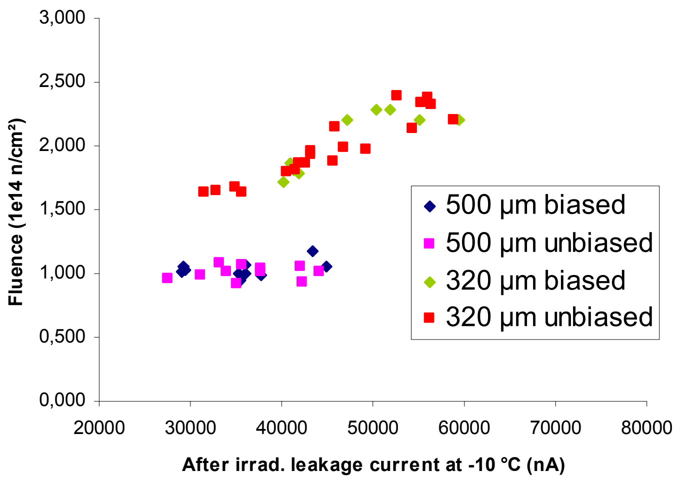

Fig. 64: Post-irradiation leakage current of biased and unbiased standard test structures.

As in Fig. 64, the leakage currents for thick and thin structures do not allow to decide upon any influence of the bias during irradiation. For similar fluences, the biased and unbiased samples of the same thickness give similar leakage currents. When we compare the average values of the alpha parameter measured at –10 °C, we obtain the following:

Structures	Average value (nA/cm)
320 µm - Biased	2.19 ± 0.39
320 µm - Unbiased	2.18 ± 0.18
500 µm - Biased	2.62 ± 0.55
500 µm - Unbiased	2.18 ± 0.25

Table 14 : Biased-unbiased alpha parameter comparison.

This clearly shows that the bias voltage does not seem to have any impact on the bulk leakage, hence confirming the observations made by Cindro et al [35], where permanently biased or unbiased structures have shown to have the same leakage currents. It also gives a first confirmation of the well-known result that the alpha parameter does not depend on the initial bulk resistivity of the material. We will give more details about this later.

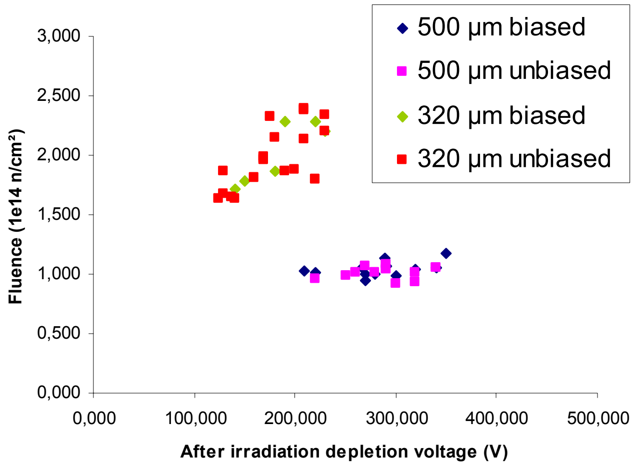

Fig. 65 : Post-irradiation depletion voltages of the biased-unbiased sample.

Fig. 65 gives the same plot for the depletion voltages after irradiation. On each sample, the average values and standard deviations of depletion voltages and fluences are in fact compatible for structures of the same type :

	Biased	Unbiased
Thick structures	$<\Phi_{1\ MeV}>=1.03\pm0.06\ 10^{14}n/cm^2$	$<\Phi_{1\ MeV}>=1.02\pm0.07\ 10^{14}n/cm^2$
	$<V_{dep}>=283\pm42$ V	$<V_{dep}>=294\pm45$ V
Thin structures	$<\Phi_{1\ MeV}>=2.05\pm0.22\ 10^{14}n/cm^2$	$<\Phi_{1\ MeV}>=2.98\pm0.25\ 10^{14}n/cm^2$
	$<V_{dep}>=185\pm36$ V	$<V_{dep}>=178\pm35$ V

Table 15 : Average and standard deviation values of the depletion voltages.

To confirm all this in a quantitative way, we performed and compared linear regressions on the data from each sample.

This approximation of the Hamburg model is valid since all the fluences concerned here are well above those for type inversion: the effective doping concentrations for a given fluence and for a single annealing step at a given temperature, can then be considered as a linear function of the 1-MeV equivalent fluence (4.8). Indeed, for high resistivity silicon, the constant c is usually above 20 10^{-14} cm^2/n. Moreover, at a fluence of 10^{14} n/cm^2 the non-linear term is well below 10^{-9}.

$$N_{eff}(\Phi_{eq},t_a,T_a) = N_{eff,0}\left(1 - r(1-e^{-c\Phi_{eq}})\right) - \Phi_{eq}\left(g_c + g_a e^{-\frac{t_a}{\tau_{a,T_a}}} + g_y(1-e^{-\frac{t_a}{\tau_{y,T_a}}})\right) \quad (4.8)$$

Unfortunately, our samples are composed of structures irradiated at very similar fluences, and the uncertainties on fluences and depletion voltages lead to large errors on the regression coefficients, and consequently to high χ^2 for every regression. The results were that the obtained regression parameters were compatible with each other (no influence of biasing during irradiation), but also that the statistical significance was very low. Therefore we confirm our initial statement: according to our experience, bias has no influence on the depletion voltage.

This result seems somewhat different from the one quoted by Cindro et al ([35] and [36]), where permanently biased structures have shown different effective doping concentration compared to unbiased ones. When permanently biased, those structures have effective doping concentration twice as high as those for the unbiased structures. This has been discussed above, and there is no discrepancy with our results as the difference of the depletion voltage tends to vanish if both samples are left unbiased for a period about 50-100 h: this was the case in our conditions.

A further compatibility check would be to bias our detectors for a much longer period and see if the full depletion voltages rise. This test would need new irradiations and a careful annealing in conditions similar to those pictured in [35], as any annealing behaviour is highly temperature-dependent.

Strip parameters

We did not find any impact of bias during irradiation on the bulk parameters. But is it the same for strip properties like bias resistors, the coupling and interstrip capacitances? This is what we quickly inspect in the present paragraph. Let us start with the bias resistors.

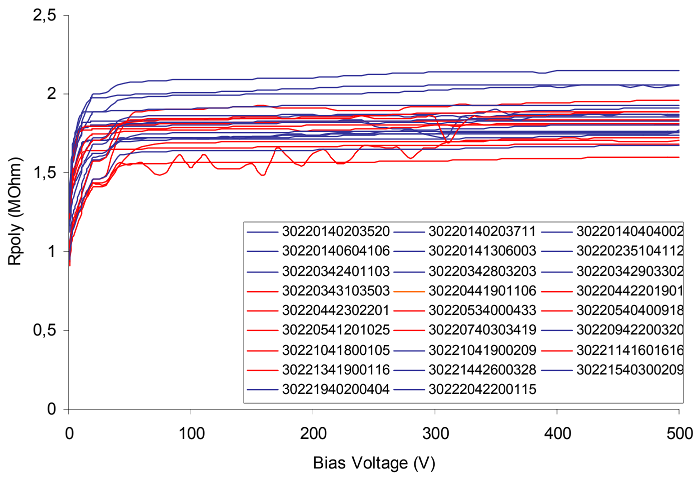

Fig. 66 : After irrad. R_{poly} ramps on biased (red) and unbiased (blue) thick and thin structures.

As shown above, the measurements of the bias resistor quickly reach saturation values, even on a slightly biased detector. Also, according to the distributions of the variations (Fig. 67), it seems that the impact of irradiations is very limited and seems to be fairly independent of the dose.

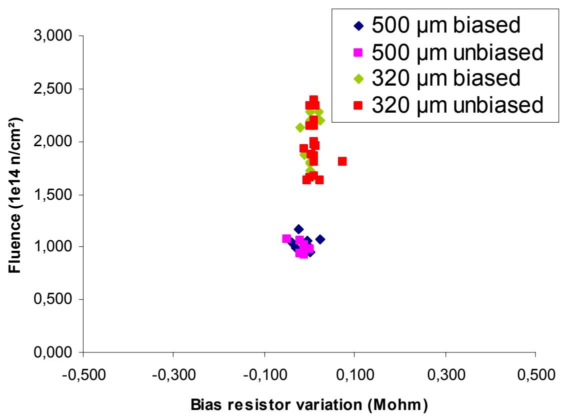

Fig. 67 : Variation of the bias resistors on biased/unbiased samples, taken at 400 V bias.

Due to this apparent independence on the dose, we will directly look at the variations of the average values of the resistors: indeed the relative variations are found to be less than a percent. The average values and standard deviations of the samples are listed in Table 16. As for the bulk parameters, they again point towards damages independent of bias.

	Biased	Unbiased
Thick structures	$<\Delta R_{poly}>=-1.07\pm1.73$ %	$<\Delta R_{poly}>=-0.92\pm0.86$ %
Thin structures	$<\Delta R_{poly}>=0.14\pm0.74$ %	$<\Delta R_{poly}>=0.60\pm0.94$ %

Table 16 : Average & standard deviation values for the bias resistor variation of biased and unbiased samples.

The coupling capacitances, like polysilicon resistors, quickly reach a saturation value when the device starts to be biased. Hence, a simple look at the distributions of variations will give a first clue of the possible dependence on bias.

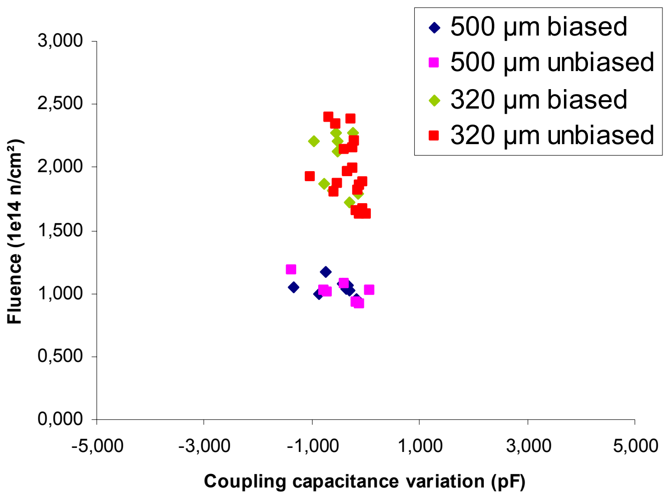

Fig. 68 : Coupling capacitance variation distributions on biased/unbiased samples, taken at 400 V bias.

Once again, from Fig. 68 there is no clear fluence dependence of the damage of the coupling capacitance. It is therefore interesting to look at averages and standard deviations of the samples (Table 17). Given these averages, one deduces a slight decrease of the coupling capacitances with irradiation, but no bias effect.

	Biased	Unbiased
Thick structures	$<\Delta C_{AC}>=-0.84\pm0.57$ %	$<\Delta C_{AC}>=-0.72\pm0.73$ %
Thin structures	$<\Delta C_{AC}>=0.75\pm0.39$ %	$<\Delta C_{AC}>=0.45\pm0.38$ %

Table 17 : Average & standard deviation values for the coupling capacitance variation of biased and unbiased samples.

About the interstrip capacitances, we have to consider their evolution with the sensor bias. Indeed, the interstrip capacitances do not reach a saturation value early in the bias ramp but instead show a decrease well above the depletion voltage. However, the large plateau in these curves allows us to use the standard test results anyway*, considering a bias level around 0.8 V_{dep}. In this way, we obtain the now usual distributions over fluence (Fig. 69).

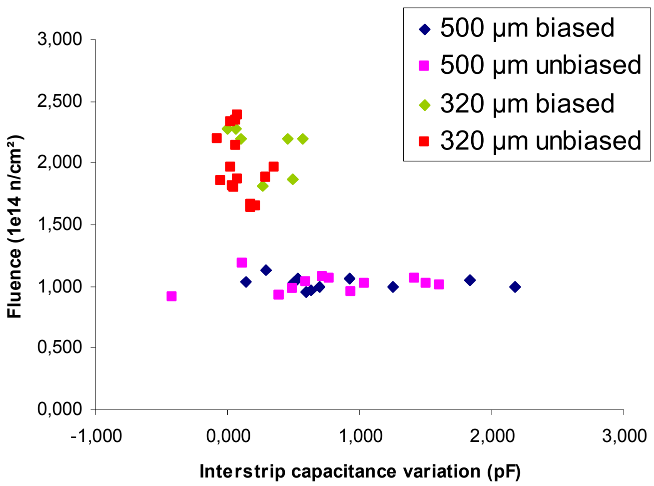

Fig. 69 : Distributions of the variations of the interstrip capacitance for biased/unbiased samples, taken at 400 V bias.

* Standard results are taken as the parameter value at 400 V bias.

One directly notices that all samples show an increase of the interstrip capacitance, but also that thick structures show a much broader spread of the variation of the capacitances. Both the increase and spread are directly related to the C_{int} saturation, and will hence not be discussed here, but later in this chapter. However and once again, the distributions seem to be similar for both biased and unbiased devices. The averages and standard deviations of each sample tend to confirm this statement, and we therefore conclude there is no evidence of a bias effect on the interstrip capacitances.

	Biased	Unbiased
Thick structures	$<\Delta C_{int}>=0.84\pm0.57$ pF	$<\Delta C_{int}>=0.69\pm0.63$ pF
Thin structures	$<\Delta C_{int}>=0.28\pm0.23$ pF	$<\Delta C_{int}>=0.10\pm0.12$ pF

Table 18 : Average and standard deviation values for the interstrip capacitance variation of biased and unbiased samples, taken at 400 V bias.

The interstrip resistances have a behaviour much more dependent on the bias conditions. Hence, it is crucial to look at the graphs showing these resistances as a function of the bias voltage than simply looking at the distribution of the scan values for a given bias voltage.

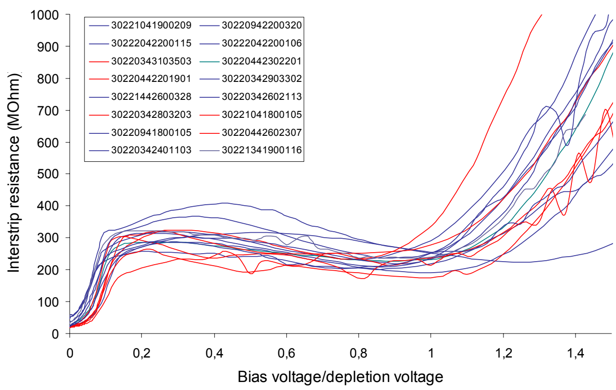

Fig. 70 : Interstrip resistance as a function of normalised bias for thick structures - Red lines show the results for the irradiation-biased structures.

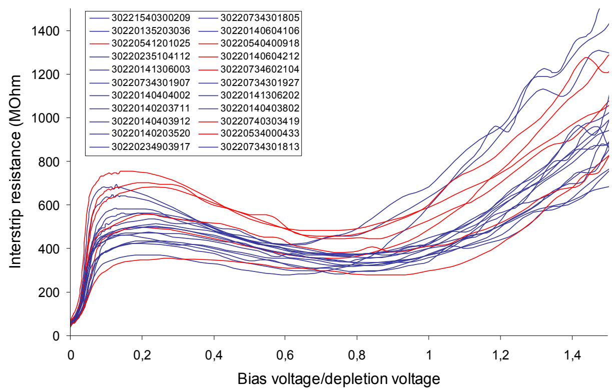

Fig. 71 : Interstrip resistance as a function of normalised bias for thin structures - Red lines show the results for the irradiation-biased structures.

All curves on Fig. 70 and Fig. 71 have seen their ordinates (the bias voltage) individually scaled according to the depletion voltages of the structures. This makes the comparison between all curves easier, and highlights their common features.

It is obvious that all scaled curves show the same behaviour, with a local minimum at about 0.8 V_{dep}. Fig. 72 then shows the Interstrip resistance versus fluence distribution at this bias.

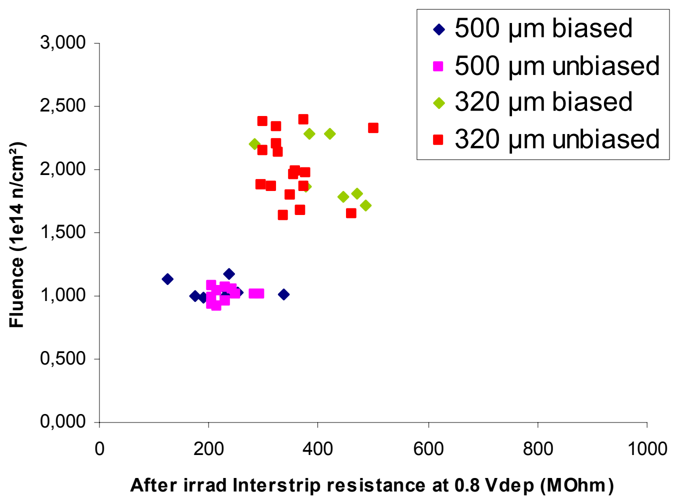

Fig. 72 : Interstrip resistance distributions on biased/unbiased samples.

Like in other cases, we do not see a clear correlation between interstrip resistance values and fluences. Table 19 summarises the average values and standard deviations on the samples: once again no influence of bias can be deduced.

	Biased	Unbiased
Thick structures	$\langle R_{int}\rangle$=222±58 MΩ	$\langle R_{int}\rangle$=224±30 MΩ
Thin structures	$\langle R_{int}\rangle$=409±69 MΩ	$\langle R_{int}\rangle$=354±54 MΩ

Table 19 : Average and standard deviation values for the interstrip resistance for biased and unbiased samples.

4.2.2. Summary of the irradiation results

Although we started the irradiations back in 2001, the data used for this analysis have mainly been collected during the 2003-2004 irradiations. This is due to the setup attached to the probe station which has been finalised after the second IQC workshop, held in Louvain-la-Neuve in May 2003. Hence, only the data collected thereafter are free of any setup-related constraint. The concerned data sample is made of data gathered on 228 structures and sensors, produced by both Hamamatsu and STM. As it has been demonstrated in the previous paragraph that the obtained results are independent of whether the device was biased during irradiation or not, we will consider here both cases within the same sample.

Bulk properties: leakage current

The comparison of the leakage current results with literature imposes a temperature correction of our measurements of the leakage current, obtained at −10 °C, to a standard temperature of 20 °C.

According to equation (2.4), the correction factor before irradiation is of 15.2. An experimental determination of this scaling factor gave 16.2 ± 0.5 for a CMS baby detector; and 18.3 at a reference 400 V bias voltage. But is this still valid after irradiation, or does the higher concentration of defects influence the leakage current so that it varies differently with the detector temperature? In order to check this, a measurement of the leakage current as a function of bias has been carried out for temperatures varying between –10 °C to 23 °C in steps of 1 °C. The results are discussed below.

Te device is a thin Hamamatsu baby detector, irradiated at a fluence of 2.22 10^{14} n/cm² and annealed as usual for 80 minutes at 60 °C. It has been cooled down in a fridge for a night between the annealing treatment and the measurement itself.

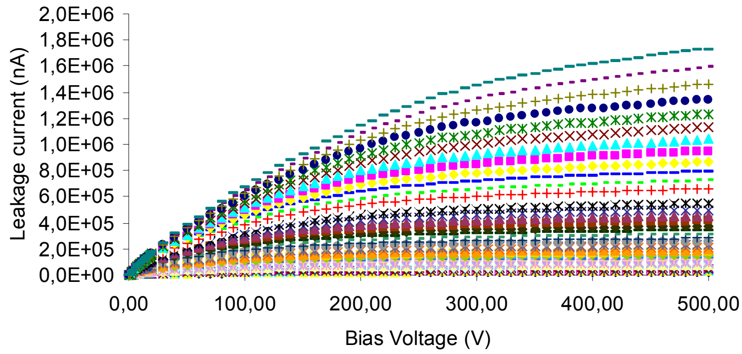

Fig. 73 : The leakage current of a baby detector after irradiation, at different temperatures.

The leakage current scaling factor from –10 °C to 20 °C, averaged over the entire curve, is of 15.6, to be compared with a theoretical factor of 15.54. At our reference bias voltage of 400 V, used by the collaboration to compare all leakage currents, the scaling factor is of 21.71, hence a bit higher than for a non-irradiated structure.

The post-irradiation measurements were performed at –10°C, this has been decided as the tracker will be operated cold, but also because the leakage current of irradiated full-size sensors may become too high for the power supply used in the different CMS probing labs. Hence this scaling factor is useful when considering a comparison with the literature.

Fig. 74 shows the distribution of the alpha parameter observed during our neutron irradiation tests. The observed alpha parameters observed, once scaled to 20 °C, are of 3.77 ± 0.64 10^{-17} A/cm for thin structures and 4.23 ± 0.61 10^{-17} A/cm for thick ones. Considering the whole set of measurements as a simple data set gives an alpha parameter of 4.23 ± 0.8 10^{-17} A/cm, to be compared with 3.99 ± 0.03 10^{-17} A/cm in [32].

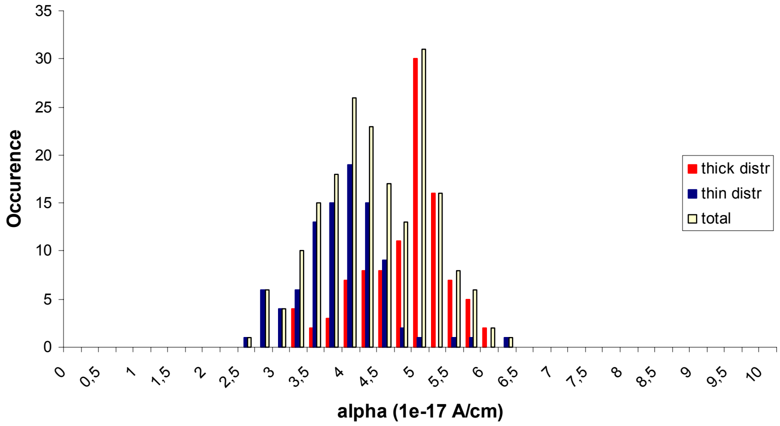

Fig. 74 : alpha distribution for thick and thin structures.

The leakage current obtained during the CMS irradiations is thus compatible with literature. A possible source for the difference in the averages and the spread of the distribution may be found in the fact that our measurements were not performed with a connected guard ring, leading to possible uncertainties on the size of the volume from which the current is drawn. The fluence uncertainty plays also a major role in the distribution spread.

Bulk properties: depletion voltage

At the occasion of the first neutron irradiations, standard RD48 diodes were put in the beam to get another reference for the fluence determination. This has been the occasion to perform an early annealing study at a temperature of 40°C to slow down the annealing processes.

This annealing study has been useful to show that the fluence normalisation is fine, as only the reverse annealing time constant had to be a bit changed from literature data. The results are shown on Fig. 75, where the experimental measurements are compared to predictions of the model. The parameters used here are quoted in Table 20.

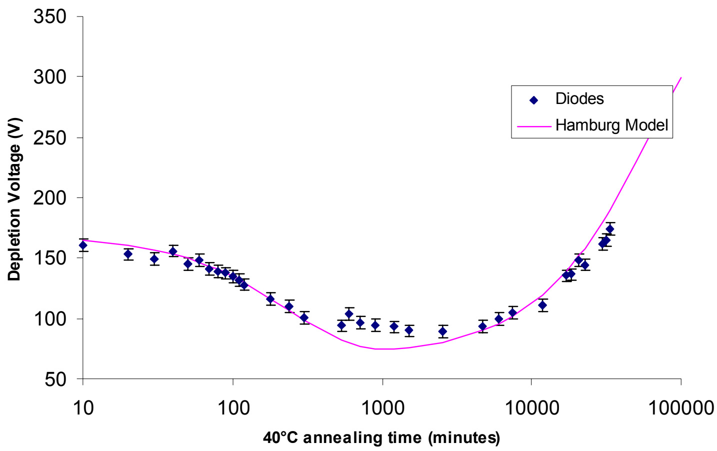

Fig. 75 : Standard diode annealing curve at 40°C.

Stable damage	$G_c = 1.5\ 10^{-2}$ 1/cm	$N_{c0}/N_{eff,0} = 0.8$	$C^*N_{eff,0} = 0.109$
Beneficial annealing	$G_a = 1.81\ 10^{-2}$ 1/cm	$\tau_a = 240$ min	
Reverse annealing	$G_y = 5.16\ 10^{-2}$ 1/cm	$\tau_y = 60000$ min	

Table 20 : Parameters used in the Hamburg model to compare expected values of the depletion voltage with the experimental data of the first irradiated diodes.

Coming to the irradiation of the CMS baby detectors, the application of the Hamburg model becomes a bit more difficult. As a reminder, the Hamburg model predicts in fact the evolution of the effective doping concentration as a function of the 1-MeV equivalent fluence and heat treatment of the detector. To compare the depletion voltages determined with the probe station, the model prediction has to take into account the effects of the geometry of the sensor to the depletion voltage as mentioned on page 35, equation (2.6).

On Fig. 76 and Fig. 77, a summary of all post-irradiation depletion voltages obtained in 2003-2004 is given, together with the Hamburg model predictions for a thick and a thin structure having the same geometry as standard CMS baby detectors, and with the average initial doping concentration observed during the production phase. Also, a thickness of 290 µm instead of 320 µm has been used according to HPK recommendations about the thin structures. This is due to a special wafer treatment we have not much details about.

The parameters injected in the Hamburg model to match these depletion voltages are given in Table 21 for the high resistivity sensors, in Table 22 for the thin low-resistivity ones. These parameters are directly taken from M. Moll's PhD thesis [32]. Using these parameters, an estimation of the depletion voltage using the Hamburg model has been computed for each structure, taking its geometry and initial depletion voltage into account. The average deviation of the predicted depletion voltage to the predicted one is found to be as less as 1 V. Unfortunately, the standard deviation of this deviation is about 70 V due again to the fluence spread.

Stable damage	$g_c = 1.56\ 10^{-2}$ 1/cm	$N_{c0}/N_{eff,0} = 0.56$	$C^*N_{eff,0} = 0.069$
Beneficial annealing	$g_a = 2.01\ 10^{-2}$ 1/cm	$T_a = 24.1$ min	
Reverse annealing	$g_y = 4.92\ 10^{-2}$ 1/cm	$T_y = 1010$ min	

Table 21 : Parameters used in the Hamburg model to fit the depletion voltage data of CMS 500 µm thick test structures.

Stable damage	$g_c = 1.43\ 10^{-2}$ 1/cm	$N_{c0}/N_{eff,0} = 0.64$	$C^*N_{eff,0} = 0.09$
Beneficial annealing	$g_a = 1.67\ 10^{-2}$ 1/cm	$T_a = 15.4$ min	
Reverse annealing	$g_y = 5.16\ 10^{-2}$ 1/cm	$T_y = 1160$ min	

Table 22 : Parameters used in the Hamburg model to fit the depletion voltage data of CMS 320 µm thin test structures.

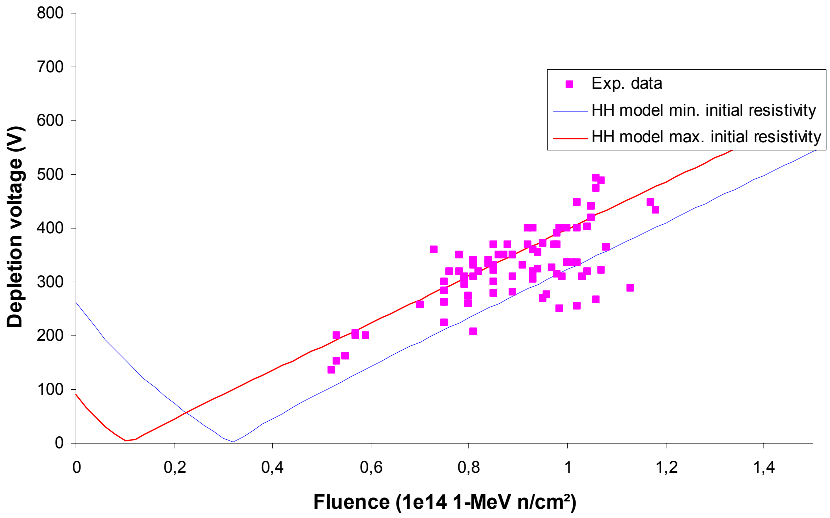

Fig. 76 : Post-irradiation depletion voltages obtained during the neutron irradiation tests in Louvain on 500 µm-thick CMS structures.

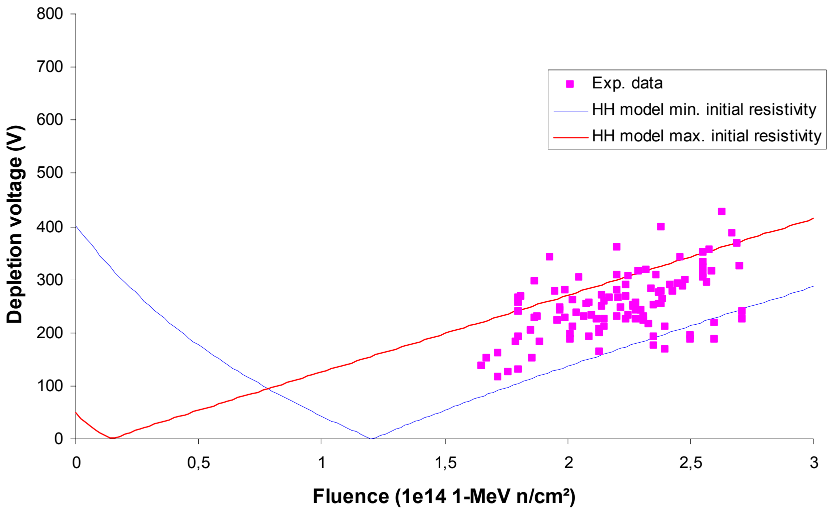

Fig. 77 : Post-irradiation depletion voltages obtained during the neutron irradiation tests in Louvain on 320 µm-thick CMS structures.

It is difficult, considering the depletion voltages obtained here, to obtain a better estimation of the Hamburg model parameters for the CMS structures. Indeed, given the fact that the average deviation to the model is small, an accurate re-estimation of these parameters would require an irradiation campaign at various different fluences, with several devices at each fluence and an annealing study for each of them.

It is also worth mentioning that the value of the reverse annealing parameters plays only a minor role on the interpretation of the results: with a single annealing step of 80 minutes at 60 °C, beneficial annealing is already well in progress whereas reverse annealing is only in its very early stage (with $1\text{-}e^{-80/Ty}$ being equal to 0.062 in equation (2.12), page 45). However, if all the other parameters were well-known, a fit of the annealing time constants with a single annealing state of the sensors would lead to a poor confidence in the fit results. Further discussions on these time constants will be found in S. Assouak's thesis.

Nevertheless, it is amazing to see that the parameters quoted in the literature give such a good idea of the evolution of the depletion voltage under neutron irradiation.

Triggered by a paper written by M. Mikuz et al. [37], a late study of the stability of the depletion voltage after irradiation has been done. This study was aimed to check whether the depletion voltage of an irradiated device raises when the structure is kept biased for a long time. The results quoted in the paper showed that the depletion voltage raises if the object is kept at room temperature, but nothing was indeed quoted for a device kept cold, as will be the case in CMS.

This stability measurement has been performed on a HPK IB1 test structure, irradiated in late 2004 at a fluence of 1.96 10^{14} n/cm². Like other structures, it has been annealed for 80 minutes at 60 °C. Its depletion voltage has been measured daily during 2 months and the structure has been kept biased at 400 V between measurements.

During the first phase of the test (blue diamonds on Fig. 78), it is found that the depletion voltage rises with a slope of 0.17 V/day; The test had to be interrupted because of probe station availability and the structure has been biased at room temperature for one day, enhancing reverse annealing due to lack of cooling and high leakage current. Afterwards, the red triangles on Fig. 78 show the follow-up of the test: the structure has been kept biased at low temperature again. the depletion voltage shows a step due to the annealing between the two parts of the test, but went increasing again afterwards.

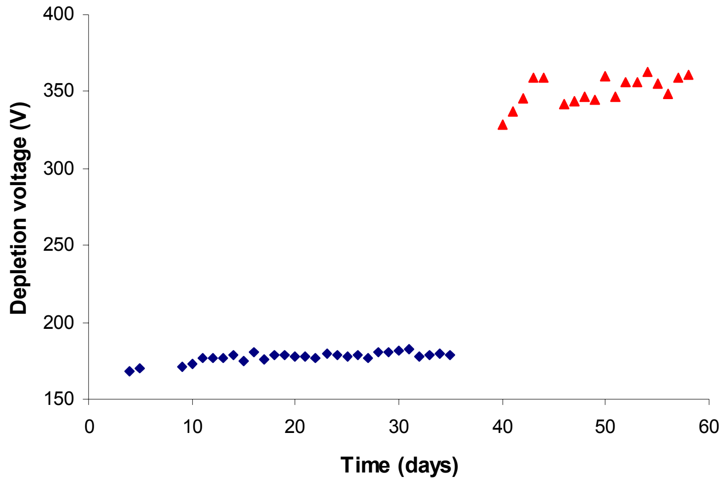

Fig. 78 : Evolution of the depletion voltage of an irradiated thin HPK structure kept biased at 400 V at –10 °C.

Looking at the first part of the test, a difference of 12 V between the initial depletion voltage and the final one is observed. This difference is relatively small but the evolution of the depletion voltages can be observed on the superposition of the kinks observed on the CV curves (Fig. 79).

In [35], the impact of this effect for the Atlas tracker, after 10 years at LHC, is estimated to be between 40 and 70 V, with an "activation rise time" quoted to be about 100 days at –7 °C. Our depletion voltage increase is compatible with such an increase rate as we obtain a 12 V rise in about one third of the time. Indeed, one would obtain an effect in the lower end of the range quoted in [35], due to a slightly lower operating temperature.

It is however regrettable that this test could not have been pursued for a longer period. It would for sure be interesting to perform a longer test over at least 4 months, to be extended as long as the depletion voltage rises. This test could bring a new view on the reproducibility of this effect, its saturation value and would eventually allow to give an estimation on its possible impact on the tracker.

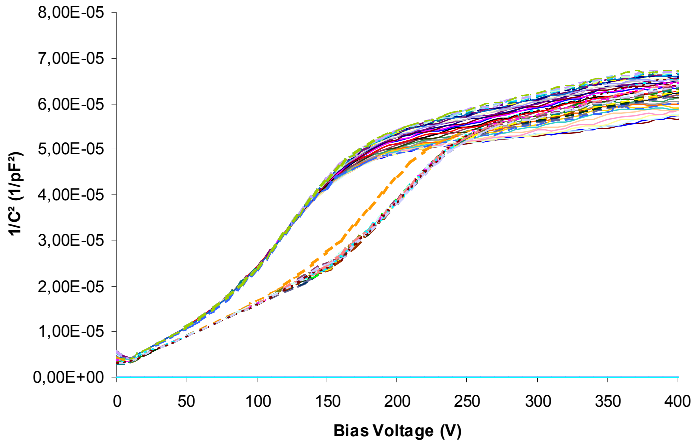

Fig. 79 : CV curves measured during the long term test.

Polysilicon resistances variation under irradiation

As already pointed out above, the polysilicon resistances do not seem to be heavily affected by neutron irradiation. This is confirmed to a larger extent on Fig. 80, where the most affected structures show a decrease of 3% only after a dose equivalent to 15 years at LHC.

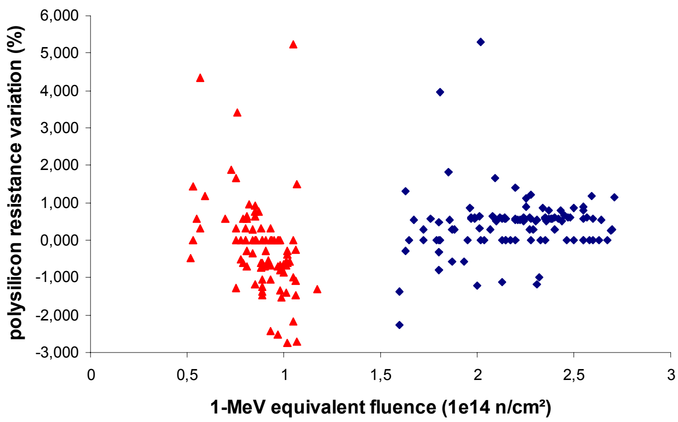

Fig. 80 : R_{poly} variation after irradiation (red triangles for thick structures, blue diamonds for thin ones).

However, it seems that the thick structures may show a decrease of the resistance. This should be further studied at higher doses as the spread of the variation distributions (Fig. 81) does not allow to firmly conclude anything about this so far.

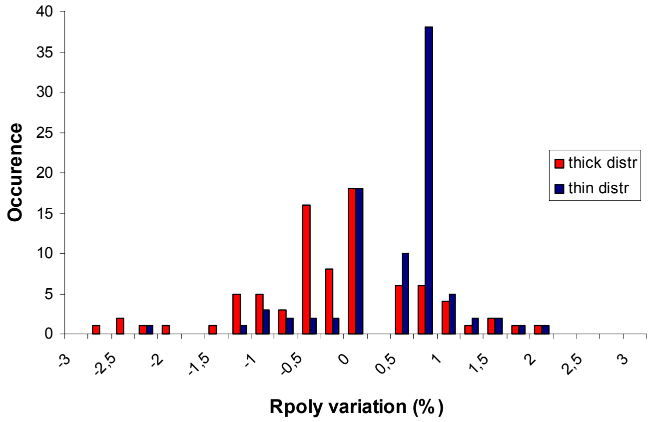

Fig. 81 : Distributions of the polysilicon variations after irradiation for thick and thin structures.

The average variations extracted from these distributions are the following: –0.185 % (3.2 kΩ) for thick structures and 0.64 % (11.1 kΩ) for thin ones with standard deviations of respectively 1.234 % and 1.96 %. These standard deviations are hence compatible with the absence of variation under neutron irradiation, and make our data sample irrelevant to deduce any further trend. Once again this stresses the complementarity of the neutron and proton irradiations performed in the CMS-IQC framework as our result differs from those obtained under proton irradiation where an increase of the bias resistance values is observed (about 350 kΩ and 150 kΩ for thin and thick structures respectively).

Coupling capacitance evolution under irradiation

Fig. 82 shows the evolution of the coupling capacitance as a function of the fluence, as Fig. 80 did it for polysilicon resistances.

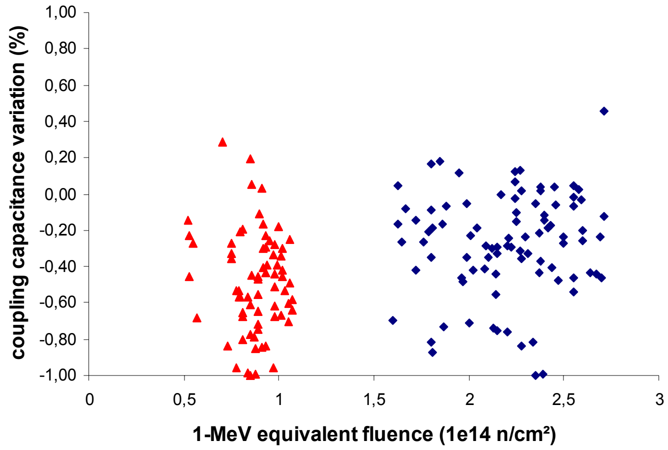

Fig. 82 : coupling capacitance variation expressed as percentage of the initial value for thick (red) and thin structures (blue)

Again, as mentioned when considering the impact of biasing, but this time on a larger sample size, a clear relation between fluence and coupling capacitance variation cannot be deduced although it seems that these capacitances slightly diminish when submitted to a radiation flux (Fig. 83).

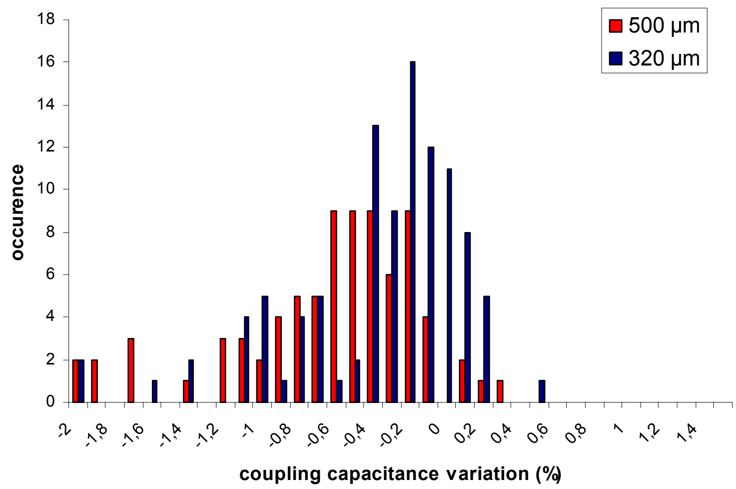

Fig. 83 : coupling capacitance variation distributions.

Indeed, the average variations are of –0.64 % for all data sets (thick, thin or global) and again the spreads are relatively high with standard deviations of 1.68 % for thin structures and 0.96 % for thick ones (the global standard deviation being of 1.45 % considering all structures together). This corresponds to a decrease of 0.07 pF to be compared to a typical decrease of about 1 pF observed on CMS structures under proton irradiation.

Interstrip resistances

Part of the ST production had a low R_{int} problem, but these structures where not irradiated as they did not pass the PQC and QTC steps of the CMS QA procedure. It is then no big surprise that it is found here that almost all tested structures and sensors were fine regarding the 20 MΩ minimal interstrip resistance criteria, apart a few ones which showed an evident other big failure.

As the interstrip resistance value is highly bias-dependent, a detailed analysis requires the individual inspection of the R_{int} versus bias ramp measurement. These ramps, are shown on the following figures, where the bias voltage is normalized to the depletion voltage to give a better idea of the bias status of each structure.

It can be noticed that the curves for the thick structures are similar to each other unlike those of the thin structures, which present more often an earlier increase. This is anyway not a source of concern since it means that the strips of thin structures have a better insulation between them, which is good regarding the noise performance of the sensors.

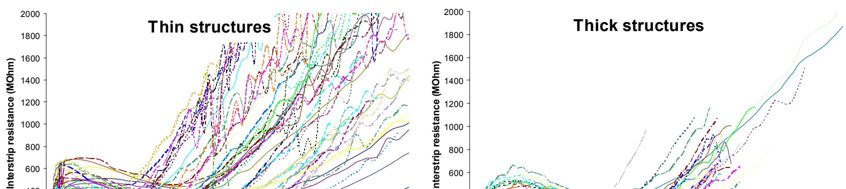

Fig. 84a, b : post-irradiation interstrip resistance as a function of the bias status for thin and thick test structures.

Fig. 85 shows the distribution of the value of the interstrip resistances at the local minima of the above curves, as a function of the fluence. The idea of the analysis is the same as before, and again there is no clear correlation between R_{int} and fluence for the fluences concerned here.

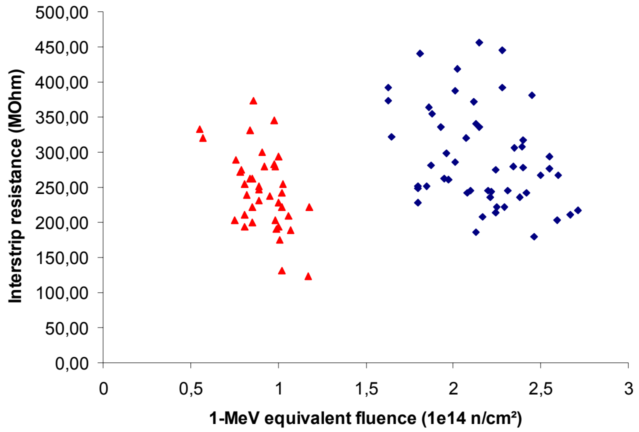

Fig. 85 : value at local minima of the curve.

At same bias status, the difference between thick and thin structures is not evident: respectively 245.6 ± 55 MΩ and 291.8 ± 70.3 MΩ. But it has been shown before that the thin structures generally have lower depletion voltages than thick ones, at a fluence of 10 years operation at LHC. Therefore, at the same bias voltage (400 V), thin structures show an average interstrip resistance of 1560 MΩ whereas thick ones present an average of 620 MΩ, again pointing in the direction of a better strip insulation.

Interstrip capacitance behaviour

In late 2003, a first summary of the results obtained under neutron irradiation had shown that thick structures present a bigger increase of the interstrip capacitance after irradiation. This effect remained constant thereafter as indeed, post-irradiation measurements at 400 V bias indicate that thick structures present an average increase of 0.55 pF whereas thin ones 0.13 pF only.

This is pictured on Fig. 86 for the data collected in 2003 and 2004. On this figure, the increase is expressed as a percentage of the initial interstrip capacitance, around 0.67 pF for all baby detectors.

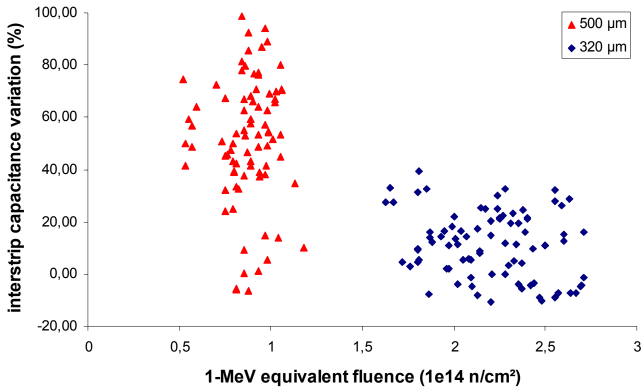

Fig. 86 : interstrip capacitance variation distribution as a function of the fluence.

The effect is further illustrated on the two graphs below. On these graphs, the curves coming from the bottom are the pre-irradiation ramps of the interstrip capacitances as a function of the bias voltage. Curves coming from above show the post-irradiation data. It is clear again that thick structures (on the right) present a higher increase. Furthermore, the end of the ramps are quite flat, suggesting that the saturation value of the interstrip capacitance is reached.

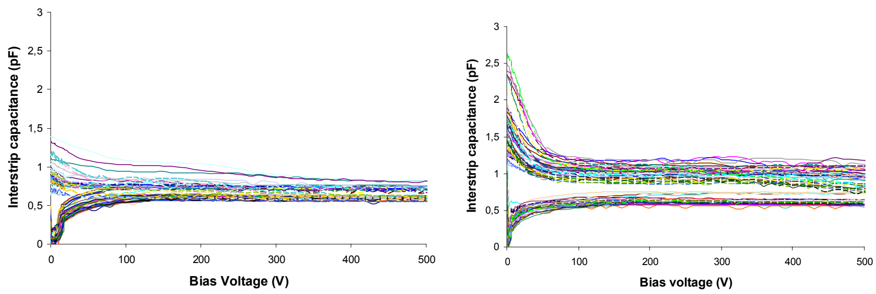

Fig. 87a, b : Interstrip capacitance as a function of the bias voltage for thin (left) and thick (right) structures.

However, as the value of the interstrip capacitance boasts a high dependence on the depletion status of the detector, it has then been decided to perform a few measurements up to very high voltages, in case of an hypothetic further decrease and despite the risk to generate an electrical breakdown on the device. A dedicated irradiation has been performed and the results were cross-checked in Louvain, Karlsruhe and Strasbourg.

The results and measurements before and after this special irradiation where all consistent among the different measurement setups. The above-mentioned effect has been observed on W6 (thick) structures produced both by HPK and STM, proving that it is vendor-independent. Surprisingly, a further decrease of the interstrip capacitance has been observed well above the depletion voltage (Fig. 88).

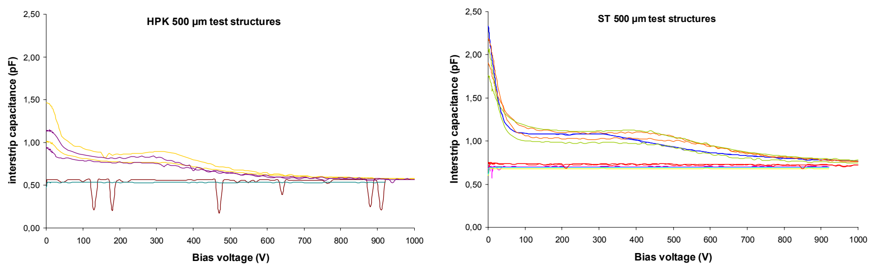

Fig. 88a, b : Interstrip capacitance measurements as a function of bias voltage for HPK (left) and ST (right) thick structures, up to 1000 V.

Strips scans also confirmed that the effect is uniform across a structure. It has therefore been concluded that this variation was linked to the geometry of the sensor, and especially its thickness.

No further investigations on this topic has been carried out. The qualification procedure remained unchanged, but it had been decided within the CMS sensor group to perform additional measurements on the thick structures showing an unusually high C_{int} at 400 V bias. A very interesting study would be to measure the impact of the increase of the interstrip capacitance to the crosstalk between adjacent strips of a complete module.

Conclusions

The large hadron collider will be a powerful tool for discovering new Physics provided the generated events can accurately be observed, but its harsh environment will be a major concern for the operation of large scale detectors. Since monocrystalline silicon microstrip detectors provide the required position accuracy, and as the RD48 collaboration developed a powerful empirical model to describe the evolution of their most critical properties, these detectors are a first class choice for the tracking at LHC.

The large scale of the experiments, their large number of channels and the vast amount of microstrip detectors needed to build the tracker oblige the collaborations to monitor the quality during the sensor production. Therefore, after a long R&D program aimed to the design of the detectors, the CMS collaboration set up a complete QA scheme. This program included, among other tests, radiation hardness tests to ensure a constant quality of the detectors. The radiation tests were dedicated to and focused on the evolution of macroscopic properties, comparing this evolution to the model developed by the RD48 collaboration.

In that scope, this work presents the efforts done in Louvain to assemble and calibrate the necessary equipment required to perform the electrical characterization on one hand, and the tools required for the irradiation of silicon microstrip sensors under an intense fast neutron flux on the other hand. The neutron beam was developed during the preceding years. Additional equipment and dosimetry methods were also developed and are presented as annexes of the document.

All the instruments and methods developed during the last few years give a valuable experience to the lab in various domains. In the different measurements required to characterize a silicon detector of course, but also in the dosimetry of the neutron beam; in the control of irradiation parameters; in post-irradiation thermal treatment or the handling of detectors in general.

The experimental measurements present different results. A side experiment that had to be made to confidently use the NIEL scaling hypothesis during the irradiation tests was the measurement of k-factors for neutrons above 20 MeV. Indeed, most of the fast neutrons of the Louvain-la-Neuve beam have energies above 20 MeV, but there is no experimental measurement of k-factors above that energy. Standard silicon diodes have therefore been irradiated with the UCL monoenergetic neutron beam at three different peak energies. The results of these irradiations show differences with the usual curve, but the large relative errors on the obtained factors do not allow to conclude for a significant deviation from the predictions.

The low gamma and charged particle contamination of the Louvain neutron beam allows the biasing of the detectors during irradiation. This is generally not the case with beams used for radiation hardness tests purposes. This is obviously due to the fact that charged particle beams lead to a very high charge carrier density within the bulk of the device during irradiation. This would lead to destructive currents if the device is biased at that moment. Hence, we studied the influence of bias during irradiation on a sample of devices. Our study shows that there is no evidence of the bias influence on the evolution of the macroscopic properties of silicon sensors.

However, part of this study unveiled a long term effect: the depletion voltage of a sensor seems to rise when biased for a long time, even at LHC operating temperature. Previously mentioned only once in the literature, a confirmation of this effect, its reproducibility and impact on the operation of a tracker module would be an interesting perspective and could be a concern.

The initial goal being to get involved in the CMS QA scheme, the major part of the irradiations were dedicated to the testing of the sensor production to monitor the evolution of their electrical properties in a standard way. The results gathered on more than 300 structures give a statistical basis to the validation of the Hamburg model coefficients used to predict the evolution of the depletion voltage and the leakage current of the sensors along their use in CMS. The study also showed that the other electrical properties do not significantly degrade at high fluences, the interstrip capacitance of thick sensors being the only parameters found to significantly evolve.

The interstrip capacitances of thick sensors have indeed shown to present a late saturation value at a bias voltage that is high above the depletion voltage of the detector. The interstrip capacitance-bias voltage curve shows a first plateau around the depletion voltage at a capacitance value higher than expected. This effect may have only little influence on the crosstalk between channels, but there are no detailed study about it to our knowledge. In addition, this effect could be studied as another interesting effect of radiation on the sensors: considering other coatings than SiO_2 for the surface of the sensors may lead to different surface defects, inducing another behaviour of the interstrip capacitance.

Annexes

A.1. Dosimetry and fluence calculations

The estimation of the fluence obtained with the different beams and the dose delivered to the silicon sensors during irradiation is, as discussed above, a crucial step in the radiation hardness tests. This part of the annexes describes the dosimetry methods and the other means used to determine these fluences, as well as their calibration.

A.1.1. Beam monitor

With the direct measurement and the integration of the deuteron current on the neutron production target, and with the help of the beam properties studied in [48], we perform the online monitoring and calculation of the attained fluence (Fig. 89).

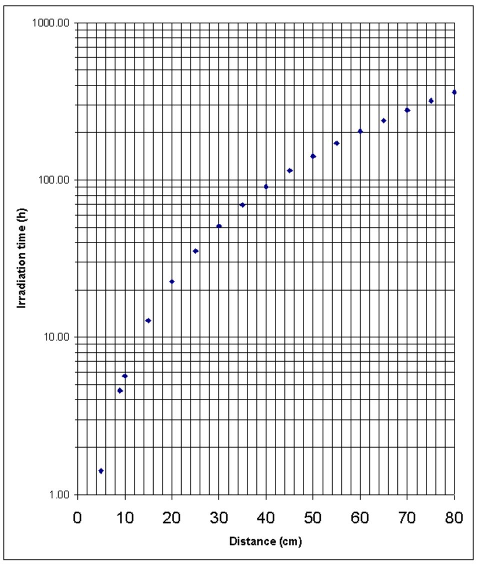

Fig. 89 : Time required to get 10^{14} n/cm^2 (not 1 MeV-equivalent) in the T2 neutron beam line with a deuteron current of 1 µA.

This monitoring is using lab-made floating current digitizers previously designed in the context of MSGC tests. These devices are built to measure currents as low as 10 nA, as high as 100 µA and are therefore well suited for this beam monitoring purpose. It is equipped with an analogue voltage output and a frequency output, both of these are well suited to our Keithley acquisition card and to a scaler installed in the same NIM crate as the current digitizer.

Before starting any silicon sensor irradiation test, we checked the current calibration of its outputs using a voltage source and a resistor. Knowing the value of the resistor with variable voltages, we know the current that should be read by the current digitizer.

The frequency calibration, counted by the attached scaler, gave a factor of 360870 counts/µAh. We are then able to obtain the calibration of our DAQ card readings, as shown in Fig. 90.

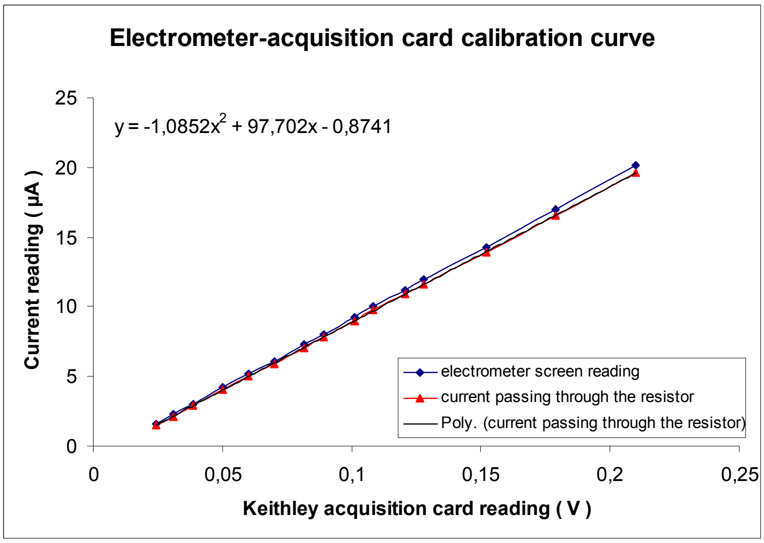

Fig. 90 : Keithley acquisition card and electrometer calibration curves.

This conversion has been incorporated in the irradiation-monitoring program in addition to the temperature readings and sensor power supply controls. It allows an online estimation of the fluence, complementary to the other post-irradiation dosimetry techniques described in the following paragraphs.

A.1.2. Activation

At the beginning of our sensor tests, we used activation foils to compute absolute neutrons fluxes at several different energies to check previous results on the neutron beam energy spectrum and confirmed the dosimetry results obtained either by the beam monitoring (see the above paragraph) or by the alanine system (cf. below).

Principle

The use of activation foils made of several different materials to determine the neutron spectrum in the T2 beam line has been discussed in a detailed way in [48] and another discussion can be found in the ASTM notice E720 [56]. We will therefore not go in such a detailed study here, but only remind its different steps.

The principle is to detect the gamma rays following the decay of radioisotopes produced during irradiation with neutrons.

At a given time T after the irradiation, the activity of a foil induced by the nuclear reaction "a" is given by:

$$A_a(T) = N_0 \overline{\sigma_a \phi}\left(1 - e^{-\lambda_a t_{irr}}\right)e^{-\lambda_a T} \qquad (\text{A.1})$$

Where N_0 is the number of atom of the relevant isotope in the foil (supposed to be uniformly irradiated), $\overline{\sigma_a \phi}$ is the reaction cross section integrated over the incident energy spectrum, λ_a the lifetime of the specific reaction product and t_{irr} the irradiation duration.

Knowing the incident neutron energy spectrum $d\Phi(E)/dE$, we compute an average cross section for a given reaction

$$\Phi_{tot} = \int_E \frac{d\Phi(E)}{dE} dE \qquad (\text{A.2})$$

$$\overline{\sigma_a} = \frac{\int_E \frac{d\Phi(E)}{dE} \sigma_a(E) dE}{\Phi_{tot}} \quad (\text{A.3})$$

Then, we make the following assumptions:

$$\overline{\sigma_a \phi} = \overline{\sigma_a} \phi_a \quad (\text{A.4})$$

ϕ_a being the neutron flux in he energy bin where σ_a is not negligible.

This allows us to use (A.1) and the activation foil activity to compute the total neutron flux in an energy range specific to the production of a given radionuclide (A.5).

$$\phi_a = \frac{A_a(T)}{N_0 \overline{\sigma_a} \left(1 - e^{-\lambda_a t_{irr}}\right) e^{-\lambda_a T}} \quad (\text{A.5})$$

In the case where the counting of the activity is made over a time lapse t_c and the number of counts is N_c, the experimental determination of the activity can be written as:

$$A_a^{\exp}(T) = \frac{N_c \lambda_a}{(1 - e^{-\lambda_a t_c})} \quad (\text{A.6})$$

This leads to the following expression of the fluence:

$$\Phi_a = \frac{N_c \lambda_a}{N_0 \overline{\sigma_a} \left(1 - e^{-\lambda_a t_{irr}}\right) e^{-\lambda_a T} \left(1 - e^{-\lambda_a t_c}\right)} \quad (\text{A.7})$$

In addition, the number of counts needed to get the experimental activity of the sample is corrected by the absolute detector efficiency (next paragraph) and dead time.

Calibration of the HPGE detector

A previous calibration of the HPGE detector has been carried out in [48] and repeated many times afterwards. It uses a well-known ^{152}Eu reference source. The results of the latest calibration, together with previous ones, are plotted above in Fig. 91.

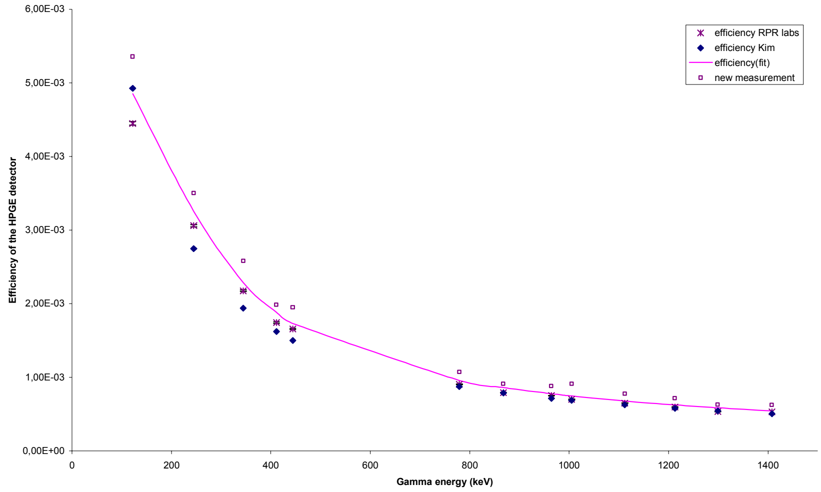

Fig. 91 : Efficiency of the Canberra HPGE detector.

Reactions considered

Using activation foils, one has always to consider several nuclear reactions with different thresholds to cover the full neutron energy spectrum. Table 23 gives an overview of the foils used here and the nuclear reactions involved.

Using Co foils, we could also use the $^{59}Co(n,\gamma)^{60}Co$ reaction, yielding gammas at 1173 and 1332 keV, but these do not allow multiple use of the activation foil due to the relatively long-lived ^{60}Co (5.27 y). On the other hand, the short-lived (1.5 d) $^{58}Ni(n,2n)^{57}Ni$ reaction is also unusable during our irradiation test.

Reaction	Incident neutron energy range (MeV)	Natural abundance of the initial isotope	γ energy (keV)	Gamma ray intensity	T ½ (days)
^{58}Ni(n,p)^{58}Co	2 – 20	0,683	811	0.995	70.916
^{59}Co(n,2n)^{58}Co	14 – 50	1	811	0.995	70.916
^{59}Co(n,3n)^{57}Co	> 20	1	122	0.855	271.77
^{93}Nb(n,2n)^{92m}Nb	9 – 30	1	934	0.991	10.15

Table 23 : Reactions of interest in the T2 beam line activation measurements.

Results

This method gave results consistent with the energy ranges of the 4 different reactions.

As an example, for a fluence estimated to 1.1 10^{14} n.cm^2 by the beam monitoring:

- the Nb(n,2n) reaction gave 10^{14} n/cm^2 (covering almost the whole energy spectrum) ;
- the Ni reaction gave 4.2 10^{13} n/cm^2 (covering almost the first half of the spectrum) whereas the Co(n,3n) reaction, its complementary, gave 7,32 10^{13} n/cm^2 for the high energy part.

A.1.3. Alanine

In addition to the evaluation of the fluence, we used individual dosimeters for each silicon sensor or test structure. The reason is twofold: first, we wanted to detect any beam misalignment of the sensors and second, because the beam distribution is not uniform across its spot.

An individual dosimetry system does help to disentangle huge fluence discrepancies due to any stack misalignment: it is not detectable with the beam monitoring alone. It also helps to take the beam radial dose distribution into account.

Considering the different dosimetry systems readily available, alanine seemed to be one of the most efficient one:

- Films are easy to handle but pellets can also be considered using the same reader.

- The dose range is wide (from 10 Gy up to 500 kGy with our films), making it suitable for other intense radiation fields.

- As alanine dosimetry is based on the generation of free radicals within the film by radiation*, there is little fading [57] in contrast to e.g. thermoluminescent dosimeters (an introduction can be found e.g. in [1]). We can therefore keep track of the doses by storing the dosimeters and can re-measure these ones in case it is needed.

- Although alanine is mainly used for Gamma ray induced dose measurements, it is also sensitive to neutrons (see e.g. [58]) and protons or other charged particles. In this case, one needs to know the Relative Effectiveness** (R.E.) of alanine for the considered radiation. It then allows cross checks between laboratories using different beams.

One important characteristic to be mentioned is that its response to the radiations varies with the ambient temperature during exposure. This can easily be taken into account in our case as the Bruker E-scan reader (Fig. 92) includes automatic correction of the readings.

The disadvantage of alanine is that, as previously mentioned, it is mainly used for gamma-ray dosimetry (and especially ^{60}Co, one of the most common high intensity gamma ray source). The dose read by our commercial system after neutron exposure may therefore differ from the tissue-equivalent neutron dose, and the fluence-to-dose factor may also vary between dosimetry systems.

---

* Alanine dosimetry is based on the quantification of these free radicals by detection of their free electrons using Electron Paramagnetic Resonance (EPR).

** The Relative Effectiveness (R.E.) is defined as the ratio of dosimeter signal after equal doses of considered radiation and reference radiation, usually ^{60}Co (for which our system is designed).

Fig. 92 : The Bruker E-scan alanine reader.

Study of a fluence-to-dose conversion factor

Using the beam monitoring, we computed the fluence-to-dose conversion factor for Kodak BioMax dosimeters irradiated in our high flux neutron beam. We checked how this conversion factor compares with the few references either found in data compilations on dosimetry systems or starting back with the corresponding KERMA coefficients.

To determine our experimental factor, we placed several dosimeters right in the center of the beam, at a distance larger than 50 cm from the production target to ensure a uniform irradiation. The beam fluence has been determined using the beam profile as described in section A.1.1. The obtained conversion factor is of 4.51 fGy.m^2, with a standard deviation of 9.8 %, in good agreement with the errors on the computation of the fluence.

Given this experimental factor, we compare it to the computations of response factors obtained using the T2 beam line energy spectrum (as described in [48]) folded with the alanine response function (Fig. 93, taken from Tavlet et Al in ref. [59]) using (A.8).

$$resp_{beam} = \frac{\int_E \frac{d\Phi(E)}{dE} resp(E) dE}{\int_E \frac{d\Phi(E)}{dE} dE} = \frac{\int_E \frac{d\Phi(E)}{dE} resp(E) dE}{\Phi_{tot}} \qquad (A.8)$$

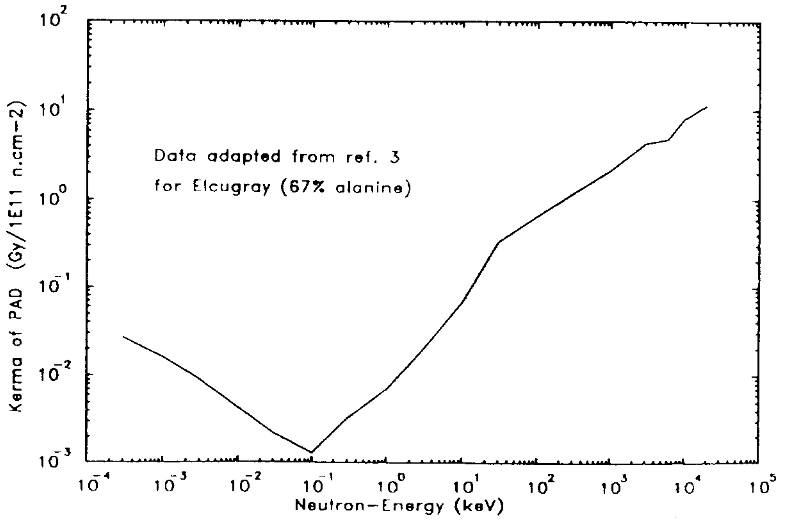

Fig. 93 : Response of PAD-Elcugray to neutrons as taken from [59].

This second method gave a fluence-to-dose conversion factor of 4.06 fGy.m^2.

In a similar way, one can fold the neutron spectrum to the KERMA coefficients determined by Chadwick et al. [60] and experimentally corrected by Meulders et al. [61]. In the latter case, we start by computing the neutron KERMA at the relevant energies using the alanine chemical formula ($C_3H_7NO_2$) and then fold it with the neutron energy spectrum and the relative effectiveness (R.E.) of alanine in a way similar to (A.8).

The R.E. of alanine can be found e.g. in Waligorski et al. [62], or Gertsenberg et al. [63]. The R.E. quoted in the latter (pictured in Fig. 94) are closer to the 0.36-0.7 range mentioned by Schraube et al [64].

The results are summarized in Table 24, where the third column shows factors computed using the Waligorski R.E. whereas the fifth uses the Gertsenberg spectrum.

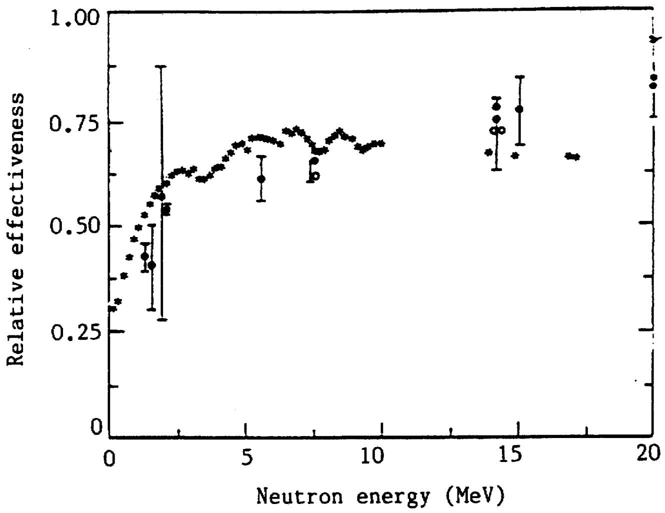

Fig. 94 : Alanine relative effectiveness to neutrons taken from [63].

	KERMA ($fGy.m^2$)	R.E. (Wal.)	Alanine response ($fGy.m^2$)	R.E. (Gert.)	Alanine response ($fGy.m^2$)
Chadwick	6.14	0.75	4.61	0.7	4.29
Meulders & Chadwick	6.16	0.75	4.62	0.7	4.31
Average	6.13	/	4.61	/	4.3

Table 24 : Alanine fluence-to-dose conversion factors obtained using literature (cf. [60], [61], [62] and [63]).

We conclude that our value of 4.51 ± 0.44 $fGy.m^2$ for the fluence-to-dose conversion factor for Kodak BioMax dosimeters shows a good agreement with computations based on existing literature. Although we have no indication of their exact chemical composition, the second method, starting with the KERMA, gives results that are closer to our experimental factor.

However, with respect to R.E. factors quoted in the literature, our measurements are not accurate enough to confirm either results obtained by Waligorski [62] or those quoted by Gertsenberg [63] or Schraube [64].

Despite the fact that the factor computed using the M. Tavlet data differs more from our experimental result, both methods are, in our case, complementary as we do not have the detailed chemical composition of our Kodak Biomax dosimeters*. In fact, the alanine response to neutrons depends on the binder used to make the dosimeters: on its alanine/paraffin ratio in case paraffin is used as a cement for alanine powder (the KERMA of neutrons into the material changes, as discussed in [64]), and one can therefore easily introduce uncertainties.

Remarks on the alanine response to protons

In collaboration with colleagues of the CMS silicon sensor group in Karlsruhe, we asked them to irradiate some of our alanine films with their 24 MeV proton beam.

The dose readings are, of course, much more important with respect to the fluences as we deal here with charged particles. Assuming the R.E. of alanine is 1 for protons above 15 MeV [62] and a radiation effectiveness weighting factor of 5 (cf. G. F. Knoll, [1]), the particle data group [65] gives a fluence-to-dose conversion factor about 46 fGy.m^2 for 50 MeV protons.

Only two dosimeters irradiated gave a consistent experimental factor obtained, of 67.4 fGy.m^2. This result is plotted together with PDG data in Fig. 95. Two other dosimeters gave factors even bigger than 100 fGy.m^2.

* We only know the strip on which the dosimeter is glued is made of PET ($C_{10}H_{10}O_4$)

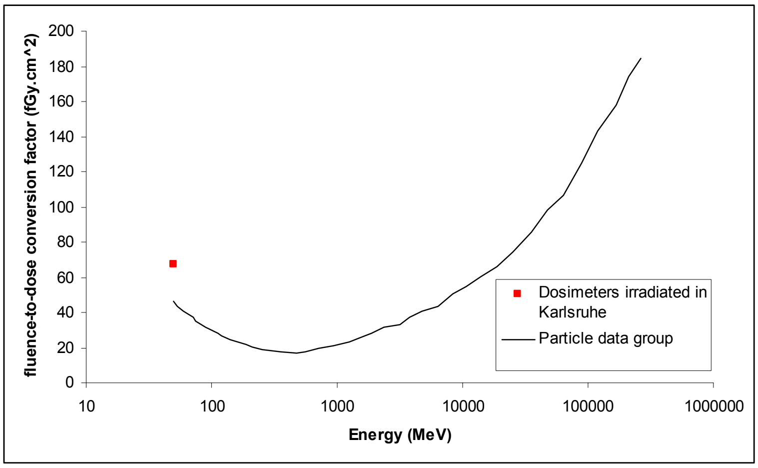

Fig. 95 : Alanine fluence-to-dose conversion factors for protons.

As our experimental factor is pretty different to the quoted ones, and since there are big differences with some other dosimeter readings, further investigations on this topic have to be envisaged.

A possible way to explain the difference is the dose rate encountered by these dosimeters during irradiation: as mentioned in the ASTM notice on alanine [66], the dose rate for alanine in a continuous radiation field has to be lower than 100 Gy/s, and our dosimeters get their full dose (more than 80 kGy) in less than 365 s. This leads to a minimum dose rate of 220 Gy/s, twice the recommended maximum one.

Within this scope, further information on the alanine response to protons can be found in references [67] through [70].

Remark on encountered problem with our Bruker E-scan

From time to time, we have an error message from the alanine readout system during the instrument check, right before any measurement: “Error 112 – frequency out of range: samples removed?”.

This message may appear when the sample holder is not in place, or its positioning is bad. Here however, it seems the problem arises is due to important temperature changes in the lab: the resonant frequency of the apparatus is affected and gets offset by a few kHz out of the allowed limit given by the previous calibration.

Although we monitored the temperature for several weeks during summer and winter and didn't observe the problem again as the temperature drops or increases, this error message can still happen, and we feel important to write here the way to fix it and keep the system running.

The solution to this problem is in fact to recalibrate the system. This requires the readings of NIST-traceable dosimeters if you want not to loose the system absolute calibration and can be annoying if your dosimeter set has been unused for several months because of the small fading they have anyway.

To avoid either to buy new calibrated dosimeters or to risk loosing the system calibration, one has to run the calibrate.vbs script again, but only perform an instrument check. Thereafter, select the "modify an existing calibration" option, load the existing one and perform the fitting again.

In this way, the routine merely establishes the reference values for the instrument self check but will not affect the performance of the instrument or change the alanine calibration curve.

A.2. Thermal treatment of the sensors: annealing oven

Many times, we stressed out the annealing-dependent time evolution of the properties of our silicon devices. This has particularly been emphasised for leakage currents or depletion voltages.

Therefore, any radiation-related study of silicon diode or sensor properties requires a good control of the device's annealing state. This can only be done using an oven with high temperature stability, which also doesn't vary too much during openings for structure introduction and/or removal.

As any commercial oven is an expensive piece of equipment, we designed a dedicated small oven (pictured in Fig. 96) whose characteristics are described below.

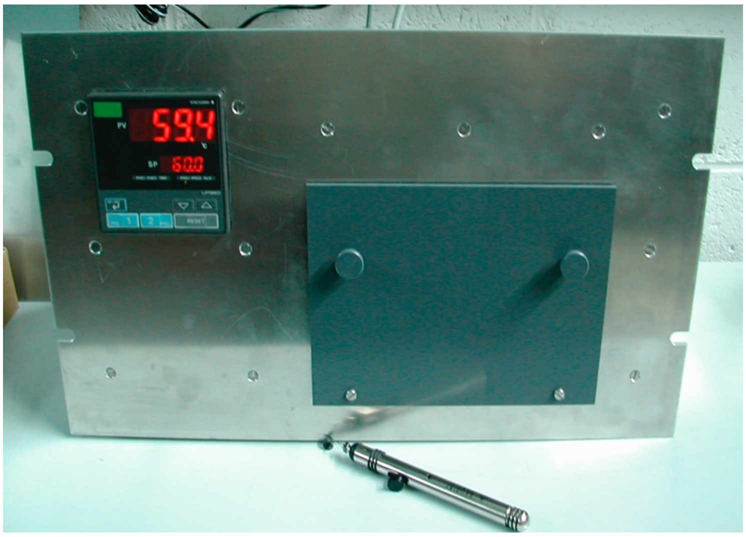

Fig. 96 : Annealing oven.

A.2.1. Principle

The most important characteristic of an oven for silicon annealing is the temperature stability. It does not require having a fast response time since the heat treatments are made at constant temperatures and because it is much easier to put the structures inside and remove these when the required annealing time is reached.

Ensuring a good temperature stability means that the oven specific heat must be high, the air volume is kept as small as possible and, of course, the thermal insulation is as good as achievable.

We choose to use special insulating bricks to ensure the first and the latter criteria. This solution had proven to be efficient with a previously built oven for TLD-annealing. A dedicated kitchen jolt resistor, directly connected to the mains using a power relay, ensures the heating of these heavy bricks.

The temperature regulation is made by a Yokogawa UP-350 programmable controller [71]. This is a very simple way to control the temperature since these modules are equipped for reading of Pt100. They provide a display showing the temperature setting and the measured current temperature. Electrical connections (cf. sketch on Fig. 97) are also easy to make and the auto-tune functionality quickly makes the oven operational in the best conditions.

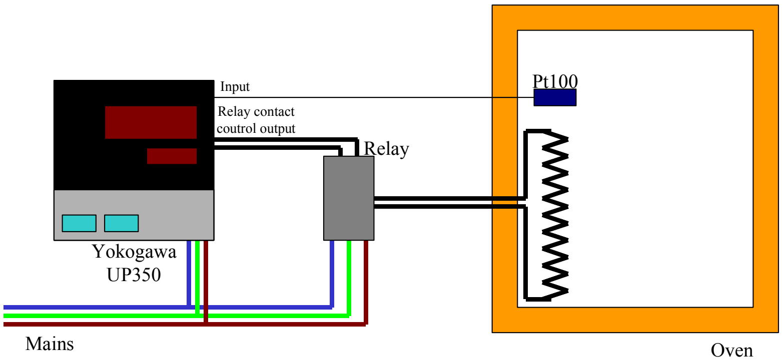

Fig. 97 : Annealing oven working principle.

The temperature uniformity is ensured by the fact that the heating resistor is in fact tied on the outer part of a steel enclosure (not shown on Fig. 97). This gives a very uniform heating inside the oven, at the position of the Pt100 sensor and where we perform the actual heat treatments. The design of the oven allows the heat treatment of either 6 standard CMS structures or 2 full-sized sensors.

A.2.2. Performances

The performances of the oven have been measured using a separate Pt100 read by a HP34970a data acquisition/switch unit.

Different tests have been carried out:

1. A maximum temperature test
2. A heating speed and stability test over more than 40 hours and for 2 different temperature settings (50 °C and 60 °C)
3. A temperature uniformity test over the 2 plateaus of the oven

The oven proved to hold temperatures up to 200 °C. Higher temperatures are possible with the replacement of the cabling for the Pt100 sensor.

On the other hand, the average heating speed from ambient to 50-60 °C appeared to be of 4 °C/min. This heating speed is practical, as one needs only 10 minutes to get the oven ready for annealing. The fluctuations of the temperature with time are about 0.3 °C on average with maximal deviations less than 2 °C. This test is illustrated on Fig. 98, where one clearly sees the oven stability in the 60 °C plateau.

Another parameter of importance is the temperature variation in the oven during openings (e.g.: at the beginning of the annealing). It can of course not be deduced from measurement shown on Fig. 98, because the opening of the oven remained closed during the entire test. Anyway, with the oven stabilised at 60 °C, opening the door during 1 min causes a drop of the temperature down to 57 °C, which is recovered in less than 2 min when the oven is closed again. If one leaves the oven open for a longer time (5 min), the regulation system will work in order to stabilize it at the nominal temperature setting, but this will result in a small overheating as the oven is closed again.

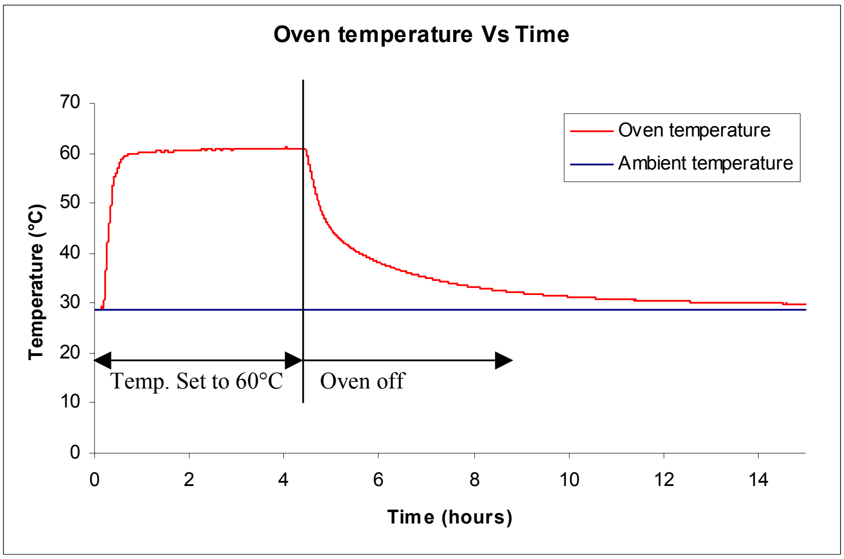

Fig. 98 : Temperature stability test at 60 °C (standard annealing temperature).

About the uniformity test, we placed Pt100 sensors at 12 different places on the 2 plates of the oven (6 on each, in 2 rows of 3 spots). The temperature deviation between the different measurements did not exceed 0.7 °C, proving the temperature is uniform enough.

A.3. Useful constants

A.3.1. Silicon properties

Gap (eV)	1.12
Gap variation as a function of temperature (eV/K)	$-2.30\ 10^{-4}$
Density of states in the conduction band - Nc ($1/cm^3$)	$2.8\text{-}3.22\ 10^{19}$
Density of states in the valence band - Nd ($1/cm^3$)	$1.04\text{-}1.83\ 10^{19}$
Electro affinity (eV)	4.05-4.85
Intrinsic charge carrier concentration ($1/cm^3$)	$1.02\text{-}1.4510^{10}$
Electron-hole pair creation mean energy (eV)	3.63
Fano factor	0.115
Intrinsic resistivity (Ω.cm)	$230\ 10^3$
Dielectric constant	11.9
Electron mobility μ_n ($cm^2/V.s$)	1450
Hole mobility μ_p ($cm^2/V.s$)	505
Electron saturation velocity $v_{s,n}$ (cm/s)	10^7
Hole saturation velocity $v_{s,p}$ (cm/s)	$8.4\ 10^6$
Breakdown voltage (V/cm)	$\sim 3\ 10^5$

Table 25 : Electrical properties of silicon crystal (at 300 K).

Structure	Diamond
Lattice (Angström)	5.431
Atomic number	14
Mean atomic mass	28.09
Density (g/cm^3)	2.329
Thermal expansion coefficient (1/K)	$2.56\ 10^{-6}$
Thermal conductivity (W/m.K)	1.53
Refraction index	3.42
Fusion temperature (°C)	1392-1415
Radiation length (cm) (g/cm^2)	9.36 21.82

Table 26 : Physical properties of Silicon

A.3.2. Silicon oxide properties (SiO_2)

Structure	Amorphous
Resistivity (Ω.cm)	10^{14}-10^{16}
Density (g/cm^3)	2.27
Dielectric constant	3.84
Breakdown voltage (V/cm)	$5\ 10^{6}$-$8\ 10^{6}$
Gap (eV)	8.8
Thermal expansion coefficient (1/K)	$5\ 10^{-7}$
Thermal conductivity (W/m.K)	0.014
Refraction index	1.46
Radiation length (cm) (g/cm^2)	10.2 27.05

Table 27 : Silicon oxide properties

Terms, abbreviations

Usual notations and sensor-related abbreviations:

C_{back}	The backplane or bulk capacitance of the sensor. It is measured between the bias ring and the backplane.
q	The proton charge, 1.6 10^{-19} C.
ε	The relative dielectric constant of the medium (no units).
ε_0	The permittivity in vacuum, in Farads per unit length.
d	The depletion zone thickness, in units of length. Sometimes confounded with the detector thickness in some equations where the sensor is depleted.
N_{eff}	The effective doping concentration of the semiconductor, in particle per unit volume. It is the difference between the donor and acceptor concentrations.
V_{bi}	The built-in voltage of a PN junction. It is the resulting electrical potential across the junction when no bias is applied. It results from the diffusion of electrons and holes.
V, V_{bias}	Usually, the reverse voltage applied on the PN junction, diode or microstrip sensor.
V_{dep}	The full depletion voltage of a device, it is reached as the depletion zone thickness is equal to the thickness of the sensor.
J_{leak}	The leakage current surface density of a reverse-biased device.
I_{leak}	The leakage current of a reverse-biased device.
d_{bi}	The thickness of the built-in depletion zone
n_i	The intrinsic carrier concentration, per unit volume.
τ_g	The minority carrier generation lifetime.
p	The pitch between two strips of a microstrip sensor.
w	The width of the p+ implantation of a strip.
Φ_{eq}	The 1-MeV equivalent fluence, as determined using the NIEL hypothesis (in particle per unit surface).
α	The total leakage current of a device, divided by the volume of the junction and the 1-MeV equivalent fluence. In principle it is independent of the bulk type.

t_a The annealing time.

T_a The annealing temperature.

r In equations related to the Hamburg Model, it is the donor removal constant (in fraction of the initial effective doping concentration).

g_c The stable damage introduction rate (per unit fluence and volume).

g_a The beneficial annealing defect introduction rate (per unit fluence and volume).

τ_a The beneficial annealing time constant. As it is highly temperature-dependent, it is often accompanied by a temperature indication.

g_y The reverse annealing defect introduction rate (per unit fluence and volume).

τ_y The reverse annealing time constant. As it is highly temperature-dependent, it is often accompanied by a temperature indication.

C_{ac} The coupling capacitance of a strip. it is measured between the DC pad (contact with the bias resistor and the p^+ implant) and AC pad (readout) of the strip.

R_{poly} The bias resistor.

C_{int} The interstrip capacitance. It is measured in between two adjacent strips.

R_{int} The interstrip resistance. It is measured in between two adjacent strips.

R_{p+} This is the measurement of the p^+ implant resistivity, in Ohm/cm, it is in fact a measurement of the doping concentration of the implant.

R_{Al} It is the value of the resistivity of the aluminization layer, in Ohm/cm².

I_{diel} The leakage current that passes trough the dielectric of an AC-coupled strip.

I_{strip} The bulk-generated leakage current passing trough a given strip to the bias ring. In principle, it should correspond to the total leakage current of the detector, divided by the number of strips.

κ the hardness factor of a beam or a particle at a given energy. It is the ratio between the 1-MeV equivalent fluence and the real fluence in the NIEL hypothesis.

Text abbreviations and some useful terms :

APV Analogue Pipeline Voltage, it is the front-end chip that keeps the bunch readouts, waiting for the level 1 trigger information in order to further keep the information or delete it.

CCU The Control Clock Unit distributes the bunch synchronisation information.

CV Capacitance-Voltage. The measurement of the bulk capacitance of a sensor as a function of the reverse bias voltage, useful to determine the full depletion voltage of a sensor.

DLTS Deep Level Transient Spectroscopy. This technique is useful for determining the type of defects induced in the bulk at the microscopic level. The very basic principle is to inject charge into the bulk in order to fill all traps. The measurement of the subsequent voltage or current transients following an abrupt change in the applied bias voltage are detected and analysed. This technique has the disadvantage that defect concentrations have to be kept low in order to not saturate the signal.

ECAL Electromagnetic Calorimeter

FEC Front End Controller, the module control electronic device.

FED Front End Driver, the module readout device

Float zone The float zone technique for growing silicon ingots uses. To get a detector-grade silicon ingot, a high-purity polycrystalline rod is re-melted into a monocristal ingot by being driven trough a RF coil. The RF coil is used to heat the rod locally and molten a “zone” of it. Hence the name. This technique performs also a simultaneous purification the crystal. Float zone (FZ) silicon presenting a low-level of impurity is often referred as standard Float zone (STFZ), whereas oxygen-doped silicon is mostly referred as diffusion-oxygenated float zone (DOFZ). Oxygenated float zone has shown an improved radiation-hardness to charged particle fluences.

Fluence The fluence (in $1/cm^2$) is the total integrated particle flux over a given period.

Frenkel Frenkel pairs are the most basic microscopic defects. It consist of a vacancy (V) –interstitial (I) pair, created together by the kick-out of a lattice atom out of its initial position.

GPIB The GPIB (general purpose interface bus) was specifically designed to connect computers, peripherals and laboratory instruments so that data and control information could pass between them. It is also known as IEEE-488 or HPIB and is the communication protocol we used to control the electrical characterization setup. It is faster than RS-232 and allow daisy-chaining of the instruments

HCAL Hadronic calorimeter

HIP Heavily Ionizing Particle: this kind of events present a very large ionizing energy deposition on a sensor. This kind of deposition can saturate the readout electronics and in fact acts like a “pinhole” (breakdown of the coupling capacitance dielectric).

HPK Hamamatsu Photonics company, one of the CMS silicon microstrip sensors manufacturer.

IQC Irradiation Qualification Center. The Louvain and Karlsruhe centres in charge of the routine irradiations for radiation hardness testing of the sensor production.

IV Current-voltage. It is the measurement of a sensor’s leakage current as a function of the reverse bias voltage.

LCR The abbreviation for a device able to measure inductance (L), capacitance (C) or resistance (R). This kind of equipment measures in fact the impedance of an electrical circuit at a given frequency and is thereafter able to assess the different components at the origin of the impedance.

LHC Large Hadron Collider.

MOS Metal Oxide Semiconductor device. This device , like its name suggests it, is made of a semincondutor bulk on top of which are stacked an oxide layer and a conductive layer (metal). It is characterized mainly by two working regime: depletion and accumulation. In the first regime, the semiconductor bulk is depleted (reverse-biased) and in the other, it is forward-biased and hence charge carriers accumulate at the oxide. The voltage at which the transition between the two modes occur is determined by the oxide quality: the less trapped charges, the closer to zero is this transition voltage.

MSSM The Mimimal Supersymmetric extension of the Standard Model is one of the model proposed as extension of the standard model. It assumes the existence of three neutral Higgses (A^0, H^0 and h^0) and two charged Higgses (H^+ and H^-).

NIEL Non-ionizong Energy Loss. It is the part of the energy deposition within a semiconductor device that is though to be at the origin of permanent damage in the device. The NIEL hypothesis assumes that the variation of the bulk electrical properties of a semiconductor device scales with this energy deposition.

Oxygenated Cf. float zone

PET The polyethylene used to make the support strip for our alanine dosimeters. It is widely used as material for plastic bottles.

PKA Primary Knock on Atom: it is the initial collision that removed a lattice atom from its position.

PQC Process Qualification Center. These centres, member of the silicon sensor group of the CMS Tracker collaboration performed measurements on test structures that were foreseen to monitor the consistency of the production quality of the sensors, by e.g. measuring the quality of the aluminium deposition.

PSI Paul Scherrer Institute.

QTC Quality Test Center. These centres, member of the silicon sensor group of the CMS Tracker collaboration performed measurements on the full-sized sensors in order to monitor the possible defects.

Rd48, ROSE

The so-called ROSE (Research and development On Silicon detectors for future Experiments) collaboration, now over, is one of the most fruitful collaboration about the radiation hardness of silicon sensors. It yields, for instance, the well known Hamburg model for the evolution of the effective doping concentration.

R.E. Relative effectiveness. It is a factor used to scale the response of dosimeter in a given radiation field.

SEE-SEU-SEL

Single Event Effects (SEE) are due toi the crossing of the detector by a single particle. These effects are classified according to their permanency into Dingle Event Upset (SEU) and Single Event Latchup (SEL).

A SEU is a soft, non-destructive error. Resetting the device affected ensures that it operates again in a normal way. Typical examples are pulses in analogic circuits or bit flips in digital devices.

A SEL causes a loss of device functionality. It is a hard error that potentially causes permanent damage. A typical example is the creation of high leakage channels resulting in currents above the device specifications.

ST ST microelectronics was the second provider of silicon sensors for CMS. It has been dismissed due to production problems.

Standard deviation

For a given set of measurements of average value μ, the standard deviation is given by the following expression:

$$\sigma = \sqrt{V} = \sqrt{\frac{\sum_{i=1}^{N}(x_i - \mu)^2}{N}}$$

Where V is called the Variance of the sample

Standard silicon Cf. Float zone

TEC Tracker EndCap. It is the forward parts of the tracker, where devices are arranged in wheels perpendicular to the beampipe.

TIB Tracker Inner Barrel. It is the inner part of the tracker, where 320 µm thick sensors are arranged in rods and facing the beampipe.

TOB Tracker Outer Barrel. It is the outer part of the tracker, where 500 µm thick sensors are arranged in rods and facing the beampipe.

TSC Thermally Stimulated Current. Like DLTS, it is a technique for investigating the microscopic defects induced in a silicon sensor. It has the advantage on DLTS that the defect concentration does not have to be low. The basic principle is to first cool down the sensor under reverse bias(or zero bias, depending on the measurement). Once cooled, charges are injected in the bulk trough forward bias or illumination. Thereafter, the device is heated at a constant temperature variation rate. Leakage current is monitored during the whole procedure and its variation with temperature is used to determine the levels and concentration of defects.

Bibliography

[1] “Radiation detection and measurement, third edition”, G.F. Knoll, John Wiley & Sons, 1999.

[2] “Semiconductor radiation detectors – device physics”, G. Lutz, Springer-Verlag, 1999.

[3] “The particle detector briefbook”, R.K. Bock & A. Vasilescu, Springer-Verlag, 1998.

[4] “Physics of semiconductor devices, second edition”, S.M. Sze, John Wiley & Sons, 1981.

[5] “Radiation hardness of silicon detectors – a challenge from High-Energy Physics”, G. Lindström et al, Nucl. Instr. Meth. A vol. 426 (1-15), 1999.

[6] “Higgs coupling at the LHC”,D. Zeppenfeld, HEP/PH0203123v1, 2006.

[7] “Physics at LHC”, G. Wrochna, CMS CR 2002-015, CERN, 2002.

[8] “CMS Physics overview”, C.-E. Wulz, CMS CR 2001-016, CERN, 2001.

[9] “Atlas detector and Physics performance, technical design report volume II”, The Atlas Collaboration, CERN/LHCC 99-15, 1999.

[10] “Direct collider signatures of large extra-dimensions”, I. Antoniadis et al., HEP-PH/9905311, 1999.

[11] “Indirect collider signals for extra-dimensions”, J. L. Hewett, Phys. Rev. Let. 82-124, 1999.

[12] “CMS trigger strategies for the selection of MSSM Higgs boson using electron-tau decay modes”, O. van der Aa, PhD thesis, UCL, 2005.

[13] The CMS letter of intent

[14] “The alignment system of the CMS tracker”, A. Ostaptchouk et al, 2001.

[15] “The tracker project technical design report”, the CMS collaboration, CERN/LHCC 98-6, 1998.

[16] “The tracker project technical design report addendum”, the CMS collaboration, CERN/LHCC 2000-016, 2000.

[17] “Layout and performance of the CMS silicon strip tracker”, D. Abbaneo, CMS CR 2003/032, 2003.

[18] “Radiation and temperature effects on the APV25 readout chip for the CMS tracker”, E. Noah, PhD thesis, Imperial College of London, 2002.

[19] “CMS inner tracking”,M. Manelli, Eur; Phys. J. C vol. 34, 2004.

[20] “Sensor alignment by tracks”, V. Karimäki et al., CMS CR 2003-022, 2003.

[21] "R&D for the CMS silicon tracker", L. Feld, presentation shown on 15/01/1999 at CERN.

[22] “Notes on fluence normalisation based on the NIEL scaling hypothesis”, A. Vasilescu & G. Lindström, ROSE/TN/2000/02, 2000.

[23] “Highly ionising events in silicon detectors”, M. Huhtinen, CMS NOTE 2002-011, CERN, 2002.

[24] “The effect of highly ionising particles on the CMS silicon strip tracker”, L. Mirabito et al., CMS NOTE 2004-011, CERN, 2004.

[25] “The NIEL hypothesis applied to neutron spectra of irradiation facilities and in the ATLAS and CMS SCT”, A. Vasilescu, ROSE/TN/97-2, revised in December 1999.

[26] “Capacitances in silicon microstrip detectors”, E. Barberis et al., Nucl. Instr. Meth. A vol. 342 (90-95), 1994.

[27] "Influence of the geometrical layout of the silicon microstrip detectors on electrical characteristics", T. Angelescu et al, EPPG/PHYS 38, 1998.

[28] "Les senseurs silicium pour CMS: caractérisation et mise en oeuvre des tests de résistance aux rayonnements", E. Forton, unpublished DEA report, 2001.

[29] "Nuclear electronics", E. Kowalski,Springer-Verlag, 1970.

[30] " Low noise techniques in detectors", V. Radeka, Ann. Rev. Nucl. Part. Sci. vo; 38 (217-277), 1988.

[31] "The impact of high-energy proton irradiation on the low frequency $1/f$ noise in FZ-silicon diodes", E. Simoen, C. Claeys, Mat. Sc. in Semic. Processing vol. 3, 2000.

[32] "Radiation damage in silicon detectors – microscopic defects and macroscopic properties", M. Moll, DESY-THESIS-1999-040, 1999.

[33] "Investigation of design parameters and choice of substrate resistivity and crystal orientation for the CMS silicon microstrip detector", S. Braibant et al, CMS note 2000/011.

[34] "Time development and flux dependence of neutron-irradiation induced defects in siliconpad detectors", D. Zontar et al., Nucl. Instr. Meth. A vol. 426, 1999.

[35] "Bias-dependent radiation damage in high-resistivity silicon diodes irradiated with heavy charged particles", V. Cindro et al, preprint, 1999.

[36] "Bias-dependent annealing of radiation damage in neutron-irradiated silicon p+ - n - n+ diodes", V. Cindro et al, Nucl. Instr. Meth. A vol. 419, 1998.

[37] "Bias dependence and bistability of radiation effects insilicon" , M. Mikuz et al, Nucl. Instr. Meth. A vol. 466, 2001.

[38] "Optimization of the silicon sensors for the CMS tracker", S. Albergo et al., Nucl. Instr. Meth. A vol. 466 (300-307), 2001.

[39] "Comprehensive study on theeffects of irradiation on charge collection efficiency in silicon detectors", L. Borello et al. , Nucl. Instr. Meth. A vol. 461 (178-181), 2001.

[40] "Simulation of non-ionising energy loss and defect formation in silicon", M. Huhtinen, ROSE/TN/2001-02, CERN, 2001.

[41] "Neutron displacement cross-sections for structural materials below 800 MeV", A. Yu Konobeyev et al. , Journal of nuclear Physics vol. 186 (117-130), 1992.

[42] "Displacement damage in silicon", A. Vasilescu & G. Lindström, on-line compilation available at http://sesam.desy.de/~gunnar/Si-dfuncs.

[43] "Observation of a bistable defect generated and activated by heat treatments in irradiated high resistivity silicon detectors", M. Moll et al., Nuclear Physcics B (proc. suppl.) vol. 44 (468-474), 1995.

[44] "Results since last workshop", A. Furgeri, private communication at the "2nd IQC workshop" held in Louvain-la-Neuve in May 2003.

[45] "The silicon sensors for the Compact Muon Solenoid tracker – design and qualification procedure", J.-L. Agram et al, Nucl. Instr. Meth. A vol. 517 (77-93), 2004.

[46] "Specifications for the Quality Control & Assurance of the CMS Silicon Sensors", the CMS Tracker sensor Working Group, unpublished, 2000.

[47] "Sensors and modules under mechanical stress", F. Hartmann, presentation at the "STM mini-workshop", CERN, December 2003.

[48] "Etude du comportement de détecteurs gazeux à micro-pistes MSGC sous irradiation intense de neutrons rapides ", K. Bernier, PhD thesis, UCL, 2001.

[49] "An intense fast neutron beam in Louvain-la-Neuve", K. Bernier et al, available on the web at http://www.fynu.ucl.ac.be/themes/he/cms/neutron_beam/neutrons-beam.html .

[50] Yokogawa UP14 manual

[51] "Radiation damage in silicon detectors – an introduction for non-specialists", M. Moll, CERN EP-TA1-SD seminar 14/02/2002, transparencies available on the web.

[52] "Results on radiation hardness of silicon strip detectors up to neutron fluences of 10^15 n/cm2", R. Wunstorf & M. Benkert, Nucl. Instr. Meth. A vol. 315, 1992.

[53] "Experimental cross sections for light-charged particle production induced by neutrons with energies between 25 and 65 MeV incident on oxygen", S. Benck et al, Atomic data and nuclear data tables 72 (1-20), 1999.

[54] "Quasi-monoenergetic neutron beams with energies from 25 to 70 MeV", H. Schuhmacher et al, Nucl. Instr. Meth. A vol. 421 (284-295), 1999.

[55] Private discussion with G. Lindström about the monoenergetic neutron beam test.

[56] "Standard guide for selection and use of neutrons sensors for determining neutron spectra employed in radiation hardness testing of electronics", ASTM note E 720-02.

[57] "Dosimetry by ESR spectroscopy of alanine", D.F.Regulla & U. Deffner, Int; J. Appl. Radiat. Isot. vol.33 (1101-1114), 1982.

[58] "Intercomparison of gamma ray, X ray, and fast neutron dosimetry using alanine detectors", J.W. Hansen et al, Rad. Prot. Dosimetry vol. 27 N°2 (85-92), 1989.

[59] "Data compilation of dosimetry methods and radiation sources for material testing", M. Tavlet et al, CERN/TIS-CFM/IR/93-03, 1993.

[60] "A consistent set of neutron kerma coefficients from thermal to 150 MeV for biologically important materials", M.B. Chadwick et al., Med. Phys. vol 26 N°6 (974-991), 1999.

[61] "Experimental kerma coefficients of biologically important materials at neutron energies below 75 MeV" , J.P. Meulders et al., Med. Phys. vol 27 N°11 (2541-2559), 2000.

[62] "The response of the alanine detector after charged-particle and neutron irradiations", M.P.R. Waligorski et al, Appl. Radiat. Isot vol 40 (923-933), 1989.

[63] "Calculations of the relative effectiveness of alanine for neutrons with energies up to 17,1 MeV", H.M. Gertsenberg, Rad; Prot. Dosimetry vol.31 N°1/4 (85-89), 1990.

[64] "Fast neutron response of alanine probes", H. Schraube et al, Appl. Radiat. Isot vol 40 (941-944), 1989.

[65] "Radioactivity and radiation protection", R.J. Donahue & A Fasso in the particle data group booklet.

[66] "Standard practice for use of the alanine-EPR dosimetry system", ASTM note E 1607-96.

[67] "The response of the alanine dosemeter to low energy protons and high energy heavy charged particles", K.J. Olsen & J.W. Hansen, Radiat. prot. dosimetry vol 31 (81-84), 1990.

[68] "Proton response of alanine based pellets and films", S. Onori et al, Appl. Radiat. Isot vol 47 (1201-1204), 1996.

[69] "Alanine EPR dosimeter response in proton therapy beams", K. Gall et al, Appl. Radiat. Isot vol 47 (1197-1199), 1996.

[70] "Response characteristics of thermoluminescence and alanine-based dosemeters to 16 and 25 MeV proton beams", A. Bartolotta et al, Radiat. prot. dosimetry vol 85 (353-356), 1999.

[71] "UP350 Program Controller Instruction Manual", Yokogawa M&C Corporation, 1-19-18 Nakacho, Musashino-shi, Tokyo 180-0006, JAPAN.

List of figures

Fig. 1 : The LHC underground installations. The grey structures were already existing at LEP. 9
Fig. 2 : Signal significance of the various SM-Higgs discovery channels, after one year or 100 fb^{-1} (from [7]). 10
Fig. 3 : Layout of the CMS experiment at LHC. 13
Fig. 4 : A slice view of the HCAL Barrel: copper plates interleaved with plastic scintillators sheets. Copper plates are 50 mm thick whereas scintillator plates are 4 mm thick. The readout uses plastic wavelength shifting fibers. 14
Fig. 5 : Light monitoring system of the CMS electromagnetic calorimeter. LASERs are used as light source and distributed over the entire calorimeter using optical switches and fanouts. 16
Fig. 6 : The CMS pixel detector layout. One distinguishes the three barrel layers and the two turbine-like endcaps on each side. 17
Fig. 7 : Transverse view of the CMS tracker. The radius is about 115 cm and the length about 270 cm on each side of the IP. 18
Fig. 8 Clockwise from bottom left: support structure of TIB, support structure of the TOB filled with some rods, TEC honeycomb support disk, TEC petal with modules, details of the cooling pipes grooves of a TEC petal. 19
Fig. 9 : Drawing of a CMS barrel module. One can distinguish the carbon-fibre frame with the silicon sensors and their readout electronics. 20
Fig. 10 : CMS tracker electronics overview. 21
Fig. 11 : the tracker material budget distribution, expressed in terms of radiation lengths [16]. The photon attenuation length due to pair production is approximated by 7/9 the radiation length. At η=1.5, the photon attenuation is hence about 16 %. 22
Fig. 12a, b : Neutron and charged particle integrated fluences in the CMS tracker expressed in particles.cm^{-2} after 10 years at the LHC. 24
Fig. 13 : Diamond lattice structure. 27
Fig. 14a, b, c: Respectively <100>, <110> an <111> lattice orientation planes (pictured in purple). 28
Fig. 15 : The shallow donors and acceptor levels in the band gap of silicon with the corresponding free charge carriers (from [2]). 30
Fig. 16 : The built-in depletion zone of a PN junction and the direction of the resulting electric field. 30
Fig. 17 : General layout of an AC-coupled microstrip detector [21]. 33
Fig. 18 : Longitudinal cut view of a silicon microstrip detector. 33
Fig. 19 : Circuit diagram of a silicon microstrip sensor. 36
Fig. 20 : Basic damage cascade process caused after a PKA: the initial impact took place at location (0,0). Taken from the ROSE collaboration, [32]. 39
Fig. 21 : Simple defects in a 2-D crystal, from ref. [2]. 40
Fig. 22 : NIEL hardness factors in the case of neutrons from 0.1 to 100 MeV. 42

Fig. 23 : Increase of the leakage current density as a function of the fluence, measurements performed after 80 minutes of annealing at 60 °C (taken from [32]). 43
Fig. 24 : Leakage current annealing behaviour after irradiation: α is the leakage current of the detector divided by its volume times the 1-MeV equivalent fluence it has been submitted to (from [32]). 44
Fig. 25 : Typical evolution of the effective doping concentration of a n-type initial bulk, as a function of the fluence, for a given annealing state. From ref [32]. 46
Fig. 26 : General scheme of the post-irradiation effective doping concentration evolution under annealing. From ref [32]. 46
Fig. 27 : Simulation of the evolution of the depletion voltage as function of the initial resistivity, irradiation fluence and annealing time at LHC, for inner barrel CMS tracker sensor of different initial resistivities (taken from [44]). 53
Fig. 28 : Signal to noise ration of irradiated CMS R&D structures (from [39]). The Breakdown resistance of the detector is clearly shown here as a crucial characteristic of the detector as the best ratio is obtained at high bias. 54
Fig. 29 : The CMS silicon sensor qualification scheme. This work is part of the tasks belonging to the Irradiation qualification centers. 55
Fig. 30 : The semi-automatic Probe station. 60
Fig. 31 : The lab-made chrome plated chuck and its fixed needle. 61
Fig. 32 : Schematic view of the instruments and electrical connections around the probe station. 62
Fig. 33 : Screenshot of the probe station acquisition program. 62
Fig. 34 : LabVIEW® program hierarchy in the case of a CV on MOS device. 63
Fig. 35 : influence of chuck-vacuum in the Karlsruhe setup (the step in current appears when vacuum is applied on the sensor). This effect is observed despite the high planarity of the chuck plate. Taken from [47]. 65
Fig. 36 : Effect of vacuum on Leakage current (measurement performed at 20 °C on non-irradiated 500 µm thick sensor). There is clearly no vacuum-induced effect. 66
Fig. 37a, b : Dielectric breakdown observed on thin (HPK) and thick (ST) structures after irradiation. Both type of structures where submitted to the same test conditions, but Hamamatsu (HPK) devices are more affected due to lower dielectric breakdown voltage. 66
Fig. 38 : Voltage applied on the strip dielectric during 5 strip test sequences (before switching revision). The transient variations at each step were the cause of pinhole creation. 67
Fig. 39 : Voltage applied on one strip test sequence (after switching revision). Transient peaks have been removed, and setup-induced pinhole creation stopped. 68
Fig. 40 : CV decoupling filter principle. 69
Fig. 41 : Interstrip capacitance measurements performed at Karlsruhe & Louvain, after irradiation on the same p-irradiated structures. 70
Fig. 42 : Interstrip capacitance measurement perturbation. 70
Fig. 43 : Post-irradiation interstrip resistance measurements made in Louvain and Karlsruhe (on the same structure but at a different annealing stage). 72
Fig. 44 : Neutron production in the T2 beam line. 74

Fig. 45 : The fast neutron beam line energy spectrum. Taken from [49]. 74
Fig. 46 : Radial extension at 80, 70 and 60 % maximum of the T2 neutron beam line, taken from [49]. 75
Fig. 47 : Principle of operation of the irradiation cooling system. 77
Fig. 48 : Time evolution of the temperature inside the irradiation cold box during calibration setup and afterwards. 77
Fig. 49 : Fast neutron beam line irradiation box on it's sliding rail. One can distinguish the HV connections for sensor biasing on the side. 78
Fig. 50 : Irradiation support for the test structures. One can distinguish the aluminium strips on the side for bonding and electrical connection of the bias line and backplane of the sensor. 83
Fig. 51 : Screenshot of the irradiation monitoring program. 84
Fig. 52 : The sensor test protocol in Louvain-la-Neuve. 85
Fig. 53 : Typical silicon pad-diode design, as irradiated in this test (taken from [51]). 90
Fig. 54a, b : Oxygenated (left) and standard (right) silicon diodes CV curves before irradiation. 91
Fig. 55: Oxygenated & standard silicon diodes IV curves before irradiation. 91
Fig. 56 : Quasi-monoenergetic beam neutron production in Louvain-la-Neuve. 92
Fig. 57 : Monoenergetic simulated and measured neutron spectra for incident proton energies of 36, 48 and 63 MeV. 92
Fig. 58 : Comparison of the CV curves before and after irradiation for each annealing step on diode cc16-09, irradiated with 33 MeV neutrons at a fluence of 6.8 10^{10} n/cm^2. 96
Fig. 59 : Comparison of the leakage current on diodes pre- and post-storage in a fridge after an annealing step of 20 minutes at 60 °C. The diodes were irradiated with 33 MeV neutrons for a real fluence of 6.8 10^{10} n/cm^2. 97
Fig. 60 : Evolution of the alpha parameter measured on the diodes for different neutron energies, compared to literature [32]. 98
Fig. 61 : Neutron hardness factors as compiled from literature ([42] and [52]) compared to results obtained at Louvain-la-Neuve with the monoenergetic neutron beam line. 100
Fig. 62 : The 4 half moons cut around a Hamamatsu sensor (the standard structure is the right one). 101
Fig. 63 : The standard CMS test-structure devices. 102
Fig. 64: Post-irradiation leakage current of biased and unbiased standard test structures. 104
Fig. 65 : Post-irradiation depletion voltages of the biased-unbiased sample. 105
Fig. 66 : After irrad. R_{poly} ramps on biased (red) and unbiased (blue) thick and thin structures. 107
Fig. 67 : Variation of the bias resistors on biased/unbiased samples, taken at 400 V bias. 107
Fig. 68 : Coupling capacitance variation distributions on biased/unbiased samples, taken at 400 V bias. 108
Fig. 69 : Distributions of the variations of the interstrip capacitance for biased/unbiased samples, taken at 400 V bias. 109

Fig. 70 : Interstrip resistance as a function of normalised bias for thick structures - Red lines show the results for the irradiation-biased structures. 110
Fig. 71 : Interstrip resistance as a function of normalised bias for thin structures - Red lines show the results for the irradiation-biased structures. 111
Fig. 72 : Interstrip resistance distributions on biased/unbiased samples. 111
Fig. 73 : The leakage current of a baby detector after irradiation, at different temperatures. 113
Fig. 74 : alpha distribution for thick and thin structures. 114
Fig. 75 : Standard diode annealing curve at 40°C. 115
Fig. 76 : Post-irradiation depletion voltages obtained during the neutron irradiation tests in Louvain on 500 µm-thick CMS structures. 117
Fig. 77 : Post-irradiation depletion voltages obtained during the neutron irradiation tests in Louvain on 320 µm-thick CMS structures. 117
Fig. 78 : Evolution of the depletion voltage of an irradiated thin HPK structure kept biased at 400 V at –10 °C. 119
Fig. 79 : CV curves measured during the long term test. 120
Fig. 80 : R_{poly} variation after irradiation (red triangles for thick structures, blue diamonds for thin ones). 120
Fig. 81 : Distributions of the polysilicon variations after irradiation for thick and thin structures. 121
Fig. 82 : coupling capacitance variation expressed as percentage of the initial value for thick (red) and thin structures (blue) 122
Fig. 83 : coupling capacitance variation distributions. 122
Fig. 84a, b : post-irradiation interstrip resistance as a function of the bias status for thin and thick test structures. 123
Fig. 85 : value at local minima of the curve. 124
Fig. 86 : interstrip capacitance variation distribution as a function of the fluence. 125
Fig. 87a, b : Interstrip capacitance as a function of the bias voltage for thin (left) and thick (right) structures. 125
Fig. 88a, b : Interstrip capacitance measurements as a function of bias voltage for HPK (left) and ST (right) thick structures, up to 1000 V. 126
Fig. 89 : Time required to get 10^{14} n/cm^2 (not 1 MeV-equivalent) in the T2 neutron beam line with a deuteron current of 1 µA. 129
Fig. 90 : Keithley acquisition card and electrometer calibration curves. 130
Fig. 91 : Efficiency of the Canberra HPGE detector. 133
Fig. 92 : The Bruker E-scan alanine reader. 136
Fig. 93 : Response of PAD-Elcugray to neutrons as taken from [59]. 137
Fig. 94 : Alanine relative effectiveness to neutrons taken from [63]. 138
Fig. 95 : Alanine fluence-to-dose conversion factors for protons. 140
Fig. 96 : Annealing oven. 142
Fig. 97 : Annealing oven working principle. 143
Fig. 98 : Temperature stability test at 60 °C (standard annealing temperature). 144

List of tables

Table 1 : Average NIEL factors in the tracker (in MeV.mb). 25
Table 2 : 1-MeV equivalent fluences as quoted in [15] and [16]. 26
Table 3 : The different CMS sensor designs. 54
Table 4 : Tests performed on sensors by quality test centres, and the corresponding qualification criteria (cf. [46]). 56
Table 5 : Summary of the measurements and acceptance criteria for the process qualification center (PQC) tests (cf. [46]). 57
Table 6 : Criteria for the irradiation qualification (IQC) tests. 58
Table 7 : The high flux neutron beam contaminations. 75
Table 8 : Leakage currents foreseen for 320 µm CMS structures and sensors. 80
Table 9 : Leakage currents foreseen for 500 µm CMS structures and sensors. 80
Table 10 : Depletion voltages foreseen for CMS test structures and sensors from the inner tracker (320 µm thick sensors). 81
Table 11 : Depletion voltages foreseen for CMS test structures and sensors from the outer tracker (500 µm thick sensors). 82
Table 12 : Integrated beam time and fluence summary for the monoenergetic neutron beam. 93
Table 13 : Summary of the experimental hardness factor determination results. 100
Table 14 : Biased-unbiased alpha parameter comparison. 104
Table 15 : Average and standard deviation values of the depletion voltages. 105
Table 16 : Average & standard deviation values for the bias resistor variation of biased and unbiased samples. 108
Table 17 : Average & standard deviation values for the coupling capacitance variation of biased and unbiased samples. 109
Table 18 : Average and standard deviation values for the interstrip capacitance variation of biased and unbiased samples, taken at 400 V bias. 110
Table 19 : Average and standard deviation values for the interstrip resistance for biased and unbiased samples. 112
Table 20 : Parameters used in the Hamburg model to compare expected values of the depletion voltage with the experimental data of the first irradiated diodes. 115
Table 21 : Parameters used in the Hamburg model to fit the depletion voltage data of CMS 500 µm thick test structures. 116
Table 22 : Parameters used in the Hamburg model to fit the depletion voltage data of CMS 320 µm thin test structures. 116
Table 23 : Reactions of interest in the T2 beam line activation measurements. 134
Table 24 : Alanine fluence-to-dose conversion factors obtained using literature (cf. [60], [61], [62] and [63]). 138
Table 25 : Electrical properties of silicon crystal (at 300 K). 145
Table 26 : Physical properties of Silicon 146
Table 27 : Silicon oxide properties 146